UNIKASSEL VERSITÄT

Master Thesis

ON

Development, Manufacturing, and Testing of a P-and L-Band Outdoor Horn Antenna

Submitted to
Department of Microwave Electronics
Faculty of Electrical Engineering and Computer Science
University of Kassel, Germany

in partial fulfillment of the requirement for the degree
Master of Science in Electrical Communication Engineering

Thesis work carried out at
Microwaves and Radar Institute, German Aerospace Center (DLR)
Oberpfaffenhofen, Weßling, Germany

Author:	Sravan Kumar Aitha
Matr.Id:	[33108827]

Supervisor:	Dr.-Ing. Björn Döring (DLR)
First Examiner:	Prof. Dr.-Ing. Axel Bangert
Second Examiner:	Prof. Dr. Bernd Witzigmann

October 6, 2016

Declaration

I do solemnly declare that the presented Master Thesis is an original piece of work and has not been imitated or copied from elsewhere, to the best of my knowledge. All parts which were taken over word-to-word or analogous from literature and other publications are quoted and identified.

Furthermore, I certify that this research thesis or any part of it has not been previously submitted for a degree or any other qualification at the University of Kassel or any other institution in Germany or abroad.

Weßling, 6. October 2016

Sravan Kumar Aitha

Acknowledgment

I am immensely grateful for all the co-operations and encouragements extended towards me during my works add efforts on my master thesis. First and foremost, I would like to express my sincere gratitude to Prof. Dr.-Ing Axel Bangert for agreeing to be my advisor. The guidance and encouragement provided by him has always been a great motivation towards my yearnings. My sincere thanks to Prof. Dr. Bernd Witzigmann for readily agreeing to be my second examiner.

I am eternally grateful to my supervisor Dr. Björn Döring for giving me an opportunity to work on such an interesting topic and also for his time, patience and continuous support throughout my entire course of the thesis. This is worth mentioning that his conceptual ideas and guidance at every stage in my work have shaped me and my work to a perceptible direction. I owe a special mention to Dr. Marco Schwerdt for giving me an opportunity to start my professional career as a research assistant in his DLR-HR Calibration Group.

A special Institute from the DLR is not mentioned yet, the Systemhaus Technik Süd team. I praise the enormous amount of help from Johanna Herzig and Lang Matthias in providing the CAD files and 3D-printing the L-Band antenna model with their 3D-printer. Without their precious support it would not be possible to complete the other half part of my thesis. My sincere thanks also goes to Bernd Gabler for explaining me the basics about antenna measurements and also allowing me to conduct measurements in DLR Compact Test Range facility.

Besides my work, I would like to thank my colleagues Daniel Rudolf, Klaus Wedeinhaupt Frank, Sebastian Raab and Walter John Mohan Anthony for accompaning me during the launch hours and made my stay at DLR more enthusiastic. I humbly thank to all the other concerns and professional bodies and organizations attached to my work for having faith on me for carrying on my work and continuously seeking valuable information from them.

Last but not least I would like to thank my family for both financial and emotional support, without them I would not be here.

Sravan Kumar Aitha

I dedicate this Thesis to my beloved parents and my friends

Abstract

In recent years a new class of synthetic aperture radar (SAR) systems using low frequency have emerged. This pertinent wavelength made the SAR technology for global monitoring and to provide high resolution images of terrain from remote location. To achieve accurate images of forest biomass and its changes, the SAR technology has aimed for P-band (center frequency of 435 MHz). But this low frequency poses new challenges for SAR calibration, namely the design and manufacturing of cost-effective calibration transponders.

One of the main challenges in designing a P-band calibration transponder lies in developing and designing an antenna and its feeding system which has dual polarization capabilities, cross-polar rejection, sidelobe suppression and should be of reduced size and light weight. Based on these specifications, in the year 2014, a compact corrugated high performance Gaussian horn antenna known as VeGA (from German Verkurzte-Gauß-Antenne) and a novel orthomode transducer (OMT) were developed and designed at C-band (5.405 GHz) by DLR-HR (DLR: German Aerospace Center) [1, 2]. The long-term goal was to base a P-band horn design on this C-band prototype. But the procedure used in manufacturing the C-band antenna prototype was not the right choice to implement at P-Band as per the crucial requirements of Biomass mission [3]. Biomass is a SAR satellite mission which will provide the first opportunity to explore Earth's surface at the 'P-band' radar frequency from space as planned by the European Space Agency (ESA) and scheduled for launch in 2020 [3].

Overcoming the limitations of the previously manufactured antenna prototypes, the goal of the Master thesis at the Microwaves and Radar Institute of DLR (DLR-HR) was to develop and investigate a compact lightweight VeGA and OMT at P-band by considering standard waveguide dimensions. Numerical simulations are presented which resemble in satisfying the design requirements as illustrated in Tab. 1.1. Moreover simulations for the determination of allowable manufacturing tolerances and resultant uncertainties are also presented. But due to time and cost constraints, the P-band antenna model was scaled down and 3-D printed at L-band (1.2575 GHz) which is affordable, can be measured and also can be used for an L-band calibration transponder.

The antenna is printed using Acrylonitrile Styrene Acrylate (ASA) material, a thermoplastic and then coated with carbon conductive paint. The combination of the plastic material and the conductive paint used in 3-D printing the L-band antenna is quite innovative and cheap which pushes the radio frequency technology to manufacture lightweight antennas and its feeding system for outdoor applications. The new antenna design and the verification measurements show that a promising concept has been implemented, eliminating one of the main hurdles in creating accurate P-band SAR calibration transponders.

Keywords. SAR system calibration, Transponder, Antenna design, Corrugated horn antennas, Orthomode transducer, 3-D printing.

Contents

List of Tables

List of Figures

Chapter 1

Introduction

Before moving into technical part of the thesis, the idea and the reason for the thesis is presented to the reader in form of chapters. This chapter gives the necessary background information and defines the objective for the work presented in later chapters, which altogether motivates the structure of the thesis..

1.1 Synthetic Aperture Radar

A synthetic aperture radar (SAR) is a system for providing high-resolution two and three-dimensional digital images. It is an active sensor system which is capable of illuminating itself independent of daylight from the sun, cloud coverage and weather conditions [8]. Achieving high-resolution is a main criteria in SAR systems. In non-SAR systems, resolution is governed by ratio of the wavelength of the electromagnetic radiation to the aperture size [9]. In such kind of systems to achieve better image resolution, for example to achieve a radar wavelength of 25 cm an antenna of approximately 8 km length is required [9]. This kind of antenna dimensions makes impractical for satellite design. To overcome this drawback SAR technology has emerged in increasing the resolution without increasing the physical antenna aperture size. This section gives the reader a basic idea for how SAR works.

The potential of SAR in a diverse range of application led to the development of a number of airborne and spaceborne SAR systems [10]. It is the most promising technology of radar systems, which is responsible to form image of a terrain from remote location. The geometrical configuration of two-dimensional image is illustrated in Figure 1.1. In general an airborne vehicle carries on-board a sensor or an antenna and an arrangement is made such that the sensor perform measurements othogonal to the velocity vector of the vehicle. The sensor scans the images or targets in two-dimensions known as cross track and along track. For real array imaging radar, its long antenna produces a fan beam illuminating the ground below [10]. Measurements in cross track or range are acquired by

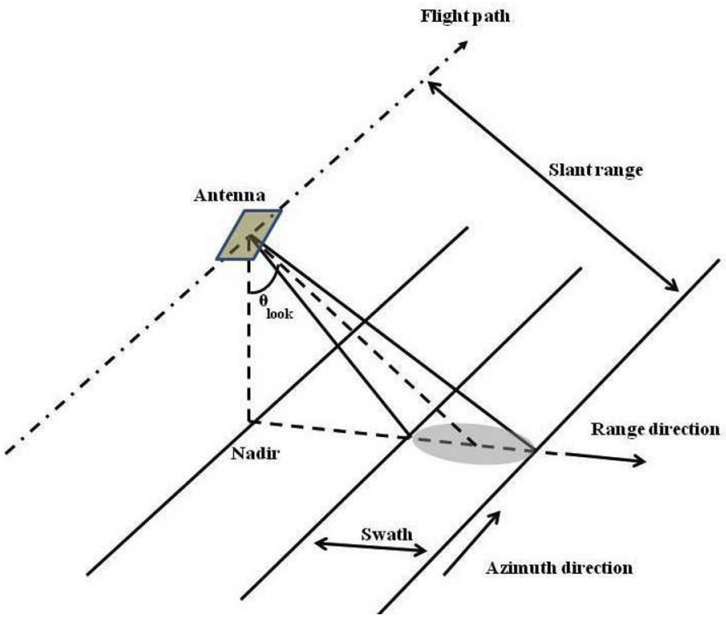

Figure 1.1: Typical geometry of side-looking SAR [4].

determining the line-of-sight distance from radar to target which is mostly performed by radar systems. The resolution of range is determined by the pulse width. The scanning in the along track or azimuth is performed by moving the vehicle or scanning perpendicular to the range and its resolution is determined by the beamwidth [11]. In Synthetic Aperture Radar, by recording and combining the individual echoes reflected from the object a synthetic aperture is created, allowing creation of high resolution images. Later on SAR signal processing is then used to reconstruct the imaged scene from the recorded pulse reflections [12]. The utilization of the Doppler effect (frequency shift) in increasing along track resolution makes the SAR technology to be different from the Real Aperture Radar systems. This is how the basic principle of SAR works.

The applications for this technology include: monitoring crop characteristics, deforestration, mineral exploration, monitoring of sea ice, disaster analysis, biomass estimation, oceanography and military intelligence [11]. The increase in resolution not only depends on the antenna size but also the signal processing techniques. To implement the operation of SAR for global monitoring or recording the geolocated terrain reflectivity, a number of technical challenges are to be done. Out of these challenges two specific areas are explained in next subsections [9]. They are:
1) SAR calibration
2) Transponders and Necessity

The detailed explanation of operation of SAR is complex and there are many outstanding books where a good overview about SAR is given in [8, 9].

1.1.1 SAR Calibration

A SAR system is not only used for imaging or detection but is also a measurement instrument that acquires measurement data for earth-observation applications [9]. But before the nominal operation phase, the SAR system has to be adjusted to ensure the delivery of SAR data products of high qualitiy. For this purpose, after launch, the SAR system is calibrated during the so called commissioning phase [13]. This calibration is based on measurements of the whole spaceborne SAR system against reference targets deployed on ground and aligned for an overpass of the satellite. In general any measurement instrument which involves a comparative study of radar reflectivities requires calibration. These comparisons are performed across radar systems or across frequencies or polarization channels with same system [14].

The SAR calibration activities are usually split into geometric and radiometric calibration [15]. The purpose of geometric calibration is to establish the absolute location accuracy on a cartographic grid. The accuracy with which an image pixel can be related to the target scattering characteristics is termed as radiometric calibration. The radiometric calibration is a two-step process which is divided into relative and absolute radiometric calibration [16]. Relative radiometric calibration is based on an accurate internal calibration facility, integrated within the radar instrument for monitoring and compensating for drift effects, and on a precise antenna model for providing the antenna patterns, which are required to correct the gain drop across the swath during SAR data processing. In the final step, these relatively calibrated SAR images are converted to ERCS maps, so called absolute radiometric calibration. The SAR calibration is most frequently performed with passive (corner reflectors) and active (transponders) reference targets, which have an accurately known location and reflectivity [17], [18] as illustrated in Figure 1.2.

(a) (b)

Figure 1.2: (a): DLR's first remote controlled trihedral corner reflector. (b): DLR's C-band Kalibri transponder: both designed and built for radiometric calibration and can be operated remote controlled.

1.1.2 Trihedral Corner Reflectors

Triangular tetrahedral corner reflectors are the standard calibration targets mostly used for SAR calibration. A trihedral corner reflector consists of three electrically conductive (mostly Aluminum) plates which are aligned crosswise to each other, forming a corner. The orthogonally aligned plates ensures a stable large radar cross sections because the incoming electromagnetic waves are reflected back to the incident direction due to the triple reflections created by the conductive plates. The choice of the plates can be any shape, but mostly triangualr panel geometry is used due to the simplicity in structural design and manufacturing feasibility [19]. The effective radar cross-section of triangular corner reflector [9] is calculated by:

$$\sigma = \frac{4\pi a^4}{3\lambda^2}, \tag{1.1}$$

where a is the length of one side of the reflector and λ is the wavelength.

1.1.3 Transponders

Transponder is an active device which records and re-transmits the received signal with necessary amplification and a possible delay. Moreover these active targets are used as point targets for the radiometric calibration of space- or airborne synthetic aperture radar instruments [20]. As transponders amplify the received signal and re-transmit to the radar instrument, they have a much higher RCS with significantly smaller dimensions than passive targets. The main advantages of a transponder over passive tragets are its large radar cross-section, small in size, signal recording of the received signal and high achievable signal to noise ratio (SNR). The other advantage ove passive targets is the possibility to easily change the receive and transmit polarization according to the calibration task because of the rotatable antennas used in the transponder [15].

The building blocks of the transponder as shown in Figure 1.3a consist of a receiving antenna, a high-precision amplifier and a transmitting antenna. The Figure 1.3b shows the DLR Kalibri C-band transponder (designed and developed by DLR, Oberpfaffenhofen, Germany) employing two potter horn antennas along with waveguide feeds and several sub-components depending on the model and application requirements. The developed Kalibri C-band transponders are used for the calibration campaign of the Sentinel-1 satellites which are operated by the European Space Agency in the frame of the European-Copernicus Programme for global earth monitoring [21]. The basic functionality of a transponder is that the incoming signal received by the receiving antenna flows over a transmitting chain, composed of filters, amplifiers, and a down-converter. After down converting the received signal, it is further sent to the digital unit. There the signal can be recorded and delayed before it is routed over the transmitting chain to the transmitting antenna. The

amplification gain G_e and the receive and transmit antenna gains G_r, G_t determines the radar cross-section of a transponder and can be computed using Formula 1.2.

$$\zeta_t = \frac{\lambda^2}{4\pi} G_r G_e G_t, \text{ [20]} \tag{1.2}$$

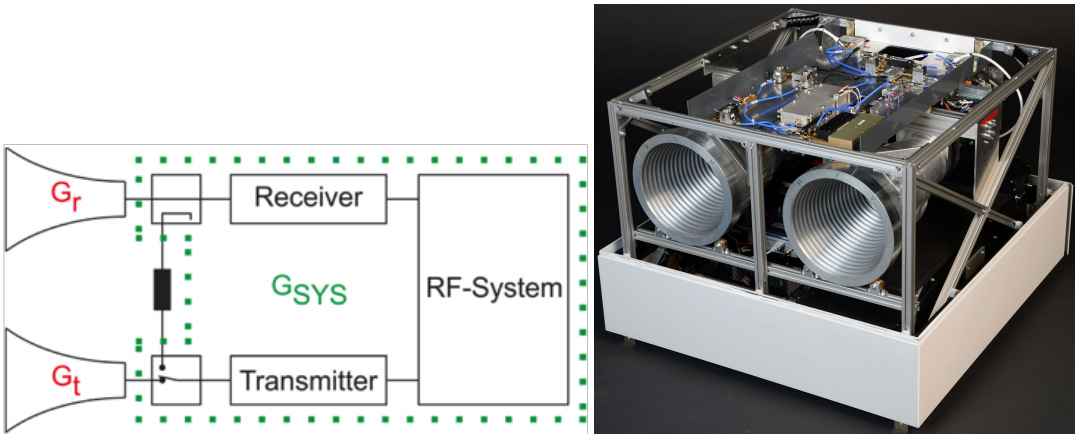

(a) (b)

Figure 1.3: (a): Block diagram of a transponder (b): DLR Kalibri C-band transponder desgined and developed for Sentinel-1 from [22] with housing removed. All parts including the antennas are installed in an outdoor housing. The RF components are mounted on a seperate plate and form together with the antennas one sub-component.

1.2 Motivation and Objective of the Thesis

In the frame of the Earth Observation Envelope Programme, ESA is undertaking the development of Biomass, a Core Earth Explorer Mission based on a SAR system operated in P-band (435 MHz) for assessing the Earth's biomass [3]. The mission measures the carbon stored in our planet's forests, height and disturbance patterns and it's change over time through interferometric & polarimetric P-band radar observations. According to [3], the reason for opting P-band for Biomass mission is, at low frequency SAR is able to penetrate dry sediments and map the subsurface down to several meters, because of low absorption and little volume scattering. The Biomass mission is expected to be launched in 2020 [3].

Once the Biomass SAR system is launched, during the commissioning phase the SAR instrument must be calibrated as discussed in subsection 1.1.1. The SAR calibration is normally split into geometric and radiometric calibration [23]. These type of calibration activities are performed using either passive (corner reflector) or active targets (transponder). In order to use these targets to calibrate the data of Biomass mission polarimetric SAR satellite, corner reflectors imposes dimensions of around 58 m and transponders require an antenna size of around 4 m × 4 m because of usage of long wavelength (68.9 cm) [24].

This kind of large size targets involve heavy weight, costly to manufacture and lot of hardware to maintain dual polarization capabilities.

As a challenge to acquire competence on light weight and compact structures for applications at P-band, in [1], [2], a high performance corrugated horn antenna and a feeding system called as orthomode transducer prototype which are intended to be used for calibration transponders were developed and built in C-band. The long-term goal was to base a P-band horn design on this C-band prototype and the developed horn antenna and orthomode transducer were supposed to satisfy the requirements illustrated in Tab. 1.1. But the previously developed prototypes [1], [2] in C-band were not suited for use in external environment, which is violating one of the requirement at P-band.

Requirement	**P-band**
Center Frequency f_0	0.435 GHz
Wavelength λ_0	68.9 cm
Bandwidth B	8 MHz
Cross-Polar Isolation (XPI)	$\geq$ 35 dB
Gain G	15 dBi
Return loss	$-20dB$
Temperature Range	$[-20; 40]$ °C
Durability	15 to 20 Years
The antenna should be 3-D printed and should be mostly used for outdoor applications.	
The antenna should have low weight and compact size as possible.	

Table 1.1: Design requirements of P-band Antenna.

The goal of this Master Thesis is to develop an antenna and its feeding system satisfying the design requirements in Tab. 1.1 by considering standard circular waveguide dimensions. In order to manufacture the developed antenna as light weight as possible and also sustaining long term effects when exposed to external environment, in study different plastics and different manufacturing techniques available in the market were examined first of all. Then finally the performance of the developed antenna prototype and its feeding system was validated by performing measurements.

Chapter 2

Theoretical Background

2.1 Plastics in EM Manufacturing

The advantages of being light weight, cost effective and easy fabrication of materials, for usage in automotive sector, electronic industry, aerospace, health care pushed the technology to plastics than metal counterparts. Low weight is even an attractive feature for antennas and many microwave components. In terms of electromagnetic waves, the difference between plastics and metals lies in electromagnetic interference (EMI) shielding issue. The metals are conductors and have a property of reflecting or absorbing EM energy, but plastics being insulators EM waves can easily pass through the unshielded plastic with negligible impedance. To shield the plastics, a conductive barrier has to be provided which has the ability to reflect or transmit electric interference to ground [25].

However to achieve electromagnetic interference (EMI) shielding, the plastic must be made conductive and this can be performed by either coating the plastic with conductive coating or to make the plastic itself conductive by injection of conductive particles into the plastic. The second method of conductive plastics is relatively new and most expensive technique. Meanwhile the coating on plastics parts are most popular and have varied shielding techniques which are implemented practically. The conductive metal flakes are added to a binding agent in order to make a liquid conductive paint. These coatings used on plastics make the plastic conductive and are capable of EMI shielding. A few examples of conductive coatings or conductivity materials mostly used are silver, copper, gold, aluminium and nickel.

The factors that are to be considered while coating the plastic with conductive paint are: the necessary skin depth of a coating according to the application or to a particular frequency, the achievable conductivity and shielding effectiveness. These are the most important parameters to be studied in this work in order to make the plastic highly con-

ductive.

2.1.1 Skin Depth

The skin depth is stated as the distance travelled by an electromagnetic wave into a conductor during which its amplitude is reduced by a value of '1/e' [26]. It can be briefly explained that, when an electromagnetic wave interacts with a conductive material, the charge carriers (electrons) in the material are made to oscillate back and forth with the same frequency as the impinging fields [26]. The movement of these electrons constitute an alternating current density. The magnitude of the current density at skin depth decays to 37% of the current density at the surface.The formula for skin depth is:

$$\delta = \frac{1}{\sqrt{\pi f \mu G}}, \tag{2.1}$$

where δ is skin depth, $\mu = \mu_0\, \mu_r$ is permeability of the metal, G is conductivity of conductor and f is the frequency.

It is clear from equation (2.1) that the skin depth is inversely proportional to frequency which means that the electromagnetic waves having different wavelengths penetrates into the conducting material upto certain depths. It also means that the skin depth is smaller for larger permeability. The relative permeability μ_r, of most metals is 1.0. But some ferromagnetic materials have a permeability greater than 100, in this case these ferromagnetic materials constitute to smaller skin depth even though the conductivity is smaller. At low frequencies a high permeability would reduce the skin depth and improve the magnetic field shielding characteristics.

In relevant to the thesis, before coating the plastics with conductive coatings, the required skin depth of a particular conductive coating for the specified frequency must be calculated. Also knowledge of skin depth determines the required thickness of coating to be coated on the plastic at a particular frequency. Based on this the skin depths of various pure conductor materials are calculated for P-band antenna and illustrated in Tab. 2.1. The values represented in Table 2.1 are taken from [27].

As per suggestions from Trevor S. Bird [28], it is noted that for conductive coatings to be highly reflective, it is necessary to have a thickness greater than 10 skin depths at center frequency. In order to avoid ohmic looses the minimum coating of a material should be atleast 6 skin depths. The table 2.1 only shows the conductivity and skin depths of pure materials, but it should be different for different conductivity coatings. The conductivity coatings are not pure materials and the need to find conductivity of the coatings is a must and is explained in next subsections.

Conductor(Pure)	Conductivity(G)$\times 10^6$ (Siemens/meter)	Skin depth (μm) at 435MHz
Silver	62.1	3.04
Copper	58.5	3.16
Gold	44.2	3.6
Aluminum	36.9	4
Nickel	14.3	0.25(μ=100)
Zinc	16.6	5.8
Chromium	7.9	8.767

Table 2.1: Skin depths of different materials at 435 MHz.

2.1.2 Conductivity, ($Siemens/meter$)

The next step in determining the skin depth at a particular frequency for any conductive material is conductivity. Moreover it was observed that most of the paint manufacturers do not specify an accurate conductive value of the paints in their company data sheets because the conductivity depends on the thickness of the paint coated on any specimen, which is true. Also it was mentioned in [29] that the conductivity of conductive coating is typically one to two orders of magnitude less than that of pure metal, because electrical conductivity can be achieved only through contact between the metal flakes in the liquid paint. Therefore a theoretical or practical approach in determining the conductivity of paint is necessary and would be explained in the following subsections.

Conductivity explains a material's ability to conduct electricity, but how the conductivity can be determined for conductive coatings. It can be determined in a step by step manner from parameters like surface resistivity and volume resistivity or shielding effectiveness.

Surface Resistivity (Ω/sq)

It measures the resistance of a material along the plane or surface of the sheet where charge is distributing over its surface [25]. As long as the surface resistivity measurements is related to square, it would be expressed as "ohms-per-square". The procedure for testing surface resistivity is mostly performed using four point probe meter, two probe multimeter or electrometer techniques, which follows ASTM D-257 standard [30]. From the available measurement techniques, an example for measuring surface resistivity is described below [5]:

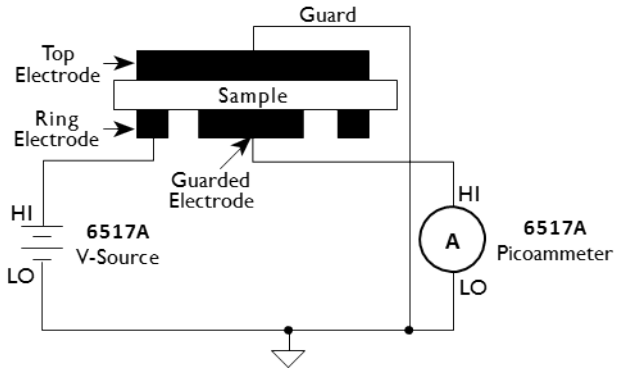

Figure 2.1: Surface resistivity measurement technique, adapted from [5].

A voltage potential or charge is applied across the surface of the sample using the electrode and the resultant current is measured using the negative potential electrode as shown in Figure 2.1. An electric charge can easily be redistributed over the material surface when the surface resistivity value is low and this results in more accurate conductivity measurements. By measuring the resistance, the distance between electrodes, the surface resistivity can be calculated by using the equations $\rho_s = K_s \times R$, $K_s = \frac{P}{g}$ [5], where ρ is surface resistivity, R is resistance in Ohms(V/I), P is effective perimeter of the guarded electrode and g is the distance between the electrodes. If the conductive coating is conductive enough then four probe technique is the best and widely used technique for measuring the surface resistivity.

Volume Resistivity ($\Omega - cm$)

It measures the resistivity of a material or sample through its volume or a defined thickness. The lower the volume resistivity, the higher the conductivity, because volume resistivity and conductivity are inversely proportional. The volume resistivity can be calculated by using the equation 2.2 using the experiment illustrated in Figure 2.2.

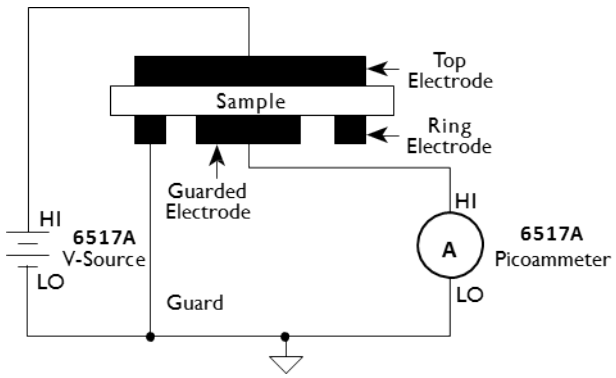

Figure 2.2: Volume resistivity measurement technique, from [5].

$$\rho_v = \frac{K_v}{\tau} \times R \tag{2.2}$$

where, ρ_v= volume resistivity, K_v = the perimeter of the guarded electrode and τ= thickness of the sample.

The equation 2.4 also gives an assumption that surface resistivity times thickness of the sample gives the volume resistivity of the material. According to [31], the conductivity may be calculated using the equation 2.3.

$$G(S/cm) = \frac{1}{R/sq[\frac{2.54t}{1000}]} \tag{2.3}$$

where, t is the thickness of the coating (mils) and R is the surface resistivity.

Shielding Effectiveness

Shielding effectiveness(SE) is measured in term of attenuation. It is defined as the ratio of the field strength without the shielding interposed to the field strength with the shield interposed. It is expressed in decibles(dB) and SE is most often measured using MIL-STD-285 test method [31].

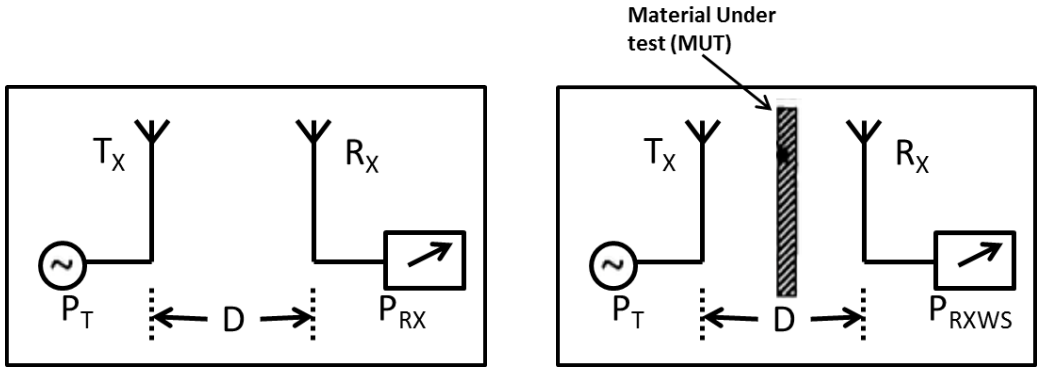

Figure 2.3: Principle of shielding effectiveness measurement, from [6].

The basic test setup for the SE measurement is shown in Figure 2.3 and can be calculated by using the equation 2.4. In this test method, initially the transmitting antenna (T_X) is powered by a signal generator. The receiving antenna R_X is also arranged at distance of 3 meters away from the T_X antenna. The power received by the receiving antenna P_{RX} is measured in dBm using the spectrum analyzer. In the second step a shielded sample under test (MUT) is introduced between transmitting and receiving antenna and P_{RXWS} the power received by the receiving antenna can be obtained by the same conditions [6].

$$SE = 10\log\frac{P_{RX}}{P_{RXWS}}dB \tag{2.4}$$

The SE is related to the electronic and magnetic properties of the coating and also

the interface between the materials. The conductive coatings with high relative magnetic permeability and high electrical conductivity contribute for better shielding effectiveness. The most cost effective and frequently used conductive coatings for EMI shielding applications are nickel-filled acrylic or polyurethane conductive coatings [31].

To write a short summary in choosing the reliable and approachable method for determing conductivity, it was realized that conductivity of a coating can be determined with the combination of surface and volume resistivity parameters which subsequently helps in determining the skin depth. The also reason for choosing the method based on the combination of surface and volume resistivites is due to readily and user friendly instruments available in the market like four point probe and eddy cúrrent based method [32]. The topic on conductivity is further discussed in Chap. 5.

2.2 Corrugated Horn Antenna

In present scenario, aperture antennas (Horn antenna) attribute to the development of the present and future communication systems with high performance antennas, high gain and low crosspolarization requirements. A horn antenna can be formed by flaring one end of a waveguide, rectangular or conical. Without the flare, a microwave signal making a sudden transition from the waveguide's impedance to free-space impedance would suffer a mismatch. The flare can be designed in various geometrical ways to smooth the transition. There are certain drawbacks to be observed in the performance of horn antennas. Due to the sudden discontinuity at the edge of radiating aperture or due to finite flange, leads to edge diffraction of EM waves and also generation of currents on outer surfaces, which contribute to production of side lobes and back lobe [26]. To overcome these drawbacks, corrugated surface horn antenna are preferably used.

Corrugated horn antenna can produce desirable radiation patterns having extremely good axial symmetry, low cross-polarization and low sidelobes because they support the hybrid mode HE_{11}. HE_{11} mode is a combination of transverse electric and transverse magnetic modes. This is due to the fact that the corrugated surfaces generates modes with modified field distribution in the E-plane which is uniform and circumferential electric and magnetic fields are zero at the aperture, forming a cosine wave [33].

Design principle of corrugated horn antenna. The design principle of any corrugated horn depends on the corrugated surfaces, because the corrugated surface can generate a condition in which both the impedance and admittance at the surface of corrugations becomes zero [34]. This condition basically constitutes to linear aperture electric field HE_{11} mode, illustrated in Figure 2.4b. It was stated from the paper [33] that better performance

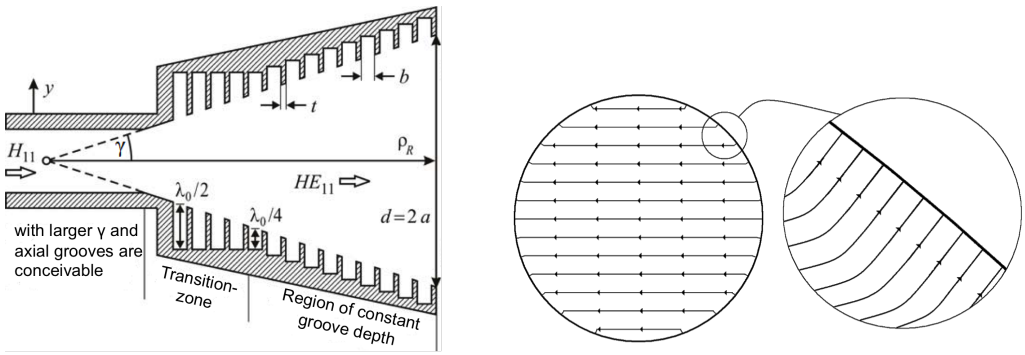

(a) (b)

Figure 2.4: (a): Typical corrugated horn antenna [35]. (b): HE_{11} aperture electric field of a circular corrugated horn [34].

from the corrugated horn antenna can be achieved by considering the following hints. a) In order to have zero azimuthal electric field at the surface of corrugations, a necessity of enough corrugations per wavelength (λ) is needed. It is also said that if the corrugations are narrow and $\lambda/4$ deep, they act as short transmission lines where the short circuit at the end of the slots transform into an open circuit at the corrugation boundary ensuring zero tangential transverse magnetic field [33]. b) The slot depth d is selected such that $\lambda/4$ < d < $\lambda/2$. Under this condition, generation of power around the radius of the corrugations is low, and causes low levels of cross polarization. c) A very gradual change from a slot depth of $\lambda/2$ to $\lambda/4$ from the throat toward the aperture can avoid the excitation of the surface waves so that the diffraction is minimized. A typical corrugated horn antenna is shown in Figure 2.4a.

The corrugation geometry of a horn antenna is divided into two parts, the throat and the flare region. The throat region determines the input impedance of the antenna and the flare region determines the position of phase center and generation of any high order modes. Corrugated horn antennas generally are composed of input waveguide, mode converter, transition section and the flare. The diameter of the horn and the flare angle have a significant role in controlling the radiation patterns of the antenna. The mode converter is carefully designed to have a smooth transformation of dominant mode TE_{11} at input waveguide toHE_{11} mode at the end of mode converter to avoid impedance mismatch between exciting waveguide and the horn. Corrugated horns are widely used in communications, radio astronomy, satellite tracking, radar, and remote sensing. The most widely used corrugated horn antennas are conical in shape [34].

2.2.1 Corrugated Gaussian Profiled Horn Antenna (GPHA)

A free space radiation from an antenna is possible by gaussian modes, obtained from the solutions of the paraxial free space wave equations. The advantage of the gaussian modes in antennas provide a perfect matching between waveguide modes and the free space modes (fundamental gaussian mode, Ψ_{00}) [34]. The gaussian modes do not contribute to sidelobes and crosspolarization and are better than HE_{11} modes as given in Figure 2.5. A corrugated GPHA (Gaussian profiled horn antenna) fed with a hybrid mode results in high purity gaussian beam mode [34]. These corrugated GPHAs are added at the end of corrugated horn antennas. The profile for Gaussian profile horn antennas is defined by the equation 2.5.

$$w(z) = w_0 \cdot \sqrt{1 + \left(\frac{\lambda \cdot z}{\pi \cdot {w_0}^2}\right)^2} \tag{2.5}$$

Where, λ the wavelength and w_0 is the beamwaist at z=0 of the fundamental gaussian mode. The important parameters to be considered while designing a corrugated GPHA are profile length, input diameter (defines beamwidth) and the alpha parameter of the profile [34]. The alpha parameter governs in obtaining the perfect Gaussian beam at the output.

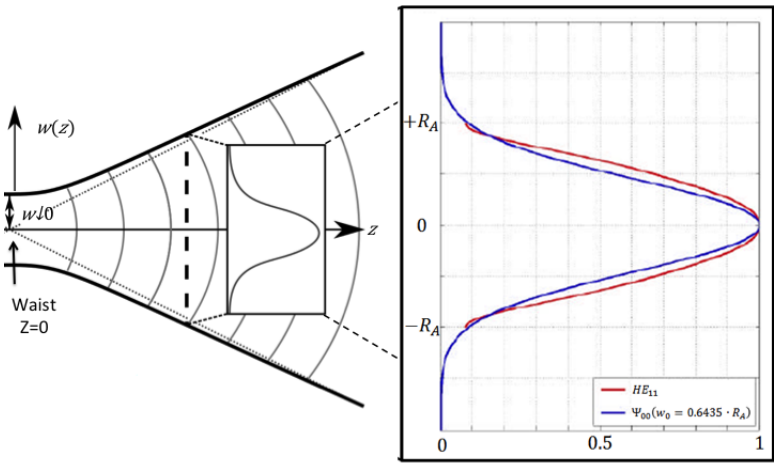

Figure 2.5: Fundamental gaussian beam mode (left) and comparison between HE_{11} at aperture of the horn and Ψ_{00} (right) [34].

From the book [34], a GPHA produces very nice radiation patterns with very low sidelobes, when a pure hybrid mode HE_{11} is considered as a feed at the input of GPHA. It is possible to obtain such a hybrid mode HE_{11} at the input diameter of corrugated GPHA by

using some optimization codes [36], but the solution is long. In case if the linear profile (vertical corrugations) corrugated horn antennas are used for low frequencies for example 435MHz, it is possible to obtain better performance, but the horn is very lengthy, not suitable for satellite application due to heavy weight and length. Even for S-Band frequencies a compact linear profiled bowl shaped corrugated horn antenna was designed in [37], but the profile has high number of grooves leading to tolerance issues while manufacturing. In spite of these issues corrugated GPHAs are considered to have better output profiles than any other corrugated horn antenna.

2.2.2 Verkürzte-Gauß-Antenna

For past 20 years many corrugated horn antennas were designed and developed, achieving the performance of corrugated antennas like gain, directivity, low cross polar and side lobe levels. These antennas have vertical corrugations throughout the profile of the horn antenna. Additional design parameters, relevant to satellite applications are length and weight, which need to be minimized [34].

Based on these limitations in using corrugated GPHAs for space applications, a compact (where "compact" refers to physical dimensions) choked GPHA was developed [38]. The concept is based on the combination of short choked antenna (horizontal corrugations for throat region) with the gaussian profile corrugated horn (vertical corrugations for flare region) attached to it and the schematic is shown in Figure 2.6. The advantage of using a choked antenna as a throat for horn antennas is to dramatically reduce the length of corrugated antennas and also a pure hybrid mode at the throat section can be obtained by using choked antennas (mode converter from TE_{11} to HE_{11}) at the throat. The details for choked corrugated antenna are explained briefly in [39]. Choked-gaussian horns are a good solution now-a-days for around 15-20% bandwidth requirements and even a bowl-shaped choked gaussian GPHA was developed in [38]. It has better radiation patterns with almost zero sidelobes, crosspolarization greater than 44 dB and the Bandwidth is around 15 to 20 %. But this bowl shaped horn has more ridges which lead to tolerance issues. Hereby considering the advantages of choked GPHAs, in 2014 a compact high performance choked GPHA, known as VeGA (from the German Verkürzte-Gauß-Antenna) was designed by [1] for C-band and also scaled to P-band (435 MHz). This antenna is more compact in size than bowl-shaped antennas [38], the tolerance issues for VeGA are negligible and a Gaussian mode Ψ_{00} is generated at the aperture.

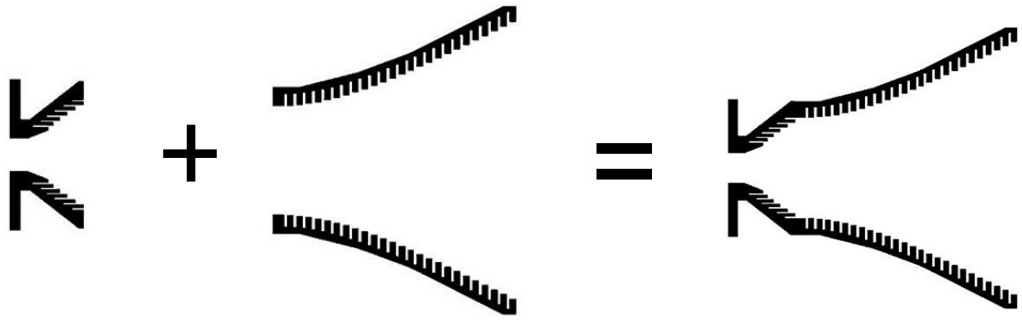

(a) Choked profile (b) Gaussian neck profile (c) VeGA Profile

Figure 2.6: Schematic of VeGA horn antenna [1].

A choked GPHAs solves the problem in terms of compact size for use in calibration transponder, but the weight of such a horn antenna is still an issue. Taking this into account, the VeGA for C-band was 3-D printed using additive manufacturing techniques in PA (Polyamide) 2200 which is a plastic material [1]. In order to make the plastic function as a conductor, it was coated using a conductive coating. So now it is important to know in detail information about different 3-D printing techniques and also to know whether any 3-D printing techniques are utilized for manufacturing complex antennas. The answer is explained in the coming chapters.

Chapter 3

Review of Existing Horn Antenna Manufacturing Techniques

This chapter briefly explains some of the manufacturing techniques of horn antennas made out of thermoplastic and their tradeoff's. On the following subsections, a brief description of the light weight horn antennas found in literature is given. This kind of description gives a better support in choosing the better manufacturing technique, better outdoor plastic material and suitable conductive paint.

Light weight corrugated horn antenna. In 1997, an S-Band (2 to 4 GHz) Gaussian corrugated horn antenna has been developed for full-earth coverage from a geostationary satellite. This horn was called 'bowl-shaped' because of its distinctive profile [40]. The multihybrid-mode horn has very low side lobes of -36 dB, gain around 20.9 dBi and cross polarization is less that -40 dB at center frequency. This compact horn is made out of aluminium and has a length of $5.6\lambda_c$, aperture diameter $4.6\lambda_c$ and accquires a weight of about 100 kg [40] as shown in Figure 3.1a. Eventhough the developed bowl shaped horn is compact in size and has low sidelobes, it is not suited for spaceborne platform due to heavy weight. Keeping the weight consideration in mind, in the year 2000, the US Defence department commissioned a light weight version of bowl shaped horn for installation on a satellite [28]. The idea of fabricating complex antennas with plastic materials and then coating with conductive paints was first demonstared in [28]. The lightweight horn is illustrated in Figure 3.1b.

The lightweight design was fabricated from carbon-fiber-reinforced-plastic (CFRP) materials by Composite Optics Inc. and in order to increase the electrical conductivity of the horn the interior walls were plated with copper [28]. The final design had a mass of only 9.3 kg, which was 10 times smaller than aluminium prototype horn. Moreover this CFRP horn was also tested for space-qualification tests, where it has proved that it could withstand launch and meet standard space-qualification condtions [28]. Unfortunately, the

horn was never made it into space as the US Defence application was cancelled [28]. The more detailed description about the CFRP bowl shaped horn is available from the article [28]. This article gave an idea that even the electroplated plastics can be used as microwave components.

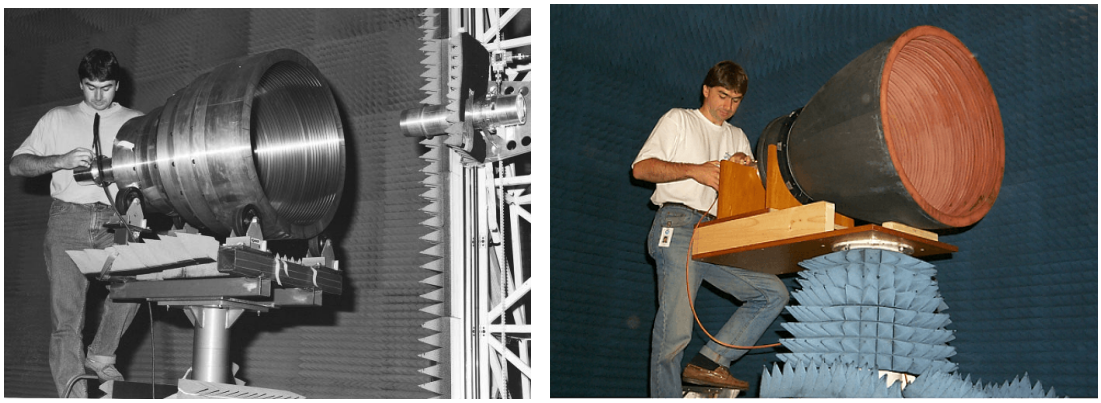

(a) (b)

Figure 3.1: (a): Bowl shaped multi hybrid corrugated horn out of Aluminium [40]. (b): Compact corrugated horn made with CFRP material [28].

In relevant to use CFRP material for the P-band horn antenna , it is well suited material and the only thing to be considered is the cost of the material. Due to the involvement of high cost of CFRP material, it was decided to choose cheap plastic material satisfying the application requirements.

3-D printed Ku-Band corrugated conical horn antenna. The manufacturing technique of Ku-Band (10–16 GHz) corrugated conical horn antenna using 3-D print technology was presented in the paper [7]. The corrugated conical antenna was initially simulated in HFSS. In HFSS it was considerd that the horn was made of ABS plastic and a boundary condition was used on the interior wall of antenna for emulating conductive spray paint [7]. A peak gain of 19.7 dBi and cross polarization levels below 55 dB at 16 GHz were observed from the simulation of corrugated conical horn [7]. Later the antenna was printed using acrylonitrile butadiene styrene (ABS) thermoplastic material by a Fortus 250 MC 3D-printer and then sprayed manually with super shield conductive nickel aerosol 841 paint (From MG Chemicals). The fabricated antenna has a length of 118.8 mm and aperture diameter of 76.4 mm also shown in Figure 3.2. From the measured results, a peak gain of 19.6 dBi was observed and it was stated in [7], the change in gain compared to the simulation results is either due to the surface roughness and non-uniformity thickness of the coating or the loss between the plastic and coating. The detailed description of the fabrication method of the conical corrugated horn and the gain curves can be visualized from [7].

To summarize a few strong points from the article [7], it was noted that ABS thermoplastic material can be used to 3-D print horn antenna and nickel conductive paint 841 from MG chemicals can be used as a conductive coating on the thermoplastic. It was also noted that the 3-D printing technique would allow for producing various microwave and millimeter wave components.

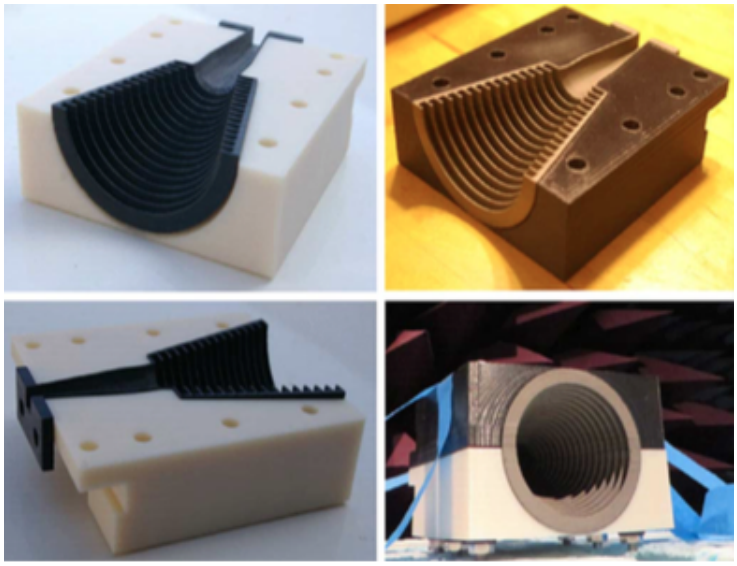

Figure 3.2: 3-D printed antenna coated with conductive aerosol paint [7].

3-D printed plastic conical antenna. In the year 2015, a 3-D printed conical antenna was developed for a frequency of 5 GHz. This antenna was commissioned for radio frequency interference monitoring of the MeerKAT (Karoo Array Telescope) site, located in the karoo region of South Africa [41]. The antenna is conical in shape and is mainly made of ploylactic-acid (PLA) plastic as shown in Figure 3.3a and coated with a carbon-based conductive paint, HSF55 (from YSHIELD, Germany). It has an aperture diameter of 18 cm. The conical antenna is also coated with nickle-based conductive paint, inorder to compare the performance for both conductive paints. It was observed that an antenna efficiency of more than 90% has been obtained upto 5 GHz for simulation and measurement results for both conductive paints and the graph for efficiency is shown in Figure 3.3b. The effect of PLA plastic on the efficiency of the conical horn was investigated and was proved that the PLA plastic didnot contribute to any loss [41].

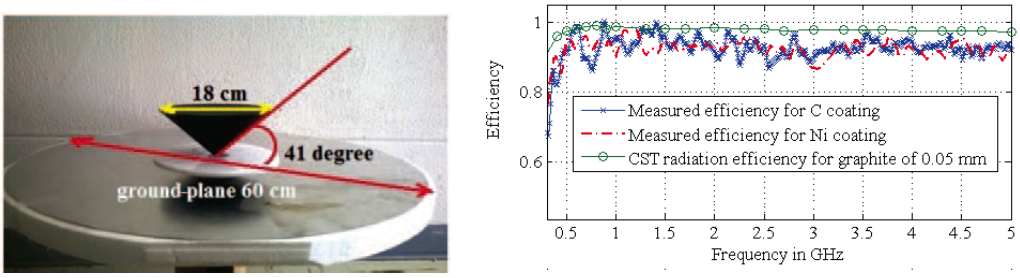

(a) (b)

Figure 3.3: (a): 3-D printed conical antenna [41]. (b): Comparison between measured and simulated efficiencies [41].

To summarize a few strong points from the article [41], it was noted that the performance of HSF55 carbon conductive paint is similar to the nickel conductive paint coated antenna and this would be one of the strong evidence to use cheaply available carbon conductive paint in 3-D printing P-band antenna.

VeGA for C-band. In the year 2014, a prototype scaled to C-band was developed by DLR-HR [1] and is intended to be used for calibration transponders. Actually the scaled prototype called as VeGA horn was aimed in P-band believing that the 3-D printing technique used for C-band could be employed for P-band device. The scaled C-band was manufactured by additive manufacturing technique using polyamide (PA2200) plastic material and top coated with 100 µm thin nickel layer. The length and diameter of the VeGA in C-band constitutes dimensions of 13.8 cm ×16.4 cm. The described process allows for manufacturing of any microwave device, which would be about six times lighter than aluminium. Meanwhile the measurement and simulation results of the VeGA were in full agreement as represented in Figure 3.4b with a gain of 14.9 dBi and cross-polar isolation of more than 53 dB within -15° $\leq \theta \leq$ 15°. This kind of positive encouragement intended for utilizing the additive manufacturing techniques in manufacturing a P-band device with a scaled dimensions of approximately 1.53 m × 2.06 m.

(a)

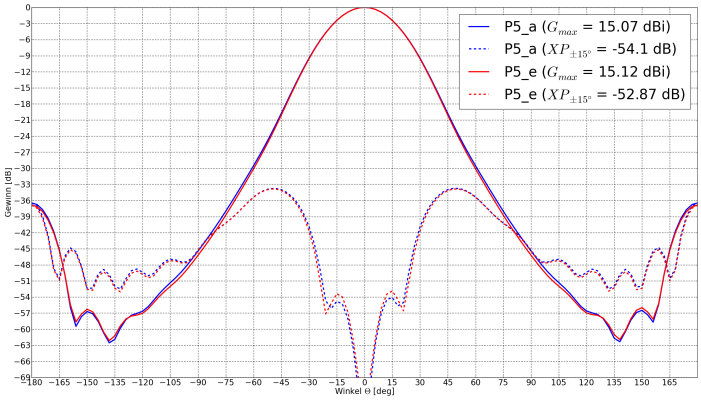

(b)

Figure 3.4: (a): Structure of VeGA developed in [1]. (b): Gain and cross-polarization graphs for simulation and measurement results of VeGA adapted from [1].

The P-band VeGA antenna is mainly deployed for outdoor environments and it is expected to work continuously under temperature variations in the range of -20 to 40 degrees and to have a life time of about 15 to 20 years. But the information on the long term effects of exposure to external environments has not been investigated so far by DLR-HR. Moreover in order to use the 3-D printed P-band VeGA for outdoor environments, the plastic material utilized for C-band antenna is not the right choice where it lacks all these specifications. Also the plastics utilized so far in manufacturing horn antennas failed for outdoor environments, except costly carbon fiber reinforced plastic. Till so far from the chapter 3, it is clear that additive manufacturing technique can be used to 3-D print antenna in plastic and carbon conductive paint can be used as an metallic element on plastic.

So here rises the question, what would be the better plastic material and better manufacturing technique for manufacturing VeGA at P-band? The answer would be explained in coming sections:

3.1 Selection of Outdoor Plastic Material

According to the specifications mentioned in section 1.2, it is necessary to choose the thermoplastic material that suits the application. The most commonly used and easily printable plastic material along with 3D printing is Acrylonitrile-Butadiene-Styrene (ABS) due to its high toughness and rigidity. It was said in [42], the chemical resistance and high strength properties are derived from acrylonitrile, toughness, rigidity and low temperature resistance from butadiene and the hardness from styrene. The ABS is used for instance for lego toys, coffe maker parts, trays, furniture, tool housings, 31% in electronics and 12% in automotive sector [42]. Some of the disadvantages are; it has low heat resistance limiting to 99 ° C, and low tensile strength (6000-7000 psi), susceptible to UV-light

and discolors when exposed to sunlight and also experiments prove that is not intended for outdoor environments. After a thorough research in finding the cheap and suitable outdoor plastic material, it is known that Acrylonitrile-Styrene-Acrylate (ASA) plastic material would be the better choice.

ASA was developed and introduced in 1970s by BASF Corporation and initially it was named as Luran S. ASA terpolymer contains acrylate rubber in the SAN matrix rather than polybutadiene, which makes ASA different from ABS [42]. ASA is similar to ABS thermoplastic but the acrylate component in ASA provides ASA UV-light resistance, heat resistance and exceptional resistance to weathering. ASA is also UV-Stable, meaning that it does not breakdown under prolonged exposure to UV radiation. It has exceptional strength, rigidity, high thermal stability and it ages very well. Perhaps the best quality of ASA material is the incredible surface finished aesthetics it offers. Another leg up ASA has over ABS is that it can be printed with a larger bridging means that ASA parts can be printed faster and with less material. ASA is a go to material for any outdoor applications from consumer goods to exterior vehicle components, tools, fixtures and boat marine parts. A clear description from the Figure 3.5a makes reader understand the properties of ASA and how it is different from the available plastics in the market today.

	Luran S ASA	PP	PVC	ABS	PC Blend	IM PMMA	PVDF & PVF
Gloss							
Control	●	◕	●	●	◕	◐	◐
Initial	●	◕	●	●	●	●	●
Long-term	◕	◒	◒	○	○	●	●
Scratch Resistance	◕	○	◕	◕	◐	●	●
Dimensional Stability	◕	◒	●	◕	●	◐	◒
Heat Resistance							
150°F	●	○	○	●	●	◒	●
200°F	◕	○	○	○	●	○	●
Initial Impact							
RT	●	●	●	●	●	○	◕
-20°F	◕	●	◕	●	●	○	◕
Weathered, RT	●	◐	◐	○	◕	○	◕
Cost/Outdoor Performance	●	◒	● ◒	◒	◕	◕	◐

● Outstanding ◕ Excellent ◐ Good ◒ Fair ○ Poor

(a)

(b)

(c)

Figure 3.5: (a): Comparison of ASA to other thermoplastics. (b): ASA formed as a protective cover for satellite electronics (c) : ASA used on the exterior panel of a golf cart, (adapted from [43]).

In terms of telecommunication industry, ASA is used for parabolic-reflector coverings, mobile antennas, T.V. antenna parts, cable access housings, weather-protection housings for satellite electronics shown in Figure 3.5b, due to its excellent UV resistance capability [43]. ASA can sustain a temperature of 120 ° C, its sustainability for lower tempera-

tures are not mentioned clearly anywhere from the manufacturers of ASA. But some of the weathering tests performed by the BASF corporation proved that they can sustain untill -20° C. The Figures 3.6a, 3.6b, 3.6c show some of the advantageous properties of ASA in comparison to other plastics. These figures are adapted from [43].

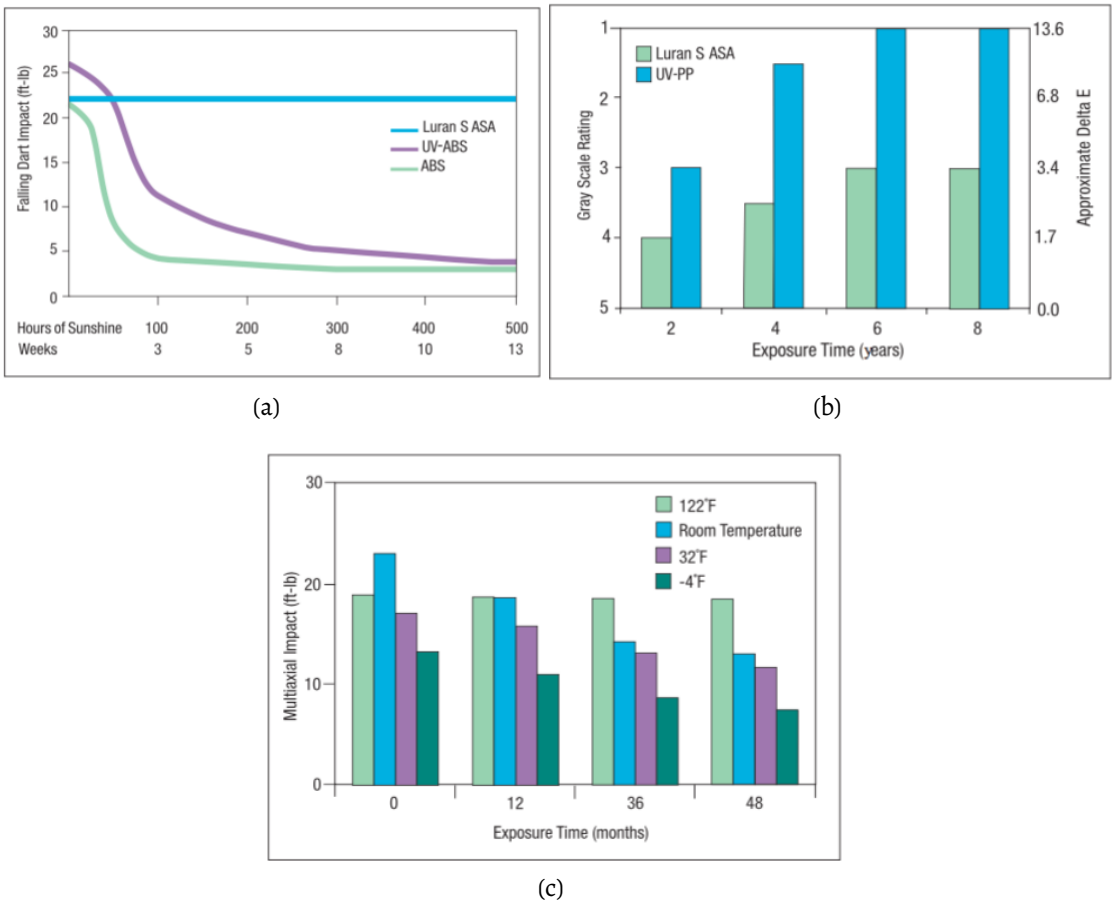

Figure 3.6: (a): Impact resistance tests of ASA plastic compared with UV-stabilized and nonstabilized ABS. (b): Physical properties of ASA over a wide temperature range conducted in Arizona field weathering study. (c): Field studies in Germany show that ASA UV window profiles resist discoloration better than UV-PP [43].

Figure 3.6c, shows that Luran S ASA also beats the long-term performance of UV-stabilized polypropylene (UV-PP) in color retention and surface quality [43]. After 4 years UV-PP shows surface pitting and at 8 years the UV-PP is severly cracked but Luran S ASA didnot pit or crack in the test [43].

To summarize about ASA plastic, ASA plastic offers superior UV resistance, better surface finish, a broader selection of attractive colors and saves money and time with sparse and fill patterns. But the main disadvantages of ASA plastic include generation of toxic smoke when burnt, easily get attacked by concentrated acids, aromatic and chlorinated hydrocarbons. After examining the strong points from Figures 3.6, and 3.5, it was thought-

ful to use Luran S ASA thermoplastic material for manufacturing outdoor P-band VeGA antenna and OMT. The also reason in choosing ASA plastic material for outdoor environments is that it is rather cheaper than the carbon fiber reinforced plastic material (mostly used for outdoors).

3.2 3D Printing Techniques

Having reviewed existing manufacturing techniques and outdoor plastic material in general, this section deals in choosing appropriate 3-D printing technique for manufacturing outdoor P-band antenna prototype. Starting with introduction of 3-D printing, a short overview of different and most prominent 3-D printing technologies is described and finally this overview links in choosing appropriate technique.

Over the recent years, technology has improved in replacing metals with plastics in the manufacture of computers, industrial machines, automotive sector, telecommunications and other electronic equipment. In order to correlate with the thesis work, an advantage has been taken in manufacturing or 3-D printing complex antennas in terms of plastic materials. 3-D printing is a process of making three-dimensional solid objects from a digital computer aided desin (CAD) file. It is an additive manufacturing process where an object is built-up layer-by-layer until the final geometry is obtained. The techniques used for building or printing the parts layer-by-layer vary significantly between different 3-D printing technologies. 3-D printing technologies are used in automotive sector, aerospace hardware, medical and health care, electronics and packaging and military hardware. Some of the mostly used 3-D printing technologies are explained below:

SLA, Stereolithography technology. It is the oldest rapid prototyping technology from 1980s. Stereolithography utilizes an ultraviolet light beam to build parts out of liquid photopolymer instead of extruding plastics [44].As the laser scans the surface of the liquid photo polymer which is solidifying, the build platform is lowered subsequently and the part is built layer-by-layer.

Advantages and Disadvantages. It has the ability to print parts with very good accuracy and surface finish. Every printing technology needs some support structures to prevent the part from collapsing. Once the part is printed then the support structure can be easily removed. However, stereolithography works only for photo polymer materials which are not expensive and mechanical strength is low. It is also not considered for outdoor applications due to the photo-reactive resins involved in the process. Moreover stereolithography is mostly used for "show and tell" parts and visual prototypes, which might not be suitable technology for manufacturing outdoor P-band antenna prototype.

Polyjet technology. Polyjet process uses high-resolution ink-jet technology to produce parts quickly and economically. It is similar to ink-jet technology but instead of jetting ink it jets layers of liquid photoploymer or UV-resin as thin as 16 microns to build models and prototypes with extremely complex geometries, fine details and smooth surfaces [44]. The support material used in polyjet technology is a gel-like substance, which can be easily washed away. It works just like an office paper printer. Polyjet is used for models with fine details or rubber like materials.

Advantages and Disadvantages. The materials involved in usage of polyjet technology are Verowhite plus, polyjet flex and over-mold which are UV-active photopolymers and are not durable over time. This technology is applicable in the areas where accuracy and surface finish are essential for a component. As polyjet technology is not compatible with standard materials, this would not be a right option for P-band antenna.

SLS, Selective Laser Sintering technology. It is an additive layer technology that uses a laser to sinter thermoplastic materials, most commonly used plastic is nylon. It is a powder based machine, similar to binder jetting technology but uses CO_2 laser to melt the surface of powder, creating a layer of the printed material. It has the advantage of producing parts with fine detail and creates high resolution parts [44]. SLS commonly used materials are polyamide PA, Flex (Black elastometer), Alumide, Titanium, Metal and wood. The SLS is mainly used in aerospace industry because the objects used are printed in high quality materials.

Advantages and Disadvantages. The SLS technology has ability to produce parts ranging from plastics to ceramics to metals. The disadvantages of this technology are very expensive peripherals, heavy post processing, rough surface finish and expensive to run. The parts do not have exactly the same properties as their injection molded counterparts [44]. Due to the non-availability of ASA in powder form, SLS technology would not be the right option for usage in outdoor application.

MJM, Multi Jet Modeling. It is an emerging technology which cure UV curable acrylic plastics and support materials. It actually lays down microscopic layer resin on a plate and the layers are laid as the plate drops down creating the part [44]. It is good for small parts and this technology is mostly employed in casting applications like dental, jewellery because of smooth interior and exterior surfaces.

Advantages and Disadvantages. Material jetting can achieve very good accuracy and surface finish. However the technology is compatible only with wax-like materials and

moreover the mechanical strength of finished parts is poor and difficult to coat paint on the part 3D-print.

Binder jetting technology. It is one of the latest modeling techniques which uses standard inkjet technology, where the inkjet print heads print the cross-sectional area layer-by-layer by depositing a liquid binder onto thin layers of powder. This technology is better in creating parts for presentation models, because it has the capability in printing in different colors.

Advantages and Disadvantages. Binder Jetting works with almost any material that is available in powder form. The process is fast, simple and cheap as powder particles are glued together . Parts produced with the technology results in fragile parts having limited mechanical properties. It cannot simulate plastics and the surface finish, accuracy is not good when compared to other additive manufacturing technologies.

FDM, Fused Deposition Modeling technology. FDM is a process where a V-doved thermoplastic is extruded out of a nozzle and laid down on the built platform, where it cools and solidifies. The nozzle moves in X-Y plane and the filament is laid down layer by layer building the part. It uses modeling materials and support material to execute a print job. The support material can be removed by high PH water-based solvent.

Advantages and Disadvantages. This technology is widely known for its speed, accuracy, and competitive cost. It is the affordable 3D printing process compared to the other technologies and also the only 3D printing technology where a real thermoplastic can be available, which means that the parts printed with this machine have excellent mechanical, thermal and chemical qualities. FDM involves usage of standard materials like ABS (Acrylonitrile Butadiene Styrene), Polylactic acid and also materials from acrylic family namely ASA (Acrylonitrile Styrene Acrylate). FDM technology is used in variety of industries from automotives to consumer goods manufacturing. The cons include, poor surface finish, process is slow for large parts and support structures are needed.

After a short overview and comparison of different additive manufacturing technologies, FDM technology would be the suitable technique for manufacturing outdoor antenna prototype. The reason for choosing FDM because, the most priority ASA plastic material available in filament instead of powder form is compatible with FDM technology rather than the other technologies.

Characteristics	SLA	Polyjet	FDM	SLS	MJM	Binder jetting
Maximum build envelope, mm^3	2100 × 700 × 800	1000 × 800 × 500	914 × 610 × 914	550 × 550 × 750	300 × 185 × 200	4000 × 2000 × 1000
Minimum feature size,mm	0.1	0.15	0.178	0.15	0.1	0.1
Minimum layer thickness, mm	0.016	0.016	0.178	0.1	0.013	0.09
Tolerance, mm	± 0.15	± 0.025	± 0.178	± 0.25	± 0.025	± 0.13
Print speed	Average	Fast	Slow	Fast	Fast	Very Fast

Table 3.1: 3-D printing process comparison chart, from [44].

3.3 Selection of Suitable Coating Materials for Conductivity

In principle to form any plastic material as an antenna element, the plastic has to be either conductive or has to be coated with conductive paint. Taking the proof of the information from the publication [41], a short description of the cheap and readily available conductive paints in the market today are discussed in the following sub sections. This kind of description helps in studying and selecting suitable conductive paint for P-band antenna.

Super Shield Nickel Conductive Paint

The super shield nickel conductive coating is a conductive acrylic paint designed to reduce electromagnetic or radio frequency interference [45]. The high-purity nickel flakes in the paint creates an overall feature of behaving the paint as conductive. A 38 µm thickness of super shield nickel coating has a surface resistivity of approximately 0.3 ($\Omega/square$) [45]. The measurement values provided by the manufacturer are not accurate as they are performed using square probe, which is not the right tool in measuring precise values. Even the articles [7], [41] on plastic horn antennas, the conductivity values are not properly measured and their approximate values were taken for simulations. Hence to properly account for the paint, its conductivity is necessary and their accurate values can be determined using four probe or eddy current sensor method.

Advantages. Super shield nickel paint is corrosive resistant better than pure copper fillers [45]. It is more durable than silver or copper fillers and in addition the nickel coating is easily removable or repairable to re-establish the desired shielding performance in case of degradation [45]. Nickel coating adheres to most of the plastic materials like ABS, Poly carbonate and also ASA and can be easily applied by paint brush or spray gun.

Disadvantages. Proper safety measures has to be taken while using nickel paint for examples wearing protective clothes, safety glasses etc. Super shield nickel paint is not readily available in European markets except United Kingdom.

Applications. Nickel paint is primarily used in coating interior of plastic electronic enclosures, telecommunication equipment, industrial equipment, medical and military devices and aerospace equipment. It is also used to shield entire rooms [45].

Carbon Conductive Paint

The other alternative paint next to super shield nickel conductive coating is Carbon conductive coating, HSF44 [46]. This paint is manufactured by YSHIELD. It is used for protection against high and low- frequency electromagnetic fields. Based on a high quality pure acrylic binder, this shielding paint offers a perfect compromise of excellent attenuation and high water resistance. The carbon shielding paints do not contain any metal flakes but a mixture of carbons, resulting in chemically stable and permanent corrosion-free, even in damp environment.

Applications. The figure 3.7 show that carbon conductive paint is mostly used on the interior and exterior walls for protection against electromagnetic waves and is also recoated preferably with plastic bonded emulsion paints, silicate emulsion paints, facade paints and silicone resin paints. The carbon conductive paint is also used in commerce, science, research and defence facilities to prevent interception of data from wireless networks (data-stealing) also to protect potentially bugged conference rooms or to shield technical equipment [46].

Figure 3.7: Some of the applications where carbon conductive paint is coated (adapted from [46]). From the Figure it can be observed that a man started painting a house with carbon paint (left most and middle figure) and in order to protect the carbon paint, it is top coated with a white paint (right most).

Advantages and Disadvantages. The carbon conductive paint can be easily applied without taking any precautions and as per information provided by the manufacturer, the shielding attenuation of HSF44 does not degrade over years. The main disadvantage is

it is not scratch resistant and it requires a top coat to protect HSF44 paint.

It can be drawn to a conclusion that both Nickel and Carbon conductive paint can be used for the both plastic OMT and Horn.

3.4 Conclusions

To sum up, the following contributions are made in this chapter:

- Firstly, in section 3, the different types of lightweight antennas mostly manufactured out of plastic material and coated with conductive paints were introduced. This kind of review helps in incorporating an approachable technique (the technique which satisfy the antenna requirements from Tab. 1.1 for manufacturing a P-band horn antenna.

- In the following section 3.1, an overview about the different plastics available in the market till date is given. Finally a choice was made to select a suitable plastic material (ASA plastic) which satisfies the lightweight and outdoor antenna requirements illustrated in Tab. 1.1. To follow up, in the section 3.2, a short review is given about the different 3-D printing techniques and finally ASA plastic material compatible FDM based 3-D printing technique was selected to manufacture the P-band antenna.

- Finally, in section 3.3, a review about the cheap and available conductive paints and their applications, advantages and disadvantages were given. This helps in opting a suitable conductive paint for our application.

Hereby in coming chapters a clear cut step by step process is given explaning the adaptation of the existing antenna model [1], [2] to P-band and analyzing the radiation properties of different horn antenna designs by performing simulations in FEKO Suite 7.0 [47]. Also, analyzing the adaptation of developed P-band antenna model to deformations, implementing the main idea of adapting perfect electric conductor (PEC) P-band antenna model to plastic material and conductive paint, would be explained and analyzed with the help of simulations in coming chapters.

Chapter 4

Adaptation of VeGA and OMT for P-band and Respective Numerical Simulations

In 2014 and 2015, at the DLR-HR, a compact corrugated horn antenna, so called VeGA and orthomode transducer prototype were developed, which were built in C-band [1] [2]. The long-term goal was to base a P-band horn design on this C-band prototype. This chapter addresses the transition and the necessary modifications in going from C-band to P-band. In this chapter 4, the combination of VeGA and OMT is often referred to as an antenna model.

This chapter aims to provide a short discussion about OMT and also provides detailed description of necessary modifications implemented on C-band VeGA and OMT presented in [1], [2]. The previously developed model did not consider standard P-band circular waveguide dimensions and the cross-polarization requirements at P-band were not satisfied. Hence to overcome this limitations, one of the main objective of this thesis is to develop a 3-D print VeGA and OMT model at P-band, by considering standard circular waveguide dimensions and modifying necessary parameters as to achieve design requirements shown in Tab. 1.1. Initially the antenna model is developed at P-band and simulated results were analyzed using the electromagnetic software FEKO Suite [47]. Perfect Electric Conductor (PEC) is used in modelling the antenna. All the simulations presented in the thesis are performed using the commercially available electromagnetic field simulation software FEKO [47] and a 32-CPU computer has been used in order to run analyses in parallel at any time.

4.1 Optimization of VeGA at P-band

Figure 4.1 represents a cutplane CAD model of VeGA. The throat profile of VeGA in Figures 4.1a acts as a mode converter which is responsible for converting the fed circular

waveguide mode TE_{11} to the desired hybrid mode HE $_{11}$. The other advantage of having a choked profile or horizontal corrugations at the throat section of VeGA is to have a shortest antenna profile. The fundamental parameters highlighted in the Figure 4.1a at the throat section are the waveguide radius r_0, γ controls the flare angle, the width and depth of a groove S_{dt}, W_{st} and width of the ridge W_{rt}. The converted HE_{11} mode travels with a gaussian profile in the flare section, which ideally merges in the ψ_{00}- fashion before it is radiated into far field. In Figure 4.1b, the fundamental parameters highlighted at flare section are namely: depth of a slot S_{df}, width of the groove and ridge W_{sf}, W_{rf} and y is the gaussian flare aperture radius. The in detail description of cad design of VeGA can be found in [1].

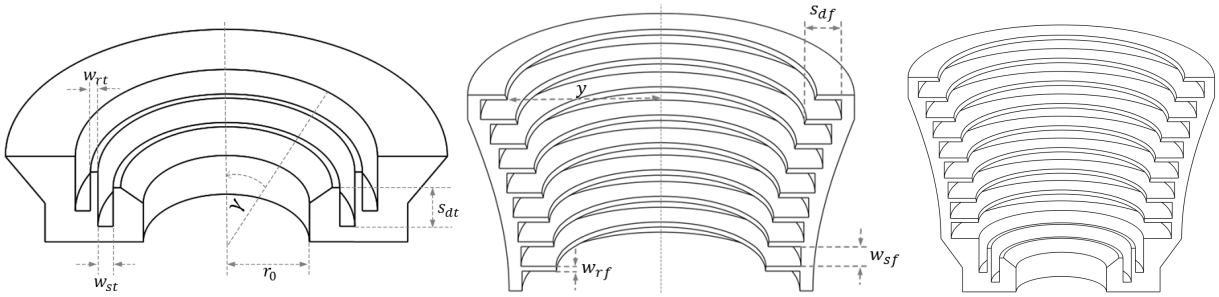

Figure 4.1: (a), (b), (c): VeGA Throat Section, Flare Section, VeGA Profile.

As it is already discussed that the previously developed models in [1], [2], did not consider standard P-band circular waveguide dimensions. One of the main objective of the thesis is to develop the existing models considering standard circular waveguide dimensions at P-band and moreover the developed horn antenna and orthomode transducer in P-band must satisfy the design requirements illustrated in Tab. 1.1. In order to achieve the requirements in Tab. 1.1, the existing antenna model (both C-band horn antenna and orthomode transducer) must be either scaled by a factor of 12.4 times to realize in P-band or a numerical optimization must be performed in numerical simulations. In this section 4.1, only optimization of VeGA is presented.

By considering the standard dimensions of P-band circular waveguide radius (0.27 m) [48], initially the existing C-band antenna model [1], is scaled by a factor of 12.4 times to realize in P-band and the scaled model which includes P1_a set of parameters is simulated and the simulation results represented as P1_a are shown in Figure 4.2. Later on considering standard P-band circular waveguide radius, a numerical optimization for VeGA is performed in FEKO by mainly changing the parameters in the throat section as shown in Table 4.1. It was mentioned in the thesis [1], that the throat section is sensitive to cross polarization and directivity, which is one of the reason for altering the parameters in the throat section. After the optimization runs, the requirements listed in Tab. 4.1 could be

fulfilled. The parameter x and t represents number of corrugations at throat and flare section. By considering the set of six parameters from the Table 4.1, the VeGA antenna was simulated in a numerical simulation tool and the simulation results are shown in Figure 4.2. Figure 4.2 shows the gain and the cross-polarization curves for the six set of parameters mentioned in the Tab. 4.1. The reason for considering the cross-polarization isolation value within the requirements for -15° $\leq \theta \leq$ 15° because within this requirement a maximum θ angle deviation is expected between the satellite and the transponder beam in practice [2].

Simulation	γ/°	x	W_{st}	W_{rt}	S_{dt}	t	y	S_{df}	**Length/m**	**Aperture Radius/m**
P1_a	50	2	2/25	1/25	1/4	9	1.3	1/4	1.67	2.18
P2_a	55	2	2/25	1/25	1/4	8	1.2	0.27	1.52	2.04
P3_a	60	2	2/25	1/25	1/4	8	1.2	0.27	1.46	2.04
P4_a	55	3	2/25	1/25	0.3	8	1.2	0.27	1.59	2.07
P5_a	55	2	2.25/25	1/25	1/4	7	1.2	0.27	1.37	2.03
P6_a	55	2	2.25/25	1/25	1/4	8	1.2	0.27	1.50	2.05

Table 4.1: Overview of parameters for six simulations.

From Figure 4.2, it can be observed that for P1_a simulations the gain greater than 15 dBi is obtained and cross-polar component is $\geq$ 50 dB, which satisfy the design requirements mentioned in Tab. 1.1. But it has to be noted here that the P1_a simulations are performed without considering standard P-band waveguide dimenisons. Here one can observe the changes in parameters from Tab. 4.1 and their corresponding simulation results in Figure 4.2. Out of the six set of parameters from the Table 4.1 only P6_a was considered to satisfy the requirement with respect to Gain $\geq$ 15 dBi, cross-polar isolation $\geq$ 50 dB in the relavant range of -15° $\leq \theta \leq$ 15°, side lobes $\leq$ -36.5 dB and compact in size compared to other horn designs presented in the Tab 4.2. Also the developed appropriate design P6_a has length of 1.50 meters which is 0.17 meters smaller than the existing model presented in [1]. Overall the simulation results prove that the change in parameters at antenna throat section is sensitive to gain and cross-polarization components of VeGA. However with the P6_a set of parameters, simulations resulted in lowest cross-polar components at sufficiently high gain and compact in size when compared to other choked GPHA designs. Nevertheless, to achieve the requirements for a compact corrugated Gaussian horn antenna at other frequencies (like L-band), along with scaling necessary numerical optimization must be performed. Moreover the developed P-band VeGA model with P6_a set of parameters is used for further analyses in the thesis.

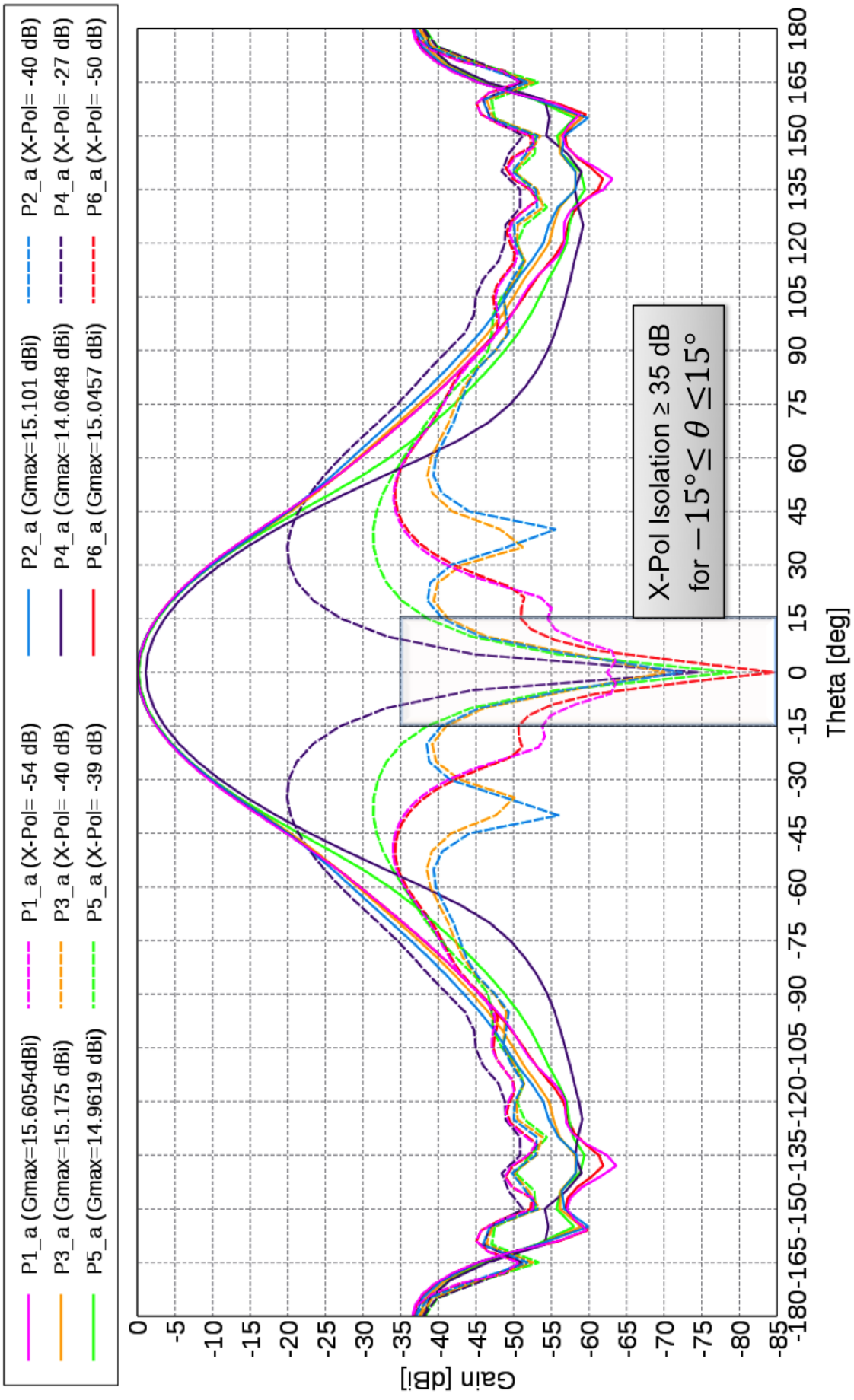

Figure 4.2: Simulations for Gain and Cross-Polarization for the set of six parameters from Tab. 4.1.

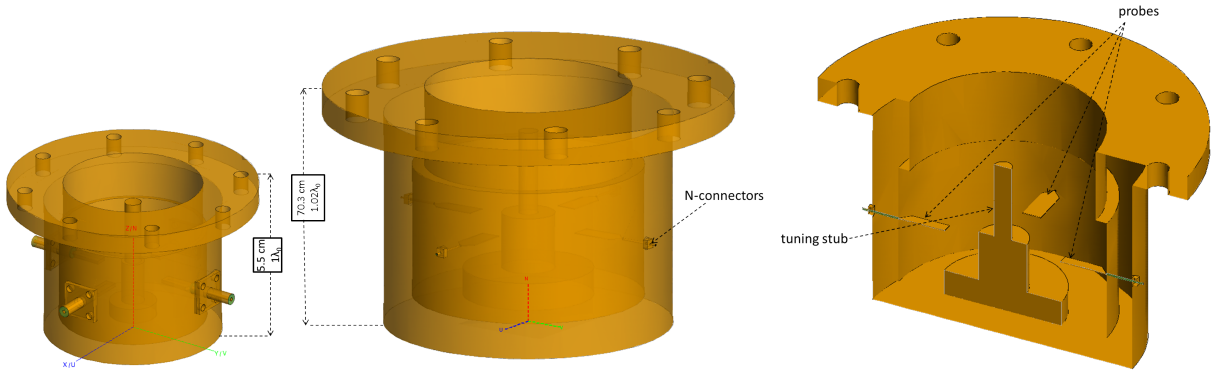

(a) (b) (c)

Figure 4.3: (a): Isometric view of 5.5 cm C-band OMT [2]. (b): Isometric view of 70.3 cm P-band OMT. (c): Cutplane view of P-band OMT with details of tuning stub, N-connectors and copper probes inside the cavity.

4.2 Orthomode Transducer

The developed P-band VeGA still lacks a proper feeding system. The feeding system which is subjected to be used for P-band VeGA should have dual linear polarization capabilities, high electrical performance, compact in size and finally the feeding system should not limit the performance of VeGA concerning gain and cross-polarization requirements. By considering the requirements, a compact orthomode transducer (OMT) was developed and manufactured in 2015 by DLR-HR and the work was presented in [2]. So what is an OMT?

An OMT refers to as an Orthomode Transducer is a passive microwave device, which serves as an antenna feed system. The device is capable of separating (or combining) orthogonal polarizations within the same frequency Band [2]. This device can be mainly used for any application where a dual polarization requirement is needed. Before OMT's, in order to support dual polarization capability, most of the applications uses two antennas for receiving the signals. In case if a dual polarization requirement is needed at lower frequncies, it requires a heavy and large apparatus. So instead of using two antennas for dual polarization, a single antenna can be employed for receiving two different polarization signals. This can be possible only when a Orthomode transducer is used as a feed element. The information available from different polarization signals can be combined to distinguish and categorize distributed targets [2]. Figure 4.3a, shows a developed C-band OMT model. The OMT consists of a tuning stub, a pair of probes and set of N-connectors. More information of a compact OMT is explained in [2].

Optimization of Orthomode Transducer. The main concern about OMT in this work is to develop the C-band compact OMT model [2] to P-band, inorder to use the developed

model as a feed for the P-band VeGA. So the C-band OMT model is scaled by a factor of 12.4 times to realize in P-band. The isometric and cutplane view of scaled OMT model can be seen in Figures 4.3b, 4.3c. It is also important to notice that scaling by a factor of 12.4 does not give desired results. So in order to extract the best performance of the orthomode design, some of the sensitive parameters need to be optimized. The most important parameters to be optimized are the height and diameter of the tuning stub. The remaining parameters such as placement of N-connectors, backshort distance, waveguide transformer and circular waveguide crossection for OMT were calculated using a set of equations provided in [2].

The primary tool for all simulation analysis and optimization process were performed in electromagnetic software FEKO Suite 7.0 [47]. FEKO is an electromagnetic simulation software that uses the method of moments (MoM) as the default solution method. The optimization process used genetic algorithm method (GA) in order to optimize six parameters at a time. The optimized P-band OMT has a length of 1.02 λ_0, which is almost 70 cm. Figure 4.4 shows the S-parameter simulations of P-band OMT. It can be observed from the plot that, for the center frequency, the developed P-band OMT has a return loss greater than -30 dB and cross-polarization > -90 dB.These simulation results show that the developed optimized model satisfy the requirements mentioned in Tab. 1.1. Once the developed OMT model showed convincing results, it is important to verify the developed OMT model when combined with VeGA has no any effect on the radiation properties of the P-band VeGA. This verification is explained in the Section 4.3.

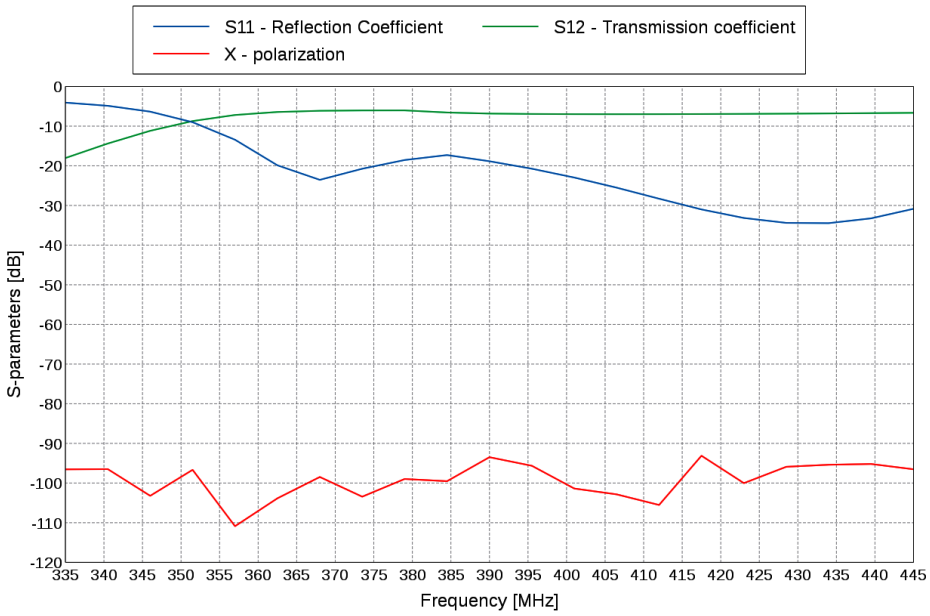

Figure 4.4: Scattering parameter simulations of P-band OMT.

4.3 OMT as a Feed for VeGA

Figure 4.5 compares the far field radiation patterns generated by VeGA and also the patterns generated by the combination of OMT and VeGA. The combination of OMT and VeGA has a length of $3.21\lambda_0$. The VeGA is excited by a single fundamental TE_{11} mode whereas the combination of VeGA and OMT are excited by a pair of fundamental coaxial modes with 180° phase difference between them [2]. Both models were mainly compared to observe any difference in the gain, cross-polarization, side lobes and back lobes. But at a single glance from the Figure 4.5, it is difficult to distinguish any exact difference between them. So proper analysis must be required from the electromagnetic field simulations for both VeGA and combination of VeGA with OMT.

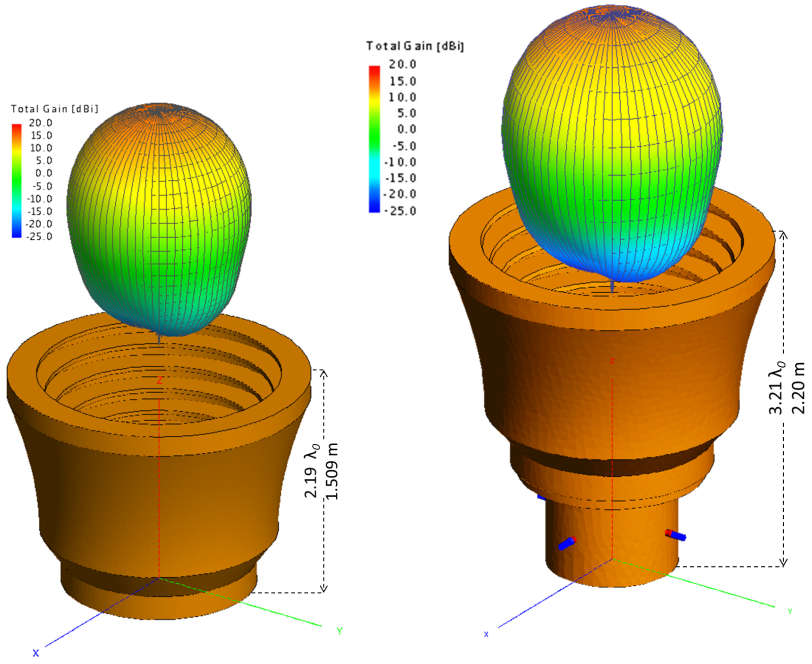

(a) (b)

Figure 4.5: Far field simulated radiation patterns (P-band). (a): VeGA pattern (b): Pattern for the OMT connected to VeGA.

In Figure 4.6, a Cartesian plot representing total gain and cross polar component traces are plotted as a function of the θ angle for both VeGA and for the combination of VeGA with OMT. From the Cartesian plot it can be seen that the gain for VeGA and combination of OMT with VeGA are almost similar having a gain value of 15.04 dBi. Similarly, when the cross-polarization is compared for both models, the VeGA and the combination of OMT with VeGA achieves a cross-polar isolation of atleast 50 dB and is essentially better than the required 35 dB in the interval of $-15° \leq \theta \leq 15°$ and with a minimum of 85 dB for VeGA and a minimum of 95 dB for the combination at $\theta = 0°$. From the simulation results presented in Figure 4.6, it can be observed that introduction of OMT does not show any influence on

the radiation patterns of VeGA. Here the cross polar component traces are presented for $\phi = 45°$ because at this angle a worst case cross polarization can be observed.

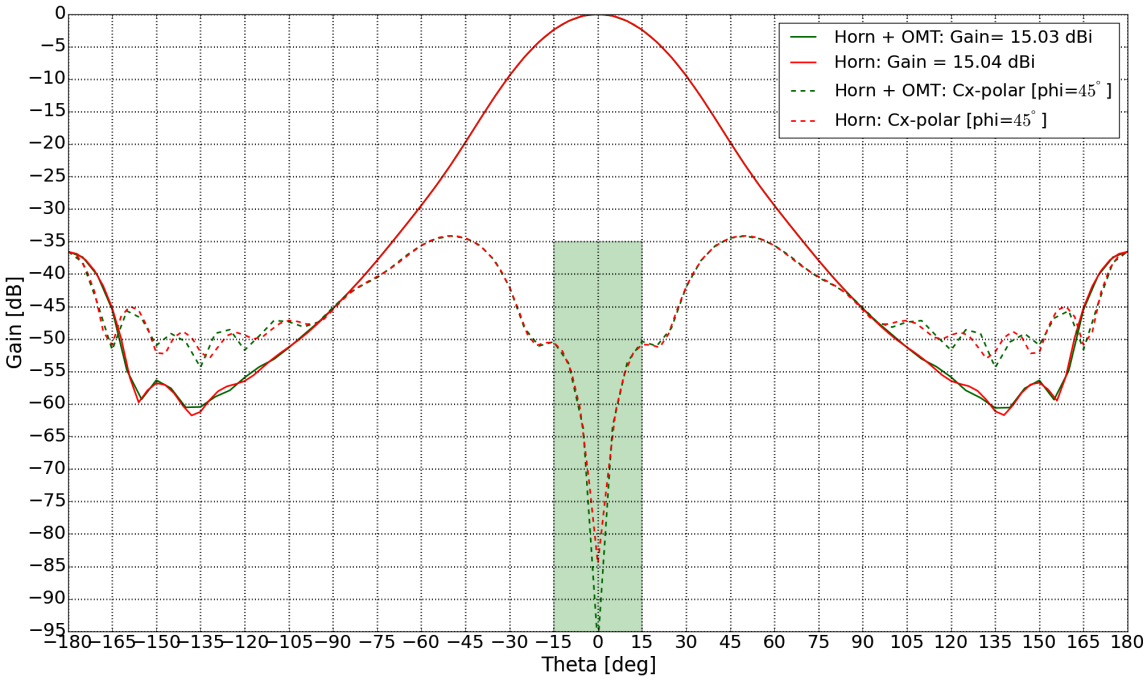

Figure 4.6: Total gain and cross-polar component (X-Pol) for the horn and for the combination of OMT and horn as a function of viewing angle θ. The gain and cross-polarization of the horn antenna and the combination of horn with OMT are similar satisfying the antenna requirements from Tab. 1.1.

Figure 4.7 and Figure 4.8 present far field cuts for the planes at $\phi = 0°$ and $\phi = 90°$, in polar form. A better perspective of the field perturbations introduced by the orthomode transducer can be observed in far field cuts [2]. From these polar plots, it can be seen that back lobe and main lobe of VeGA and combination of VeGA with OMT remain unaltered. Both models have a side lobe of 36.5 dB. Hence from the plots it can be strongly confirmed that introduction of OMT almost has no any effect on the radiation patterns of VeGA.

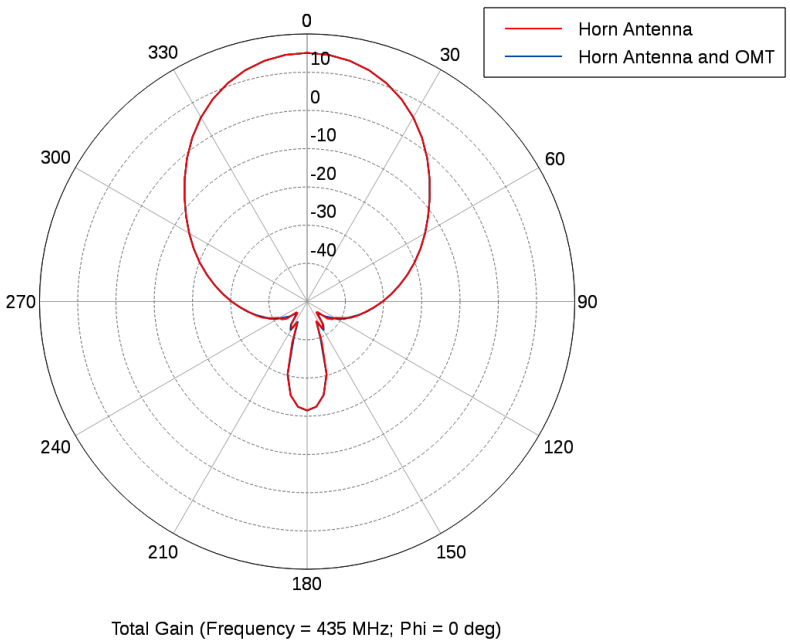

Figure 4.7: Polar plot comparison for the far field generated by the horn alone and by the combination of OMT and horn. $\phi = 0°$ cut (E-Plane).

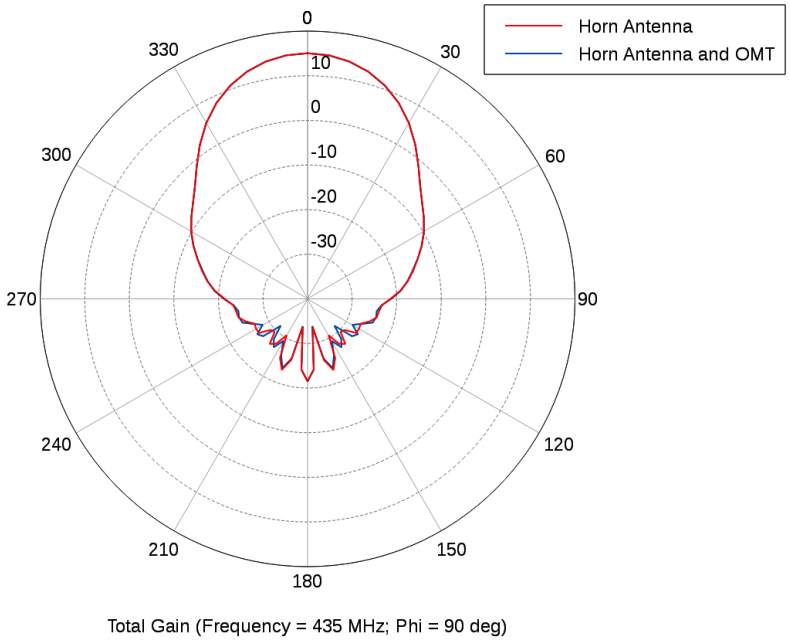

Figure 4.8: Polar plot comparison for the far field generated by the horn alone and by the combination of OMT and horn. $\phi = 90°$ cut (H-Plane).

4.4 Simulation of Mechanical Imperfections

The developed 2.2 meter long P-band antenna and OMT model are subjected to be used for outdoor environments. So when such kind of large model with or without a protective radome is employed in outdoors, there would be a possibility of deformations in the model. The deformations analyzed in this chapter are either due to thermal deformations, environmental loads or either due to misalignment and manufacturing imperfections in the model.

In this section the adaptataions of the antenna design for possible deformations is shown. The deformation was analyzed by taking an ideal mesh of VeGA and deforming it in a mesh tool such as Blender 2.77a [49], and the deformed mesh is imported into FEKO to run numerical field simulations. The deformations were studied qualitatively for the following cases:
- Deformation due to thermal stress
- Deformation due to mechanical stress
- Extreme mechanical deformation, e.g. due to heat
- Manufacturing imperfections

4.4.1 Deformation due to Thermal Stress

A typical shape deformation can be seen in Figure 4.9. It was assumed that the antenna model is placed in the outdoor environment in a slant position and when the model is exposed to continuous high temperatures of sunlight, a bulge shape is formed on the top of antenna model as seen in Figure 4.9. But such observed bulge would might be a rare case because the used ASA plastic is UV-resistant which can sustain high temperatures above +60°. It is also important to note from the Figure 4.9 that by what factor the deformation has occurred is not known. Meanwhile the simulations were performed for the combination of deformed VeGA and OMT is shown in Figure 4.10. From the simulations, the gain and cross-polar isolation for deformed and undeformed antennas satisfy the design requirements.

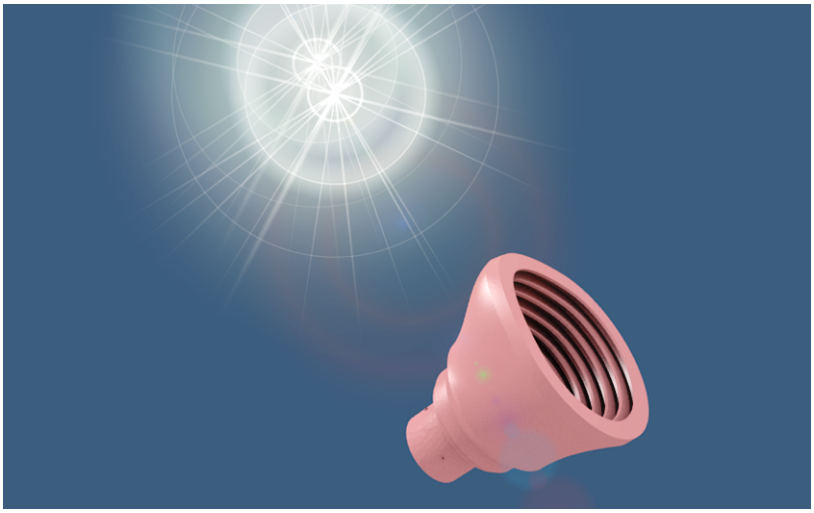

Figure 4.9: Deformation due to thermal stress induced by sun.

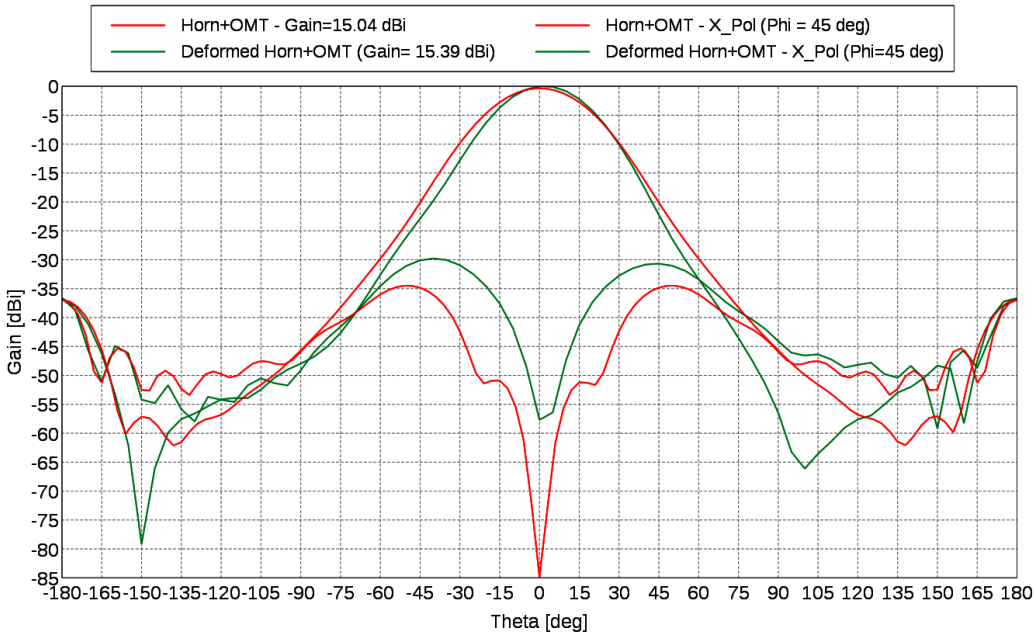

Figure 4.10: Total gain and cross-polar component for the deformed and undeformed combination of OMT and horn as function of viewing angle θ. From the simulation of the analyzed deformation, the minimum cross-polarization of the deformed model (green curve) is slightly reduced to 55 dB in the relevant range satisfying the design requirements illustrated in Tab. 1.1.

After observing the simulations in Figure 4.10, it can be concluded that the cross-polarization of a deformed antenna due to thermal stress is not that critical and is still acceptable for a P-band transponder antenna as it satisfy the design requirements illustrated in Tab. 1.1.

4.4.2 Deformation due to Mechanical Stress

From Figure 4.11, it can be observed that the VeGA is shrinked on one particular side. The deformation due to mechanical stress was created with a thought that the gravitational forces may influence modifications in the shape of antenna effecting the ridges. The other possibility of such stress may be either due to wetting and aging of antenna. The deformation represented in Figure 4.11 is only an assumption, so by what value the antenna model has shrinked and the behavior of ridges in VeGA is not known. It was studied in a manner that in case if such kind of scenario shown in Figure 4.11 takes place, how the radiation properties of the antenna model are effected. The behavior of antenna model for such kind of deformation is analyzed using simulations and are shown in Figure 4.12. From the simulations shown in Figure 4.12, it can be observed that gain is reduced by 0.23 dBi and the cross-polar isolation is atleast 28 dB in the relevant range of -15° $\leq \theta \leq$ 15°. Finally after observing the simulation results for the deformed antenna due to mechanical stress, it can be confirmed that the deformed antenna does not satisfy the design requirements and can no longer be used for any applications.

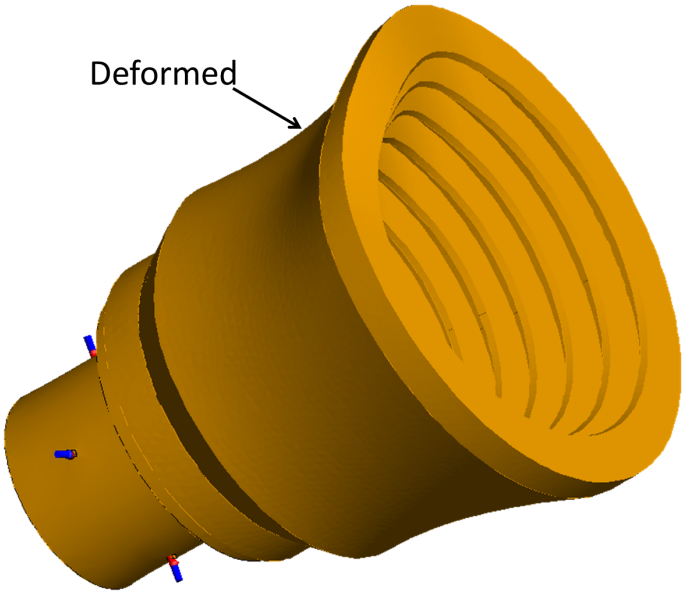

Figure 4.11: Exemplary deformation of the antenna model due to mechanical stress. This kind of deformation is assumed to be occurred either due to the gravitational forces or wetting and aging of the antenna model.

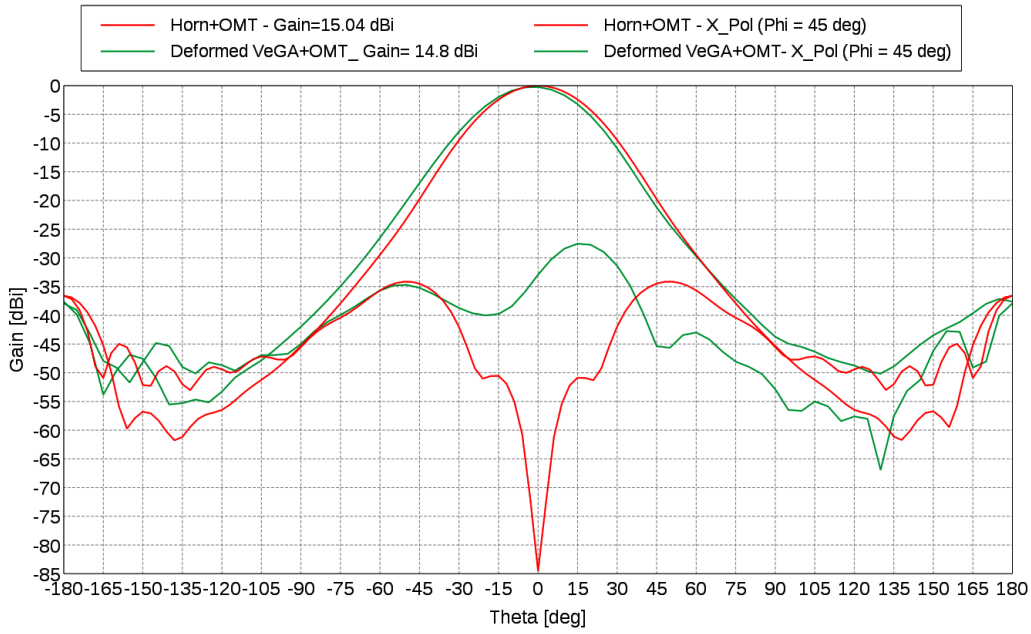

Figure 4.12: Total gain and cross-polar component for the deformed and undeformed combination of OMT and horn as function of viewing angle θ. One can observe that even though the gain of the deformed model (green curve) and undeformed model (red curve) remain same, but the cross-polarization of the deformed model is reduced violating the cross-polarization requirements from Tab. 1.1.

4.4.3 Extreme Mechanical Deformation

Figure 4.13 represents deformation of antenna model due to environmental loads such as winds, heavy rains. The deformation of antenna model caused by environmental loads can be expected as long as the aperture diameter of VeGA is not closed by a protective cover. The reason is that when the wind is in the direction of VeGA, the storm enters into the opening of antenna and has no chance for leaving out from the antenna as it is connected to OMT. The antenna model presented in 4.13 is expected to be the worst case deformation and the simulation results helps in studying the behaviour of the deformed antenna due to environmental loads. From the cartesian plot shown in Figure 4.14, the gain for deformed antenna model is reduced by 1.78 dB and has no longer a gaussian shape. It can be also observed that the cross-polar isolation for the deformed antenna is in between 25 dB and 33 dB in the relevant range $-15° \leq \theta \leq 15°$, where these values are not acceptable for the Biomass mission. From the Figure 4.13, it has to be noted that, for simulating the mechanical deformed antenna model, only circular waveguide mode is considered to be excited during simulation because it has become hard to combine the mechanical deformed VeGA and OMT in FEKO suite [47]. The other reason for considering only VeGA is that, for strong winds the OMT gets badly affected by damaging the probes. In case if OMT is considered to be deformed for such environmental deformation, it can be easily understood that there would not be any simulation results.

Figure 4.13: Exemplary deformation of the antenna model due to environmental loads such as winds and rain.

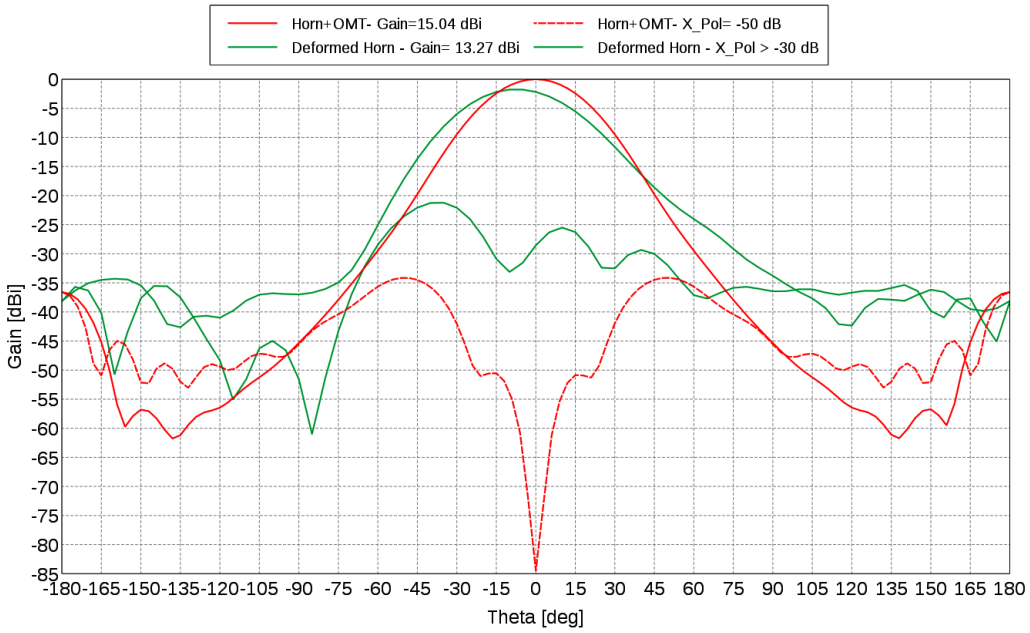

Figure 4.14: Total gain and cross-polar component for the deformed and undeformed combination of OMT and horn as function of viewing angle θ. From the simulations of the analyzed level of deformation (blue curve), it can be observed that the gain and cross-polarization is notably reduced violating the antenna requirements illustrated in Tab. 1.1.

4.4.4 Manufacturing Imperfections

Figure 4.15 shows the cutplane view of VeGA and even some imperfections are visible on the surfaces of ridges. It is quite common that there might be imperfections or surface roughness in the structure when manufacturing any model. The imperfections mostly depend on the type of manufacturing technique involved. Before directly going to manufacture the P-band antenna model, a sample segment was manufactured using additive

manufacturing method a filament based method, resulted in no minor imperfections or surface roughness on the sample segments. Although it was sure that there won't be any imperfections manufacturing the P-band antenna model using filament based method, a rare case of imperfection is considered in order to study the influence of surface roughness on the radiation properties of antenna model. By considering the rare case imperfections, random surface roughness were created in the inner surface of VeGA and later simulations were performed in numerical simulation tool.

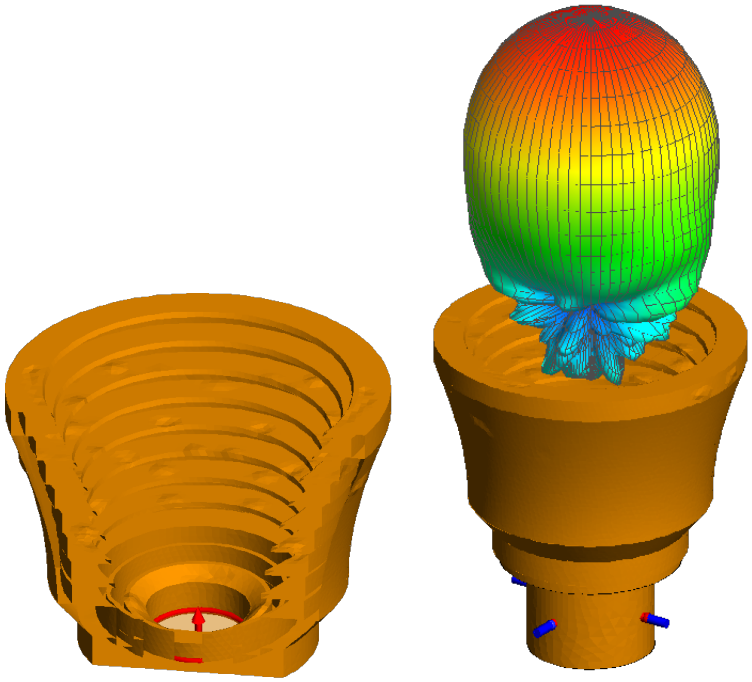

(a) (b)

Figure 4.15: (a): Cutplane view of VeGA with an exemplary surface roughness created by a 3D-printer. (b): Radiation pattern for the assumed surface roughness VeGA with OMT.

Figure 4.16 shows the simulations of antenna model with manufacturing imperfections. It can be observed from the Cartesian plot 4.16 that the gain for antenna model with imperfections and without imperfections is nearly same. Meanwhile the cross-polarization pattern for the deformed VeGA in the relevant range is not as similar as the undeformed VeGA, but the obtained cross-polar isolation of the deformed VeGA is better than 35 dB satisfying the design requirements illustrated in Tab. 1.1. After observing the simulation results 4.16, it can be concluded that manufacturing imperfections has no major influence on the radiation properties of P-band antenna and in case if some imperfections are observed it can be accepted.

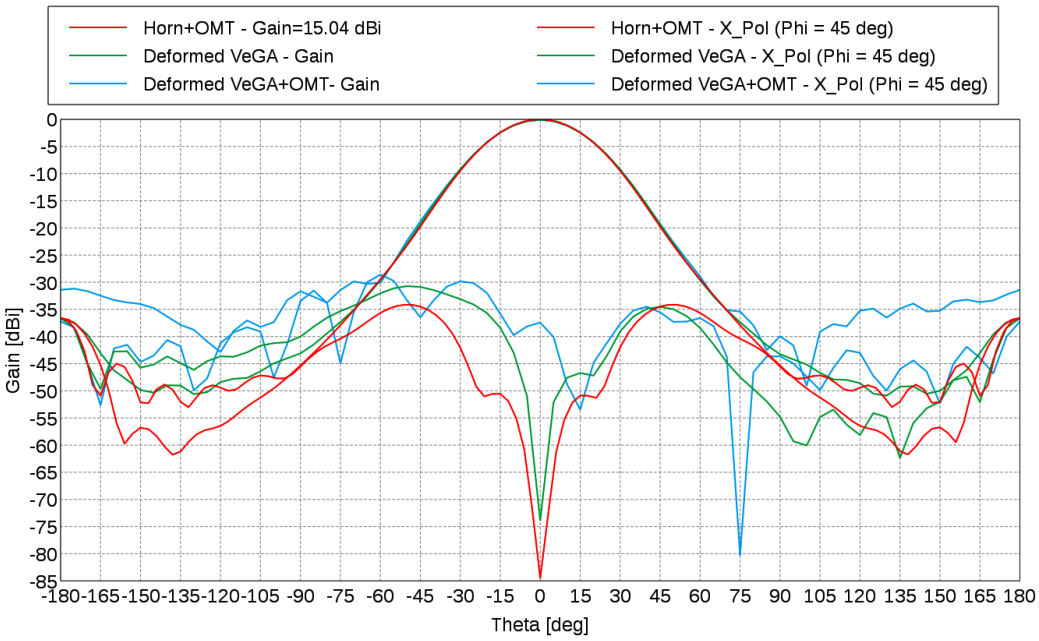

Figure 4.16: Total gain and cross-polar component for the deformed and undeformed combination of OMT and horn. One can observe that for the analyzed level of deformation, the cross-polarization performance is slightly reduced so that the antenna requirements from Tab. 1.1 are violated.

To summarize the entire Chapter 4 into a short paragraph, the followings contributions are made: Initially one of the main task is to adapt the existing antenna model concepts presented in [1], [2] to P-band. Moreover the developed antenna model (combination of VeGA and OMT) must satisfy the design requirements listed in Tab. 1.1. In regard to that, a P-band antenna model is developed by performing necessary optimizations required to the model and later on the model performance is evaluated through simulations. The simulations validated the developed model by satisfying the design requirements listed in Tab. 1.1. The modeling of a perfect electric conductor (PEC) P-band antenna model and simulations are performed using numerical simulation tool.

Chapter 5

Conductive Coating for Plastic Antenna: Simulations and Experiments

The developed P-band antenna presented in section 4.1, 4.3, 4.4 were modeled and simulated in EM simulation tool considering the model as a perfect electric conductor. But the main motive is to 3-D print the developed P-band model using outdoor thermoplastic material. Before 3D printing in plastic, it is important to examine the influence of plastic material and conductive paint on radiation properties of antenna model. So considering this, a new simulation method was proposed in the thesis. In this new simulation method, inspite of modeling the antenna as a perfect electric conductor, the thermoplastic material and conductive paint are used in modeling the VeGA and OMT in FEKO [47] to examine the antenna performance behaviour.

5.1 Antenna Modeling in Plastic and Conductive Paint

The antenna model was modeled and simulated in numerical simulation tool FEKO [47]. The ASA plastic was modeled with a permittivity of $\varepsilon_r = 1.9$ and a loss tangent of $\delta = 0.04$. The obtained permittivity and loss tangent values shown in Figure 5.1b were measured using waveguide based method.

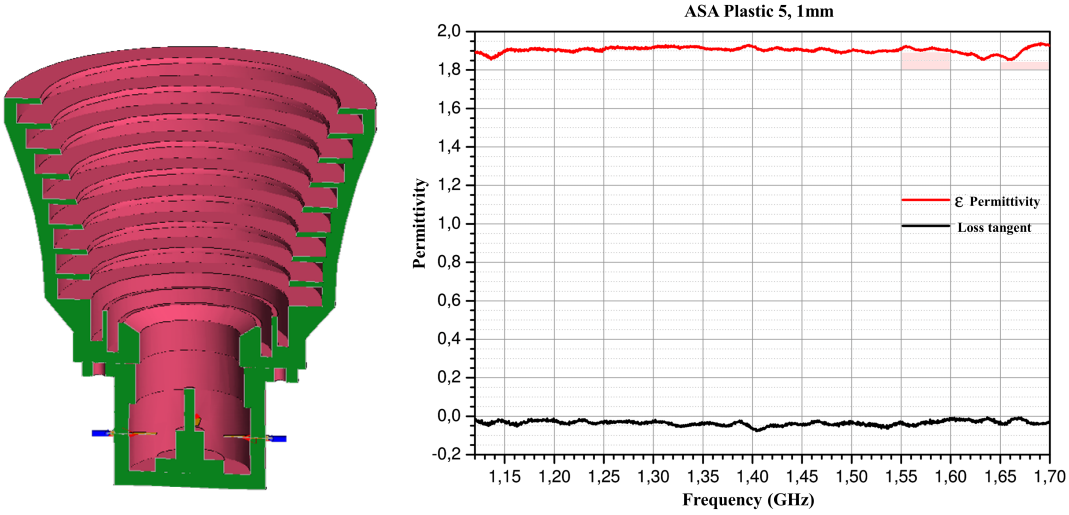

(a) (b)

Figure 5.1: (a): Cutplane view of antenna model adapted to plastic (Green) and coated with conductive paint (Pink). (b): Measured real and imaginary parts of the dielectric constant of ASA plastic. The dielectric constant of ASA plastic material is measured at L-band using waveguide based method.

In section 3.3, it was mentioned that to make plastic behave as an antenna element, either nickel or carbon paint has to be used as a coating. The main challenge for numerical simulation after the antenna modeling in plastic was the coating modeling. To model the plastic antenna with paint, its conductivity and thickness are necessary where these values play a crucial role in determining the required skin depth at any frequency. However the conductivity for a specified thickness of the paint would be either provided by the manufacturer or it can be known by measuring with suitable instruments. The conductivity and thickness values are used within FEKO for simulation. Based on the antenna performance for nickel and carbon coatings, it would be easy to select an appropriate coating as a final product. Therefore behavior of nickel and carbon coatings on antenna performance is explained below:

Nickel conductive paint. For nickel conducive paint a predefined conductivity and thickness provided by the manufacturer are used within numerical simulation tool for simulation. From the data sheet [45], a 3.0 mil (76.2 µm) coating of Super Shield 841 having relative permeability ≥ 100 results in a conductivity value of 52.5 kS/m resulting in a skindepth of 10.5 µm. This means that to acheive gain of 15 dBi and cross-polarization of 35 dB in the relavant range, the antenna has to be coated with a thickness greater than the required skin depth 10.5 µm. Based of the predefined values in [45], the antenna model was simulated with different thickness and conductivity values. The simulated radiation patterns are shown in Figure 5.2 for both gain and cross polarization. From the simulation results in Figure 5.2, it is clear that for the coating thickness less than the required skin depth

(10.5 µm), the gain and cross-polar isolation were reduced violating the design requirements shown in Tab. 1.1. For example, for conductive coating thickness of 2 µm (which is less than the required skin depth), the gain has been reduced by 0.5 dBi, cross-polar isolation has been reduced from 35 dB down to 30 dB in the relevant range and also side lobes can be observed. However, the design requirements from 1.1 were satisfied for a coating thickness greater than the skin depth.

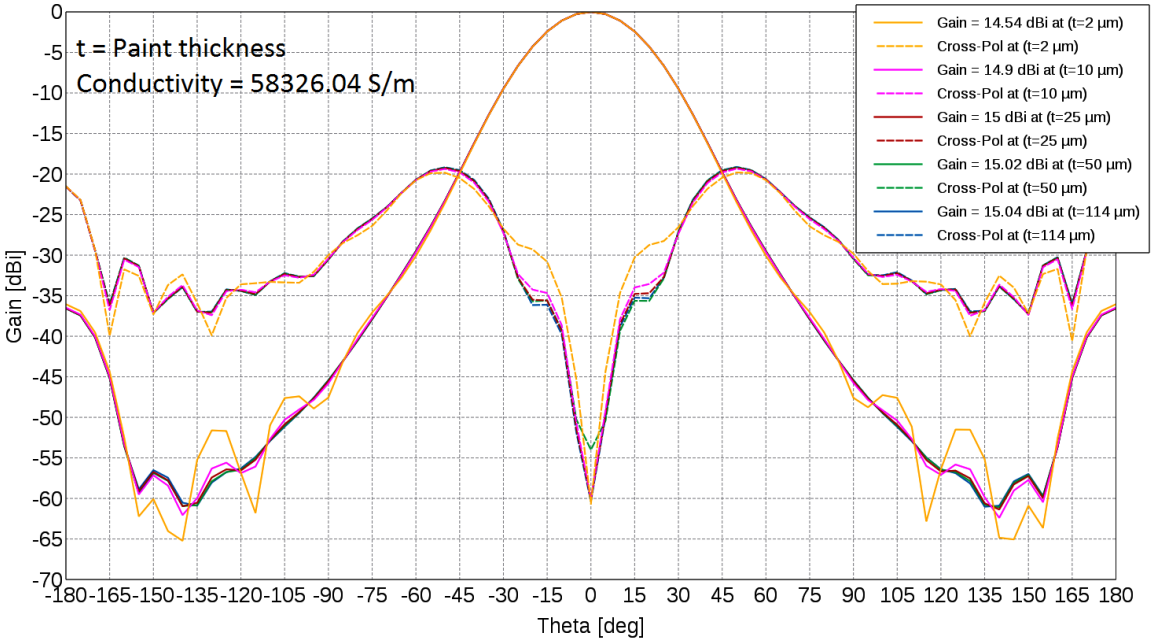

Figure 5.2: Total gain and cross-polar component (X-Pol) for the OMT and horn as function of viewing angle θ. The required skin depth of the nickel paint at P-band is calculated to be 10.5 µm. From the simulated antenna model, one can observe with a nickel paint thickness of 114 µm, the gain and cross-polarization (blue curve) performance satisfy the antenna requirements from Tab. 1.1. But for the paint thickness less than the skin effect (10.5 µm), a large change in the gain and cross-polarization is not observed.

The simulations shown in Figure 5.2 illustrates that the nickel conductive paint is conductive enough at P-band. Also the analyzation of the change in gain and cross-polarization for a coating thickness less than required skin depth shows that the method used for modeling the conductivity and thickness in numerical simulation tool for simulations is correct. But due to the restricted availability of nickel conductive paint, it was decided to use the readily available HSF44 carbon conductive paint as a top coat for the antenna model. Unlike nickel conductive coating, the conductivity and thickness of carbon conductive coating were not published by the manufacturer.

5.2 Experiments to Determine Conductivity and Thickness of HSF44

The carbon conductive paint HSF44 from YShield GmbH [46] is mostly used on the interior and exterior walls for protection against electromagnetic waves. As the HSF44 paint is mainly used for housing applications the knowledge of shielding attenuation is necessary and even the manufacturer has provided only the shielding attenuation values at different frequencies. Till the present day, to the best of the author's knowledge nobody has tried to use the technical coating HSF44 carbon conductive paint from YShield [46] on plastic antenna applications and thereby no one has an interest to know the conductivity and thickness of the paint for a single coat. Even though performance analyses on the paint were performed [41], the paint conductivity and thickness were not known. As it was thought of using readily available HSF44 carbon conductive paint, the necessity to determine the minimum thickness required to be coated on P-band plastic antenna model is very important. So the main challenge lies in finding the process for determining the paint conductivity, thickness and also the adhesive strength between the HSF44 paint [46] and ASA plastic material.

To evaluate the process for determining the paint conductivity, thickness and adhesive strength, ASA plastic material and technical coating HSF44 were ordered.

5.3 Experiments with ASA Plastic and HSF44 Conductive Paint

Rectangular samples made from the same ASA material as planned for the printing of the 3-D antenna were manually painted with HSF44 conductivite paint using a roller and can be seen in Figure 5.3. As the samples were painted manually, a uniform thickness is not maintained and the surface is inhomogenous. The dry time of the paint on plastic takes almost 7 days. After coating the plastic with carbon conductive coating it was observed that the paint is not scratch resistant that means when the coated plastic is scratched with fingers or rubbed with a piece of paper then a black color can be observed on your fingers or paper as shown in Figure 5.3b. The reason for the paint being not scratch resistant is due to graphite nature of paint. To protect the HSF44 carbon conductive paint, a topcoat, prescribed by the manufacturer [46] must be used. The next important step is a way to determine the paint adhesive strength, conductivity and thickness, which is explained in the following paragraphs.

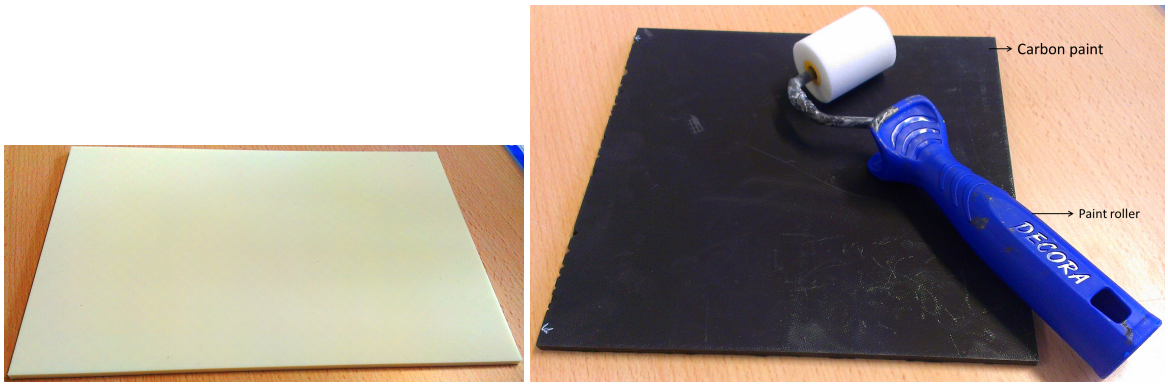

(a) (b)

Figure 5.3: (a): Rectangular shaped ASA plastic material (left). (b): ASA plastic coated with carbon paint using a paint roller (right).

5.4 Adhesion Testing Method of Paint on Plastic

Adhesion testing of the paint is necessary to ensure the paint will adhere properly to the plastic or any metal to which they are applied. Adhesion testing after coating process will quantify the strength of the bond between the plastic and the coating. Such kind of testing is important because most of the paints does not adhere well with plastics and moreover to the best of author's knowledge till present day nobody has tried to coat the carbon conductive paint HSF44 on ASA plastic material. So as a first step in studying the behavior of carbon paint on ASA plastic, it is necessity to determine the adhesive strength of carbon paint on ASA plastic.

To determine the adhesion strength between HSF44 carbon paint and ASA plastic material, two samples, single and double coated having dimension 5 cm × 5 cm and 7 cm × 7 cm as shown in Figure 5.4 were sent to a measurement laboratory [50]. According to the standard ASTM D3359, the adhesive strength between paint and plastic were performed by means of a series of cuts through coating called as cross cut adhesion test method. The procedure and information about the cross cut test adhesion method can be found in [51]. After the test it was determined that 5 to 15 % of the paint got removed which is mainly due to manually coating.

5.5 Thickness Measurement

Thickness measurements are important because in order to determine the conductivity of a paint, thickness of the paint play a crucial role. Incorrect coating thickness for P-band antenna model may lead to skin effect problems or excessive costs. These measurements can be completed with thickness measurement tools like ellipsometer or stylus profilometer.

Unfortunately, such a device was not available and more over these devices are mostly used in semiconductor field and measures the samples in nanometers. But for a conductive paint coated corrugated horn antenna, a user friendly and handheld instrument would be a better choice in determining thickness of the paint. After a through investigation, it was found that a handheld device called as Positector 200 would be the suitable instrument to measure the conductive coating thickness and is shown in Figure 5.4c. The advantage of this device is that it uses a probe to measure the thickness and for corrugated horn antennas it would be the best instrument. Positector 200 measures conductive coating thickness over wood, concrete, plastics and composites using proven ultrasound/ultrasonic technology.

Ultrasonic Principle. The probe of the instrument (Positector 200) contains an ultrasonic transducer that sends a pulse through the coating via a coupling gel. As soon as the pulse reaches the substate, the pulse get reflected back to the transducer and is converted into a high frequency electrical signal [50]. The reflected pulse is digitized and analyzed to determine coating thickness.

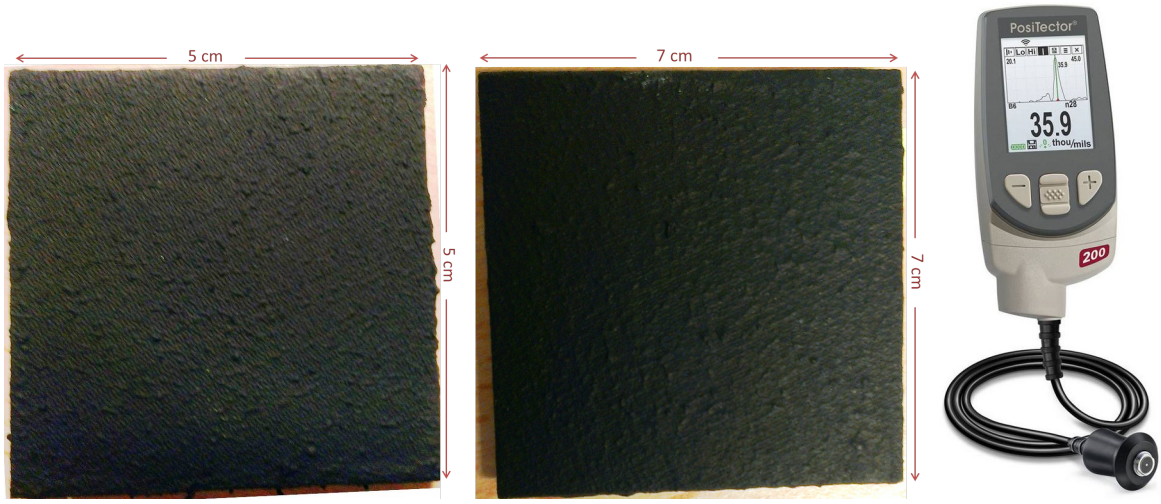

(a) (b) (c)

Figure 5.4: (a): Single coated 5 cm × 5 cm sample with HSF44 (b): Double coated 7 cm × 7 cm sample with HSF44 (c): Thickness measurement gauge. These two samples were sent to the measurement laboratory to measure the thickness of the conductive paint [50]. The device used to measure the thickness is Positector 200.

To measure the thickness of the carbon conductive paint HSF44 manually coated on ASA plastic, the samples as shown in Figure 5.4a 5.4b were sent to a measurement laboratory. A repetitive measurements were performed using two different probes to maintain reproducibility. The final outcome from the laboratory was that in principle the measurement of samples were possible but due to dissolving of the paint with coupling gel (used between probe and sample) and kind of coating the results were not reproducible. There

were too many misleading signals although the measurements were performed with two different probes which showed significant differences in the measurement results. Therefore it was not recommended to use the gauge Positector 200 in measuring the thickness of carbon conductive paint HSF44 [46]. To sum up, accurate thickness values for carbon paint HSF44 was not possible and not known.

5.6 Conductivity Measurement

The most basic measurement technique for the surface resistivity measurement is the four point probe method [32] which is a contact type method. Due to the non-availability of the four point probe measurement setup and also not sure about the performance of the instrument on non uniform coating thickness, some of the samples with dimensions 10 cm ×10 cm were sent to a measurement laboratory. The measurement results for a single coated sample were presented in Table 5.1 and the instrument performed the surface resistivity measurement at different locations on sample is shown in Figures 5.5a, 5.5c. The instrument used for surface resistance measurement is called as Duores from Napson corporation, Japan [52] is a hand held instrument and has a possibility to use two kinds of measurement probes non-destructive probe and four point probe. Initially the surface resistivity measurements were performed on two samples using four point probe method (contact type) and later on with non-destructive probe method (non-contact type).

The parameters presented in Table 5.1, Run 1, Run 2 and Run 3 are the measurements performed at a single location and $'CV'$ is the reproducibility of three runs at a single point. The values presented in Tables 5.1, 5.2, 5.3 are surface resistivity values in$(\Omega/square)$. From the Table 5.1, it is clear that for a single coat of HSF44 carbon conductive paint, the measured surface resistivity value is around 7.78$(\Omega/square)$. The little different data at every run are caused by the manual touch, non-uniform thickness of the coating and the different measurement areas of the probe. Even though the measurement results from contact type four point probe method is convincing, as a cross check it was thought to perform the sheet resistivity measurement with non-destructive probe method shown in Figure 5.5a (right). The non-destructive probe method is based on eddy current principle.

Eddy Current Principle. Eddy current method is used mainly in case of non-contact type surface resistivity measurement. An alternating magnetic field at the surface of the instrument's probe is generated when an alternating current is applied to the induction coil. When the probe is placed near the conductive specimen, eddy currents are generated on the surface of specimen due to alternating magnetic field. Due to the characteristics of the specimen and coating thickness, eddy currents within the specimen generates an opposing magnetic field to the primary field and is sensed by the exciting coil.

(a)

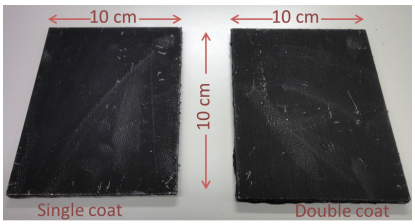

(b)

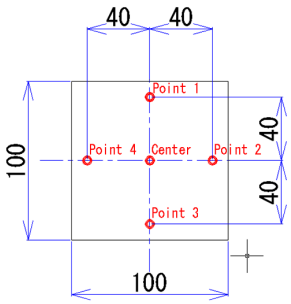

(c)

Figure 5.5: (a): Hand held sheet resistance measurement instrument (adapted from [52]). This instrument has an advantage to measure sheet resistance of conductive coating using either four point probe (left) or non contact (non destructive) probe based on eddy current principle (right). (b): Experiments conducted on single and double coated samples to measure sheet resistance (c): Sheet resistance measured at different positions on the sample.

Measured point	Center	Point 1	Point 2	Point 3	Point 4
Run 1	8.341	6,915	5,921	8,412	8,916
Run 2	8,356	7,185	5,787	8,489	8,627
Run 3	8,322	7,134	5,800	8,563	8,629
MAX	8,356	7,185	5,921	8,563	8,916
AVE	8,340	7,078	5,836	8,488	8,724
CV	0,17%	1,65%	1,03%	0,73%	1,56%

Table 5.1: Four point sheet resistance measurement performed by Duores instrument on a single coated sample. The measured values are in ($\Omega/square$).

Based on the eddy current principle the Duores instrument using non-destructive probe shown in Figure 5.5a, measured the sheet resistivity of samples shown in Figure 5.5b and the measured results are presented for single and double coated samples in Table 5.2, 5.3. The non-contact type surface resistivity measurement for a single coated sample has an overall value of around 7.9 ($\Omega/square$) and even the reproducibility values for different

runs are nearly same. When comparing the measured surface resistivity values of both probes for a single coated sample, the maximum surface resistivity value is nearly equal. It has to be also noted that the surface resistivity is not constant all through the sample because of the manually coating process. In case if some technical coating process is involved like electrolytic or electroless instead of manually coating, it is believed that a uniform thickness can be maintained, conductivity of carbon paint HSF44 can be increased and moreover the surface resistivity would be constant throughout the sample. For a single coated sample, deriving conductivity from the obtained surface resistivity value and estimating a thickness of 36.2 µm, it was observed that the carbon paint has a conductivity in terms of 10^4 (S/m).

Measured point	Center	Point 1	Point 2	Point 3	Point 4
Run 1	7,724	7,055	5,572	9,734	8,926
Run 2	7,795	7,212	5,427	9,569	9,167
Run 3	7,758	7,027	5,612	9,593	9,063
MAX	7,795	7,212	5,612	9,734	9,167
AVE	7,759	7,098	5,537	9,632	9,052
CV	0,37%	1,15%	1,44%	0,76%	1,09%

Table 5.2: Non-contact sheet resistance measurement performed by Duores instrument on a single coated sample. The measured values are in $(\Omega/square)$.

Tab. 5.3 represents the surface resistivity measurements for a double coated sample. It can be realized from the obtained measurement that, the double coated sample has an overall surface resistivity of around 2.2 $(\Omega/square)$ and even the reproducibility of the measurements is 0.6% . Meanwhile estimating a thickness of 76.2 µm for double coated sample, conductivity of 5914.09 (S/m) is derived. A lot of cross check has been done by sending samples to different companies in verfying the conductivity of carbon paint HSF44. In this cross check process some of the samples were measured by SURAGUS non-contact sheet resistance mapping system EddyCus TF map 2525SR [53] which is based on eddy current principle. This instrument scans the entire sample and then gives an average sheet resistance value unlike Duores instrument from Napson corporation. The scanned sample and its measurements can be seen in Figure 5.6. The surface resistance measurements of a double coated sample from different laboratories and with different instruments are almost similar which encourages to use either of the instrument for measuring the surface resistance of a P-band antenna model. But the main disadvantage of the instrument EddyCus TF map 2525SR is that it is not compatible for measuring the surface resistance of Gaussian corrugated P-band antenna model. Because the dimension of the instrument is large than the slot depth and slot width of P-band corrugated antenna.

Measured point	Center	Point 1	Point 2	Point 3	Point 4
Run 1	2,197	1,830	2,642	2,517	1,849
Run 2	2,126	1,832	2,682	2,526	1,858
Run 3	2,195	1,821	2,668	2,520	1,840
MAX	2,197	1,832	2,682	2,526	1,858
AVE	2,173	1,828	2,664	2,521	1,849
CV	1,52%	0,26%	0,62%	0,15%	0,40%

Table 5.3: Non-contact type measurement on a double coat sample. The measured values presented are in ($\Omega/square$).

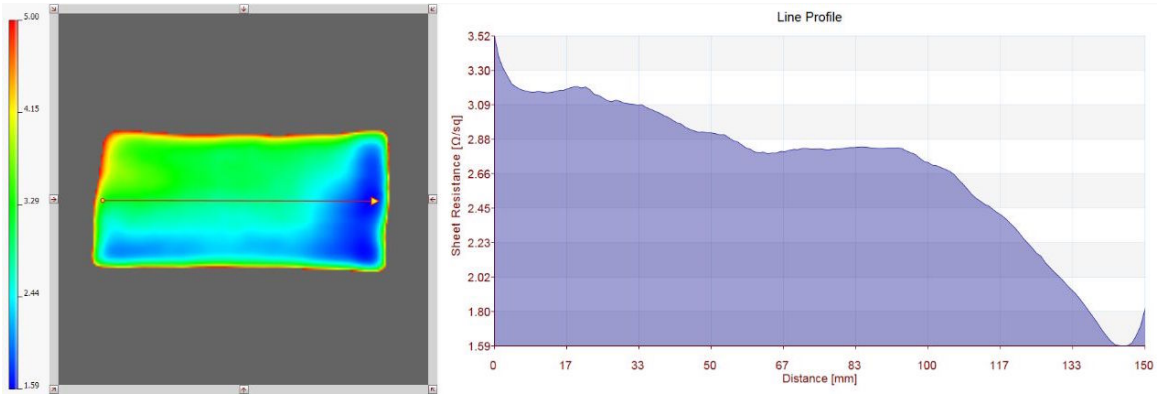

Figure 5.6: Non-contact measurements on a double coated sample. Measurements presented are performed with non-contact sheet resistance EddyCus TF device. The left plot presents the scanning procedure performed by the measurement device on the sample to obtain the sheet resistance and the right plot present the numerical values obtained from scanned sample. The average sheet resistance obtained for a double coated sample was around 2.6 ($\Omega/square$).

5.7 EM Simulations of Carbon Coated Antenna Model

Based on the measured surface resistance value (conductivity in terms of 10^4 S/m) and estimating rough thickness value, P-band antenna was modeled in FEKO suite 7.0 [47]. It has to be noted that irrespective of the coating thickness and with the measured conductivity of double coated sample, the P-band antenna model modeled using carbon paint HSF44 in electromagnetic software has a skin depth of around 300 µm. To make P-band antenna model as an antenna element using carbon conductive coating HSF44, the antenna has to be coated with a paint thickness greater than 300 µm. To verify the behaviour of carbon conductive paint HSF44 on antenna performance, the P-band antenna model was simulated in a numerical simulation tool [47] with varying coating thickness and the simulations are shown in Figure 5.7. From the simulations shown in Figure 5.7, it can be observed that only for a coating thickness of 2 µm the gain is reduced about 2.7 dBi from the required 15.04 dBi and the cross-polar isolation has been reduced from the required 35 dB down to 25 dB. It is also unclear from the numerical simulations 5.7 that the performance of the antenna is not as dramatically affected when the antenna is modeled with

a coating thickness of 100 µm which is 3 times less than the required skin depth. This is realized when the gain and cross-polar isolation of the antenna modeled with a coating thickness of 100 µm is only reduced by 0.1 dB from the considered design requirements illustrated in Tab. 1.1.

The difference between nickel conductive coating 841 [45] and carbon conductive coating HSF44 [46] in terms of conductivity is that carbon coating conductivity is lower than that of nickel and for a single coated sample, carbon can achieve the conductivity of nickel only when the coated thickness of the carbon is thrice than the coated thickness of nickel. But anyway the simulations and measurements performed with carbon conductive paint coated on ASA plastic prove that HSF44 can be easily used and furthermore satisfying conductivity requirements at P-band.

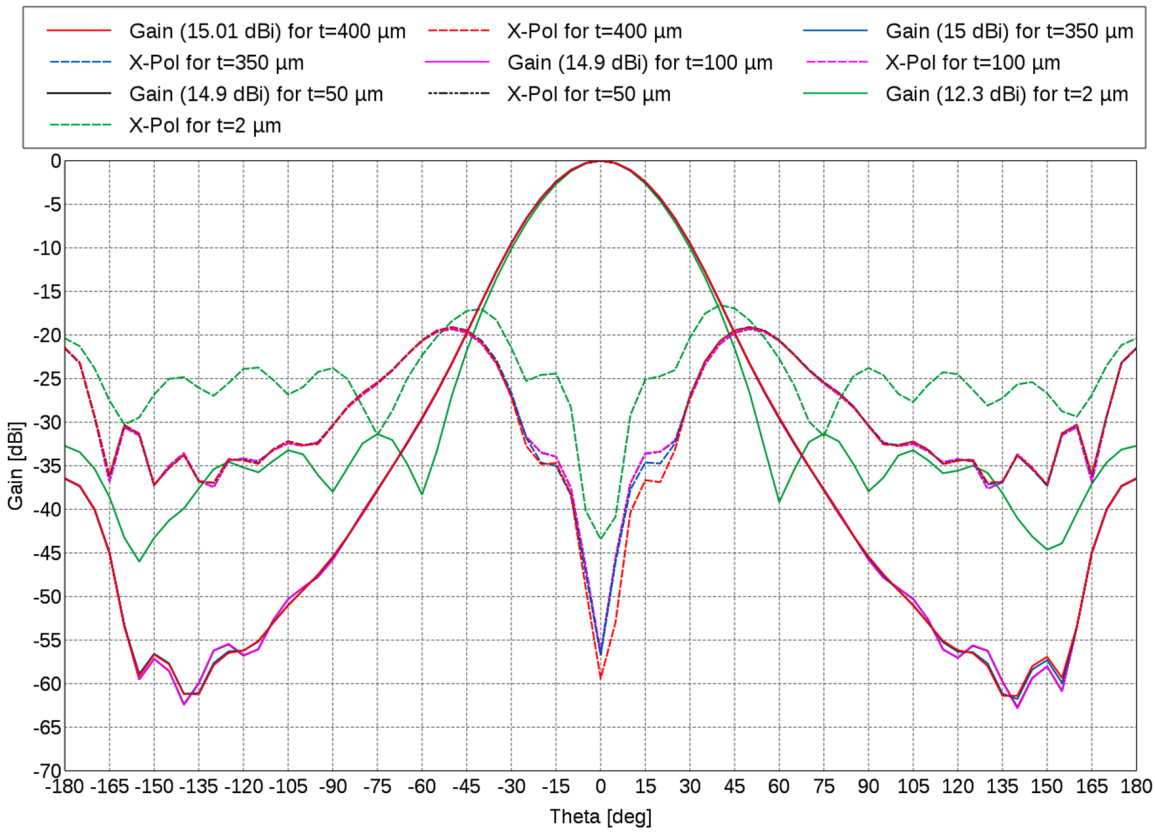

Figure 5.7: Total gain and cross-polar component (X-Pol) for the OMT and horn as function of viewing angle θ for the antenna model modeled with carbon conductive paint HSF44. The skin effect of the carbon paint at P-band is calculated to be 300 µm. From the simulated antenna model with a carbon paint thickness of 350 µm, the gain and cross-polarization (blue curve) performance satisfy the antenna requirements from Tab. 1.1, whereas for a paint thickness less than the skin effect (green and pink curve), the antenna requirements from Tab. 1.1 are violated. In the Figure, t refers to coating thickness.

5.8 Manufacturing Tolerance Analysis

To manufacture or fabricate a device or any model, a manufacturing tolerance value of the model has to be specified for the manufacturer. The performance of the model mostly depends on the manufacturing precision. Coming to the Gaussian corrugated horn antenna some authors [54], [55] claim that low frequency choked horn antenna is less sensitive to manufacturing tolerances. But it would be better and important to have a manufacturing tolerance value of any antenna model. As the P-band antenna model is 3-D printed using additive manufacturing technique a systematic error from the machine is considered instead of random error for the corrugations in VeGA. As it is evident that corrugations in the VeGA are sensitive to radiation properties, it is necessary to specify the manufacturing precision of the corrugations. The study of manufacturing tolerance of P-band antenna model was carried out in electromagnetic simulation software. A random number generator is created and added to the sensitive parameters of VeGA and several simulations have been performed with parameterized random values. The aim of the process is to identify the most critical parameter value in order to specify to the manufacturer. Three important parameters namely $slot\ width$, $ridge\ width$ and $slot\ depth$ of the horn antenna are mainly evaluated to find the manufacturing tolerance of VeGA. The analysis results obtained from numerical simulation tool are expressed in terms of gain and cross-polarization as a function of viewing angle θ.

The evaluation has been done step by step and after a long simulation run it was observed that slot depth of the corrugations did not show much influence on the antenna radiation pattern. But the randomized ridge width and slot width of Gaussian and throat section of VeGA showed an influence on theoretical profile of VeGA and radiation pattern. From the obtained simulations of random ridge and slot width parameters, a normal distribution is considered to efficiently evaluate a critical tolerance value and parameters under analysis are presented in histograms shown in Figures 5.8, 5.9. Figure 5.8 represents the approximate distribution of input parameters whereas Figure 5.9 shows the resultant variation of gain and cross-polarization due to parameterized random values of the input parameters. These histograms reveals that the variation in the dimensions of the horn like slot width, ridge width and slot depth, alters the performance of horn in terms of gain and cross-polarization.

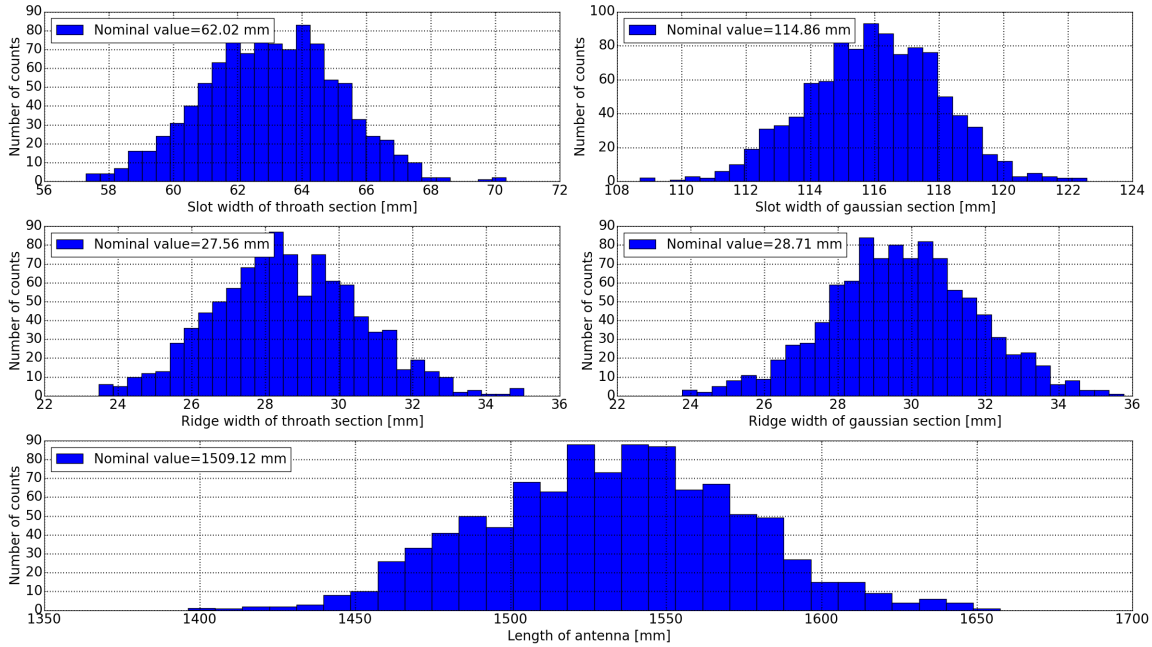

Figure 5.8: Approximate distribution of input parameters for FEKO simulation runs. Histograms 1-4 are the random input values and plot-5 is the variation in length of antenna due to random input values.

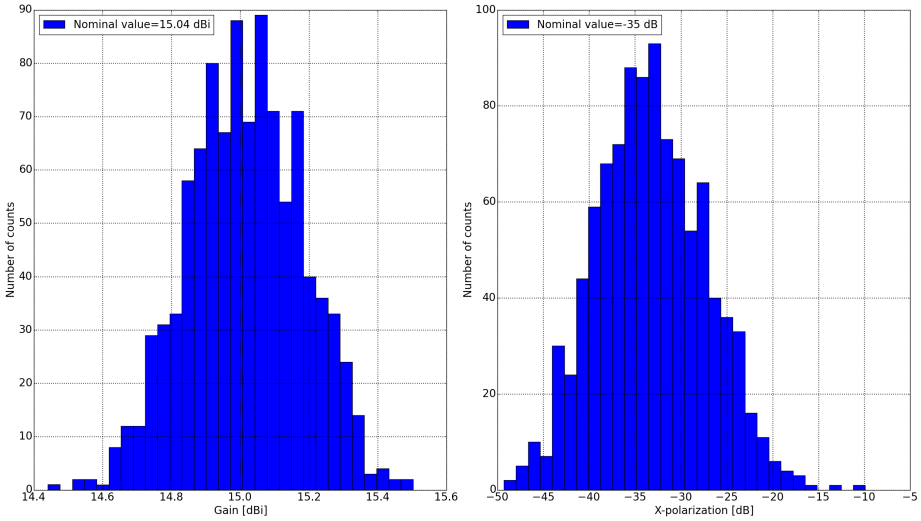

Figure 5.9: Histograms of the resultant gain and cross-polarization from the parameterized random input values.

The tolerance value is determined when a sudden change in the Gaussian shape of the radiation pattern, change in gain value from the desired 15.04 dBi and variation of the cross-polar level from the desired cross-polar isolation requirement greater than 35 dB is observed. After a careful tolerance study from the histograms shown in Figures 5.8 5.9 and simulations of P-band antenna model, a tolerance of $\pm$0.511 mm or $\pm$0.000742 λ_c, where λ_c is the wavelength at the center frequency was found not to significantly alter the radiation pattern of P-band antenna model. As a conclusion, the accurate performance of

the corrugated antenna not only depends on the design or antenna model but also depends much on the ability to precisely manufacture the corrugations.

Tolerances During Assembling. As it is known that to 3-D print the P-band antenna model using additive manufacturing technique, the antenna model has to be sliced into smaller segments due to limited printing volume of typical printers. During de-assembling and assembling of the antenna model, there may be a chance of misalignment between the segments when screwed together. Taking this into account is a necessity to study the tolerance analysis of lateral misalignment between the segments. Considering such kind of assembling precision, the P-band antenna model was modeled in numerical simulation tool in such a way that the antenna was sliced into 4 segments instead of 8 segments due to difficulty in modeling and long simulation run time. The misaligned antenna model is shown in Figure 5.10. In numerical field simulations, such misaligned antenna model is simulated by setting the segments to be offset by 0-10 mm in steps of 0.1 mm.

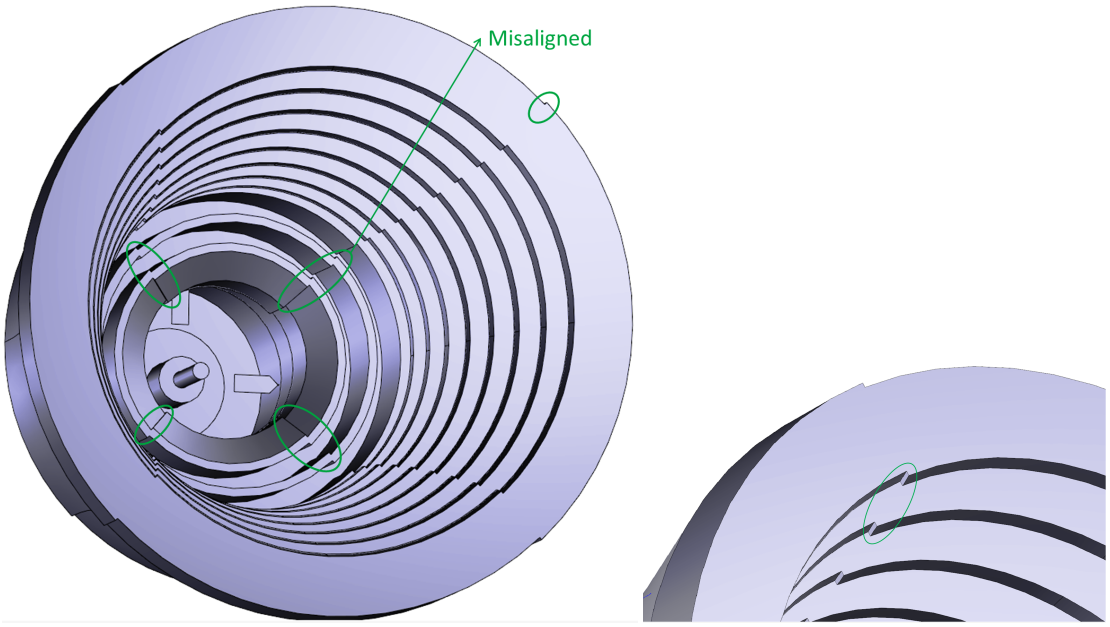

(a) (b)

Figure 5.10: (a): Misaligned VeGA and OMT. (b): Half part of VeGA. The green labels shows the number of mis-alignments created at different locations of VeGA.

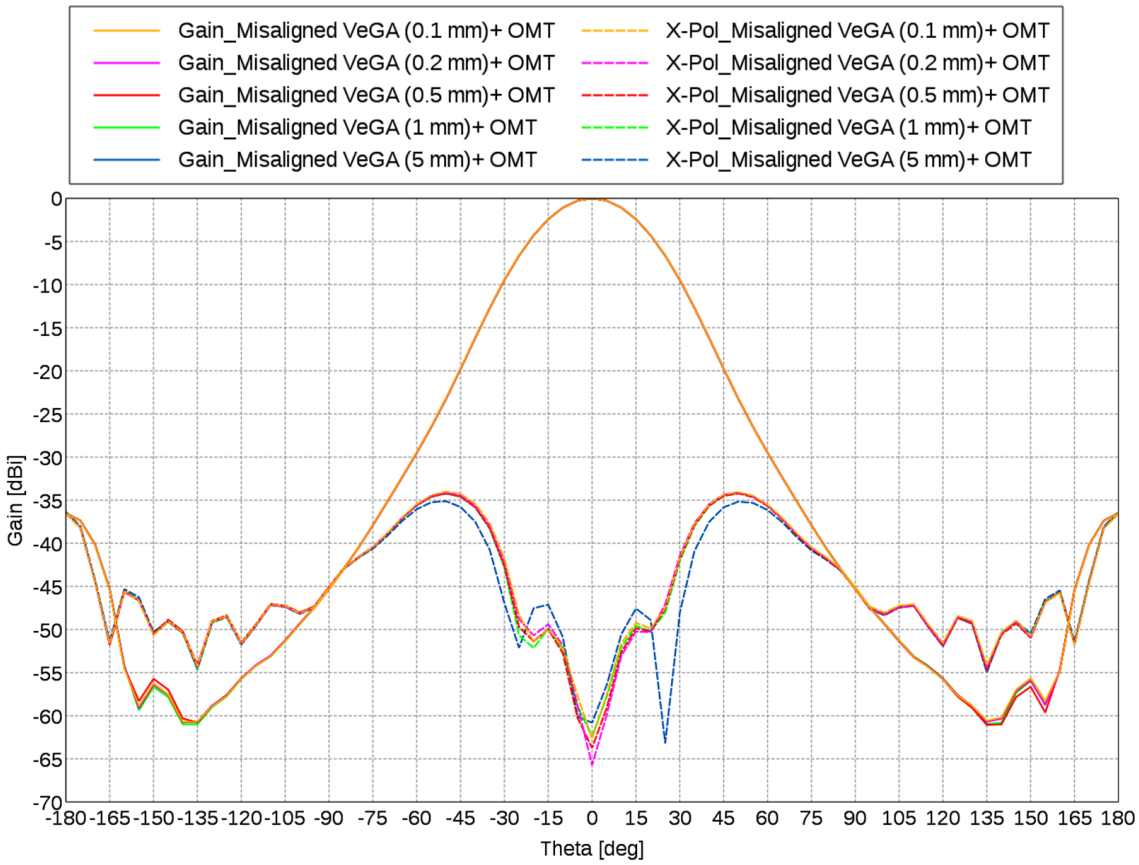

Figure 5.11: Total gain and cross-polar component (X-Pol) for the OMT and misaligned horn as function of viewing angle θ. For different offset mis-alignment values, only a few offset values which show an influence on gain and cross-polar level were plotted.

After performing the numerical simulations for different settings (in steps of 0.05 mm) of segments, the gain of the misaligned antennas remains at 15.04 dBi whereas, the cross-polar isolation is greater than 46 dB, which is essentially better than the required 35 dB. This shows that even if there is an offset between the segments of about $\pm$ 5 mm, the performance of the antenna is not effected, still satisfying some of the design requirements illustrated in Tab. 1.1. Moreover due to the complexity involved in numerical simulations, in setting the segments to be offset greater than 10 mm, a specific tolerance value which has to be maintained during assembling the antenna is further not provided.

5.9 Conclusions

To sum up, the following contributions are made in this Chapter 5:

- Firstly, in section 5.1, a challenge to adapt the antenna modeling in numerical simulation tool to plastic and conductive coating modeling is introduced. In order to perform EM simulations for such kind of antenna model in plastic, some of the material

properties like required coating thickness, conductivity of the paint and permittivity of the plastic were not available. Thus, the missing material properties required for EM simulations could be obtained by ordering the desired paint and plastic and then conducting experiments on them.

- In the following section 5.2, the necessary experiments are conducted to achieve the conductivity, thickness of paint and also the permittivity of the plastic. The required experiments in obtaining the material properties made me to go through and introduce different measurement tools. Later on the data from the measurement tools are analyzed which helped in determining the conductivity of the conductive paint and permittivity of the plastic material.

- In section 5.7, the obtained experimental material properties were implemented into FEKO for numerical simulations. From the obtained simulations of the antenna model adapted to plastic and conductive paint, a comparison is made with PEC modeled antenna which proved that the gain and cross-polarization requirements of both models are in good agreement.

- Finally, in section 5.8, a manufacturing tolerance value is determined by performing approximate distribution analysis, to ensure a tight manufacturing tolerance value is maintained while 3-D printing the antenna. As the gain and cross-polar level depends on the corrugations of the antenna, a determination of tolerance value ensure to have a high performance antenna where the measurement results would be similar to the results obtained during simulations.

Due to the promising results achieved from the simulations of antenna model adapted to plastic and conductive paint, it is thought of 3-D printing the antenna model. The processing for 3-D printing is explained in the next Chapter 6.

Chapter 6

Manufacturing of Light Weight Outdoor L-band Horn Antenna

6.1 CAD Design of L-band Antenna

To go from an antenna model shown in Figure 6.1a suitable for numerical simulations to an actually 3-D printed object, several mechanical refinements need to be included in the design. The necessary adjustments to the structure is made using a computer-aided design (CAD) software. It is important, as the large sized P-band antenna having dimensions 2.2 m × 2.16 m × 2.16 m is not compatible with the existing fused deposition modeling 3-D printers available in the market. The antenna has to be cut into several segments according to the build volume of the printer and later the segments can be joined together with screws to form a single antenna. Also other adjustments need to be considered: a minimum wall thickness (strong enough to sustain winds, cracking), the antenna should be water tight and necessary outlets must be made in order to let the moisture out of antenna. Considering these necessary adjustments, the mechanical design was supplemented with necessary joints using the CAD software. These supplements based on CAD and the manufacturing by means of a 3-D printer was executed by "Systemhaus Technik", a further Institute of DLR (DLR-SHT).

The CAD model of the complete antenna and a single segment with water outlets is shown in Figures 6.1b, 6.1c. The P-band antenna prototype was cut into 32 segments according to the build volume of Fortus 900mc FDM based 3-D printing machine, which is the largest FDM based ASA plastic compatible 3-D printing machine with a build size 914 mm × 610 mm × 914 mm available till date. In the following, the mechanical design and production process of a P-band antenna is described. For time and cost constraints, the antenna was finally built scaled down for L-band (1.2575 GHz) though, and the corresponding verification measurements are described in the following Chapter 7.

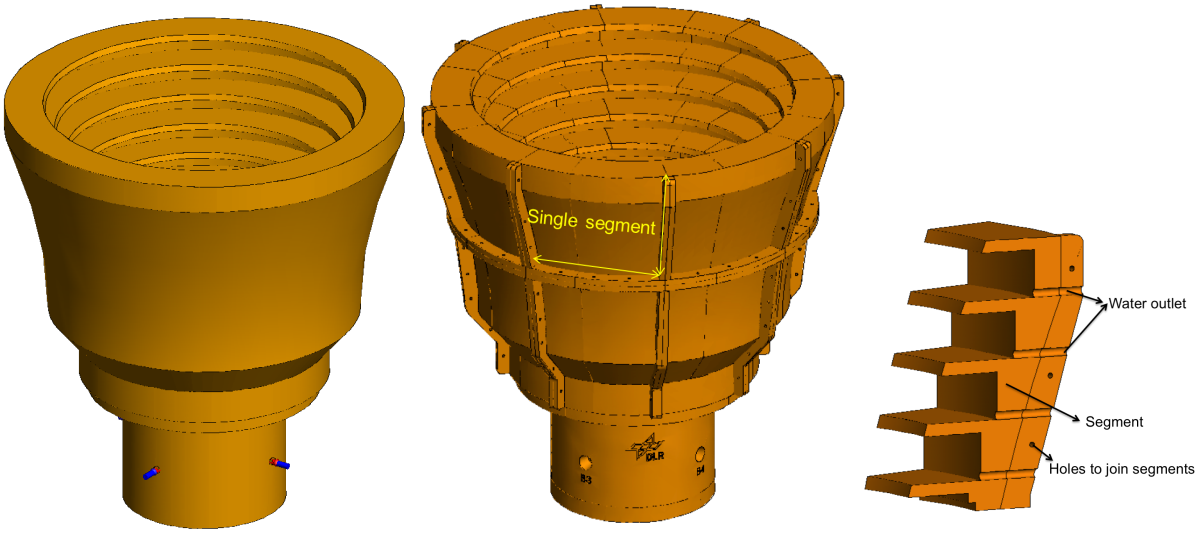

(a) (b) (c)

Figure 6.1: (a): The antenna model used in FEKO for performing simulations. (b): CAD modified antenna model prior to printing. Some necessary adjustments are made on the outer surface of the antenna model (not effecting the performance of the antenna) to achieve the necessary mechanical stability and to withstand wind loads. (c): A single segment, highlighting (rain) water outlets. To print the antenna model with FDM based 3D printer, the antenna has to be sliced into several small segments.

This chapter provides detailed description of the 3-D printing process concerning the antenna.

6.2 Weight, Durability, Transportability and Cost

After implementing necessary adjustments for the ASA plastic P-band antenna structure in CATIA software with the help of DLR-SHT, the total weight was estimated to be around 600 kg having a wall thickness of 6.8 cm and each segment weighs around 30 kg which could be easily transported by two persons. Here the walls of the antenna are considered to be filled with honeycomb structures rather than completely solid material. The honeycomb structures seems to appear like beehives where their cells are columnar and hexagonal in shape. The main reason for using honeycomb structure in 3-D printing the antenna is to minimize the weight of the antenna and also to reduce the material and material cost in 3-D printing the antenna. In case if the antenna is 3-D printed in a solid block of plastic then the weight would be more than 1500 kg which would be the one of the reason for violating the design requirements. It was also assumed that with a wall thickness of 6.8 cm, the antenna would be strong enough to sustain environmental effects and believing that the antenna can be deployed in outdoor for a period of 10 years.

Due to unavailability of large sized 3-D printers at DLR and for cost estimation of 3-D printing the CAD designed L-band antenna (as shown in Figure 6.1b) was sent to different 3-D printing companies. The outcome about the price estimation has far exceeded the available monetary resources. Due to the budget limitations, it was further decided to 3-D print the combination of VeGA and OMT at a print size which is affordable, can be measured and moreover which may have some direct use for an application. Considering these aspects, L-band (23.6 cm wavelength) was selected to 3-D print the antenna rather than in P-band (68.9 cm wavelength).

The concept of P-band antenna model is scaled down by a factor of 0.34 times to acheive in L-band. The L-band VeGA and OMT have dimensions of 76.8 cm × 74.8 cm × 74.8 cm. 3-D printed antenna model at L-band could be mostly used for Tandem-L calibration transponder. Tandem-L is a DLR proposal for a highly innovative satellite mission for the global observation of dynamic process on the Earth's surface with a goal to interferometrically image large portions of the global landmass once a week [56].

The design performance of L-band antenna (combination of VeGA and OMT) i.e., satisfying the design requirements mentioned in Tab. 1.1 is verified by performing simulations using numerical simulation tool. The design requirements are similar to P-band except the frequency (1.2575 GHz) and wavelength (23.6 cm) of Tandem-L mission has to be considered. Prior to FDM 3-D printing, necessary adjustments are made to L-band antenna model. The adjustments considered for P-band antenna structure are similarly implemented to L-band antenna model but with a different build (segment) size. The CAD files are then saved as industry standard STL file format where the 3d-printer can easily access these files for manufacturing the antenna model.

6.3 Light Weight L-band Antenna Fabrication

The L-band antenna (combination of Gaussian Corrugated Horn (VeGA)and Orthomode Transducer) was printed from Acrylonitrile Styrene Acrylate (ASA) plastic material using FDM based Fortus 400mc 3D-printer, with a build envelope of 406 mm × 355 mm × 406 mm, shown in Figure 6.2a. The L-band antenna was printed in a split-block fashion according to the build size of printer. The VeGA alone commissioned a set of 24 3-D printed segments, whereas the orthomode transducer requires a set of 8 segments. The individual printed segments are intended to be rejoined together using aceton bonding, bolts and metallic screws. The complete L-band antenna after rejoining the segments is shown in Figure 6.4a.

(a) (b) (c)

Figure 6.2: (a): The antenna segments printed using Fortus 400mc 3D-printer (b): 3-D printed segment (c): Applying the conductive paint, HSF44 to the printed plastic segments with a electric sprayer gun.

Meanwhile the OMT prototype used as a feeding part of VeGA employs four flat panel coaxial N-connectors , PCB probes and a tuning stub as shown in the Figure 6.3a. The flat paneled N-connectors are inserted through the desired holes and screwed to the outer surface of the OMT. The four metallic PCB probes as shown in the middle of the Figure 6.3a, which are used to couple the polarizations propagating within the waveguide or OMT are soldered to the inner metallic pins of the coaxial N-connectors. The PCB and tuning stub is introduced from the bottom of the OMT main body and a stablility of PCB within OMT is created by screwing the edges of PCB with the supporting parts printed within the waveguide. Details of the interior of the L-band antenna prototype can be seen in Figure 6.4b.

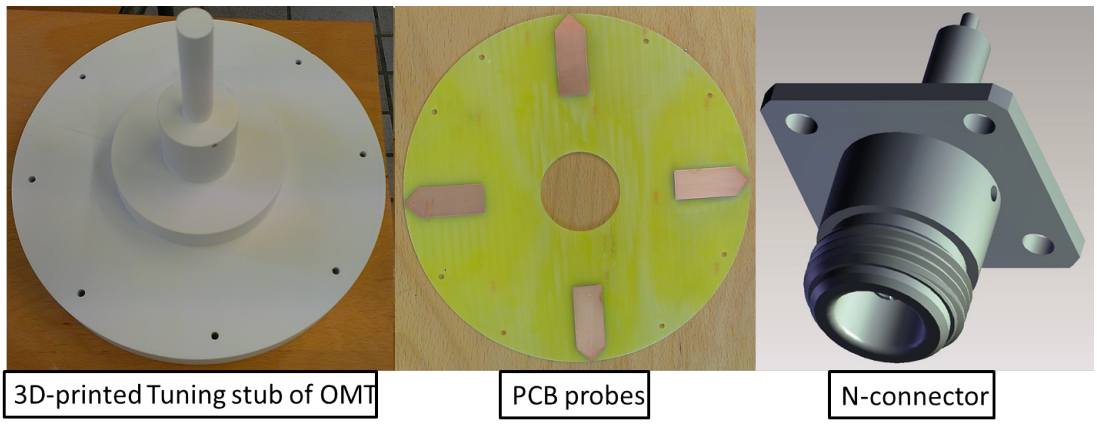

Figure 6.3: Physical realization of the individual components for the Orthomode Transducer prototype.

The antenna was printed in-house. The time spent for printing a single segment, shown in Figure 6.2b was approximately 9 hours. Moreover the individual corrugated segments

were coated with two layers of carbon conductive paint HSF44 as shown in Figure 6.2c. The recommended curing time of HSF44 coated single segment is nearly 7 days [46] as specified by the paint manufacturer. Once the segments are coated with carbon conductive paint, the segments are further coated with a protective white paint, where these segments were dried in a heating chamber. The important point to be noticed here is that neither the conductivity nor the thickness of the carbon conductive HSF44 paint is known. Once the painting of the segments are finished the segments are joined together to form an antenna and in between the segments a contact paste is applied - a copper paste ("CU") from the company "Äronix Spezialschmierstoffe", in order to avoid leakage of electromagnetic fields and also to maintain the conductivity between the segments. But before applying the copper paste between the segments, the white paint was removed from contact surfaces between the segments. The printed L-band antenna prototype is shown in Figure 6.4a. The final 3-D printed L-band antenna prototype had a mass of 27 kg, length of 76.8 cm and an aperture diameter of 74.8 cm, which could be easily transported by two persons.

(a) (b) (c)

Figure 6.4: (a): 3-D printed L-band antenna segments rejoined using acrylic and metal fasteners and further coated with a protective white paint (b): Inner view of the printed antenna prototype (c): 3-D printed L-band antenna prototype mounted with a mounting plate prior to compact test range measurements.

Chapter 7

Antenna Measurements and Performance Verification

The performance of any device can be only validated by conducting measurements. After 3-D printing the L-band antenna prototype, it is essential to validate the performance of the proposed design or prototype with proper measurements. The most important measurements in determining the characteristics of any antenna are the scattering-parameter, radiation pattern and gain measurements.

In this chapter, the first section addresses a relatively straightforward measurement, the scattering-parameter measurements, whereas the second section constitutes antenna radiation measurements performed in a compact test range measurement facility. Furthermore a comparison between the simulated and the measurement results of the 3-D printed L-band antenna prototype are presented followed by a discussion, which validates the design and manufacturing methodology.

7.1 Scattering Parameter Measurements

The scattering-parameter or S-parameter measurements is a fundamental measurement technique to any antenna. The Scattering parameters are executed with the support of a Vector Network Analyzer (VNA). The main parameters that a VNA measures are reflection and transmission characteristics of a network. In regard to measure the S-parameter of the L-band antenna prototype, a proper experimental test setup is needed.

The test setup constitutes a RohdeSchwarz ZVA-24 VNA with 4 independent channels and a RohdeSchwarz ZV-Z52 automatic calibration unit to calibrate the setup. Alongside the VNA and calibration unit, the test setup also includes two "1-18 GHz Model 4010180 Krytar double arrow 180° passive hybrid couplers" as part of the feeding system, two pairs

of equal length short coaxial cables and a pair of phase shifters to correct possible discrepancies in the cables length. The OMT has a disadvantage that the signals coupled to the probes in opposite sides have the same magnitude but a phase difference of 180° [2]. To provide these phase-shifted signals, 180° hybrid couplers are employed for recombining the signals from the OMT into a single channel. The S-parameter measurement setup employing all the desired components is shown in Figure 7.1.

To avoid unnecessary reflections the S-parameter measurements were carried out in an open area by pointing the horn antenna aperture towards the sky with no surrounding objects or buildings nearby. The measurement setup can be seen in the Figure 7.1. Further more the S-parameter measurements were also performed in a quiet zone of an anechoic chamber- the DLR's Compact Test Range (CTR) as depicted in Figure 7.2. Later on the return loss experimental measurement results from two zones (outdoor, quiet zone) were compared.

Before measuring the return loss with the VNA, the VNA has to be calibrated with a automatic calibration kit so that the effect of cables is compensated. After calibration, the VNA channel is connected to one of the input port of the 180° hybrid coupler and the coupler output ports are connected to a pair of tunable phase shifters followed by equal length cables. The cables are further connected to the orthogonal N-connector ports of the OMT. Before connecting the cables to the ports of OMT, the phase shifters are tuned untill a 180° phase difference is obtained at the output of the hybrid coupler. Due to the non-availability of two hybrid couplers during the S-parameter measurement, only a single 180° hybrid coupler is employed, so that a feasibility of taking return loss readings from a pair of orthogonal ports of OMT could be carried out at once whereas the other pair of non-employed orthogonal ports of OMT is terminated with matched loads. The setup is shown in Figure 7.1. The return loss measurements performed for the first pair of orthogonal ports is termed as Port-B1B3 and the measurement setup is repeated for the remaining pair of ports termed as Port-B2B4.

Figure 7.1: Return loss measurement: Experimental setup in open space.

Figure 7.2: Return loss measurement: Experimental setup in DLR's Compact Test Range (CTR).

The reflection coefficient (also return loss or S_{11}) measurement results obtained from the Port-B1B3 and Port-B2B4 for the L-band antenna prototype performed in free space and in CTR are shown in Figure 7.3. For the measurements performed in outdoor or free space, the S-parameters for both Port-B1B3 and Port-B2B4 are measured over a frequency sweep of 800 MHz bandwidth, whereas for the measurements in anechoic chamber, the S-parameters are measured over a frequency sweep of 500 MHz bandwidth at center frequency 1.2575 GHz which is depicted in Figure 7.3. The Figure shows that return loss characteristics measured both in open space and anechoic chamber have similar characteristics. Hence the reflection parameters S_{11} in dB for both environments are less than -16 dB

within the range between 1.2075 GHz to 1.2875 GHz (representing the relative bandwidth). The green bar represents the relevant bandwidth of 80 MHz in L-band. The measurement result for a frequency sweep from 0.85 to 1.65 GHz shows that the antenna has a center frequency at 1.2575 GHz as designed with a return loss of less than -25 dB at Port-B1B3 and a return loss less than -22 dB at Port-B2B4 for both environments (free space and anechoic chamber). The return loss within the operating bandwidth of 80 MHz is less than -16 dB, which is illustrated through a green bar in the Figure 7.3. Even though the return loss requirement of -20 dB in the operating band is violated, the obtained return loss measurement value of -16 dB is still acceptable for wide variety of applications.

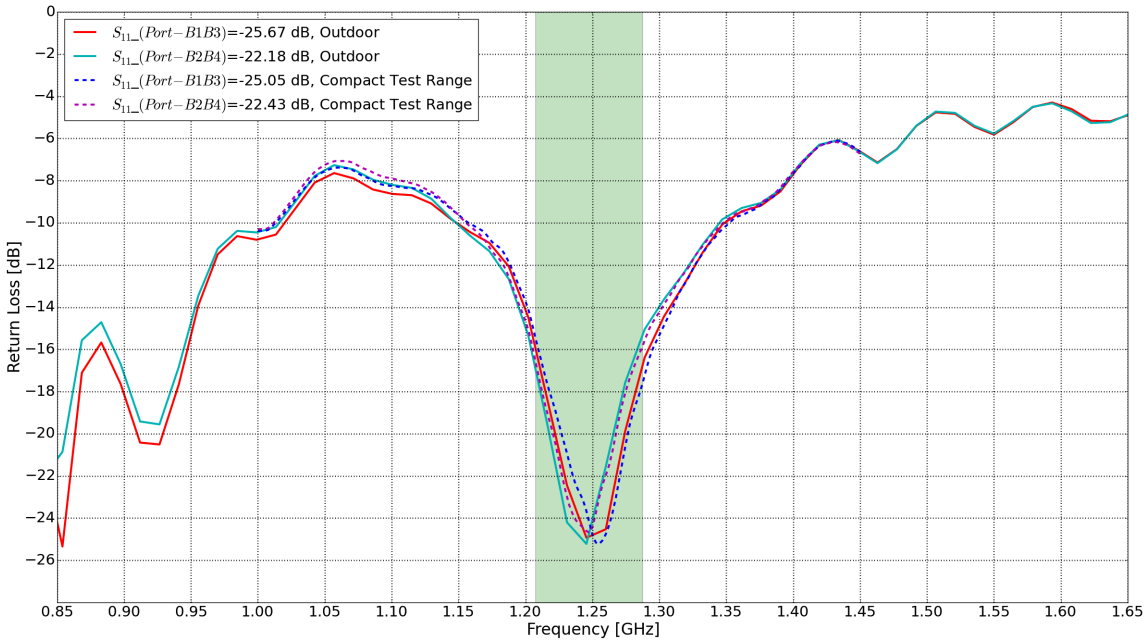

Figure 7.3: Measured return loss of the antenna prototype performed in free space and quiet zone (DLR's Compact Test Range) for the antenna prototype. The green bar represents the operating bandwidth of 80 MHz.

7.2 Compact Test Range Measurements

The radiation patterns and the gain of the L-band antenna prototype were measured by means of the DLR's compact Test Range (CTR), i.e. in an anechoic chamber. Inorder to measure these far field characteristics a sufficient separation greater than $\frac{2D^2}{\lambda}$, (where D is antenna largest dimension and λ is the free-space wavelength) between transmitting antenna and test antenna must be ensured, so that the spherical waves from the transmitting antenna is incident on the test antenna as plane waves. The far-field antenna radiation pattern is normally evaluated in outdoor far-field ranges or indoor range facility called as compact test ranges, where no reflections can occur.

The DLR's compact test range as shown in Figure 7.4 consist of a dual cylindrical parabolic reflector configuration, responsible for transforming a spherical wave generated from the transmitting antenna into a plane wave received by the test antenna (here combination of VeGA and OMT). The parabolic reflector configuartion is the core component of a compact test range and it provides far-field conditions for accurate real time measurements [57]. The surface accuracy of the reflectors allow the CTR to perform well from 1 GHz to 100 GHz and their geometry results in a quiet zone diameter of up to 3.8 meters [57]. The use of serrated edge reflectors on the borders of parabolic reflectors is to mitigate the edge diffraction effects on quiet zone performance. The unwanted reflections within the DLR's anechoic chamber are suppressed by the use of jagged triangle shaped absorbers. In CTR, the measurement device is mounted on a aluminum plate followed by a polarization turntable, so that the radiation pattern of the antenna prototype can be measured with the axis order elevation-over-azimuth-over-roll. The turntable is further handled by a movable positioner.

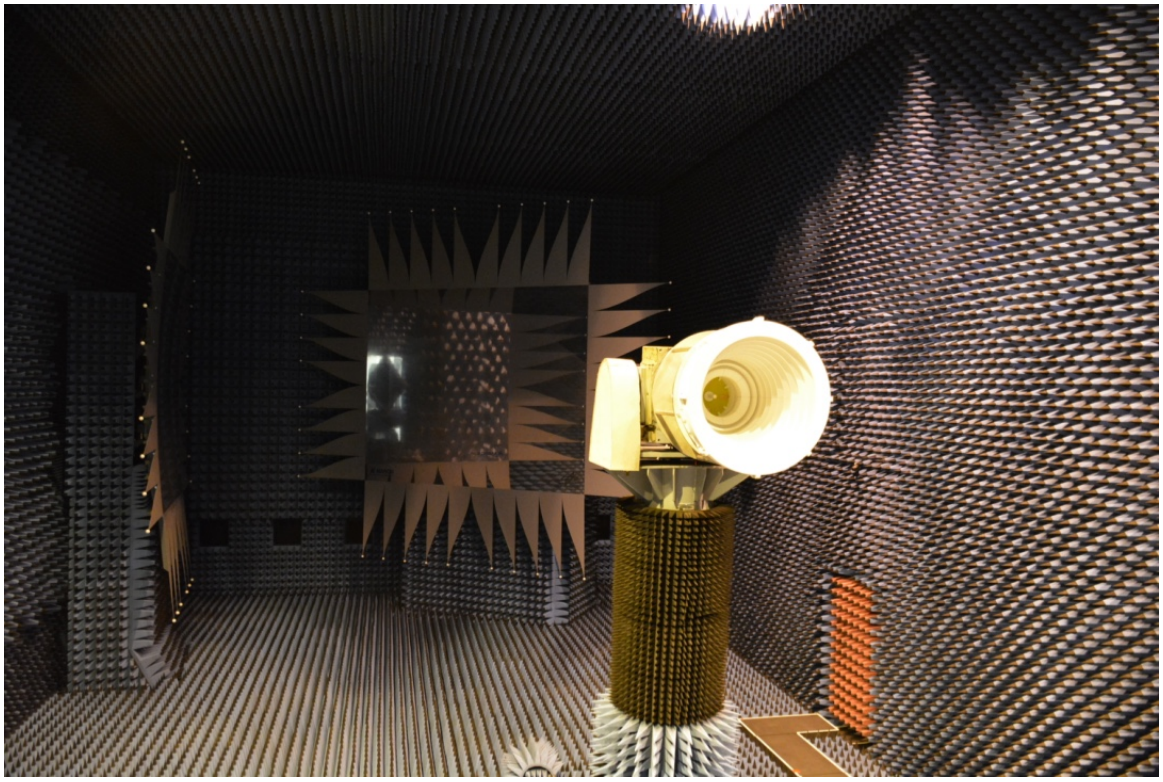

Figure 7.4: Compact test range facility at DLR-Microwaves and Radar Institute.

The resulting far-field measurements can then be compared to the design requirements or numerical simulations. A picture of DLR's compact test range is shown in Figure 7.4 with the developed antenna prototype placed on the positioner prior to the far-field measurements. In case of 3-D printed L-band antenna prototype a separate aluminum frame (around 3-4 Kg) is manufactured to mount and hold the antenna prototype by the

positioner. The antenna prototype mounted within an aluminum frame is shown on the right in Figure 7.2. The polarization turntable is computer controlled and a 4-port Rohde & Schwarz ZVA network analyser is used as RF-source and Local oscillator. The data collected from the network analyzer is post-proccessed using the analysis software tool ARCS V3.5. [57].

7.2.1 Antenna Gain and Polarization Measurements

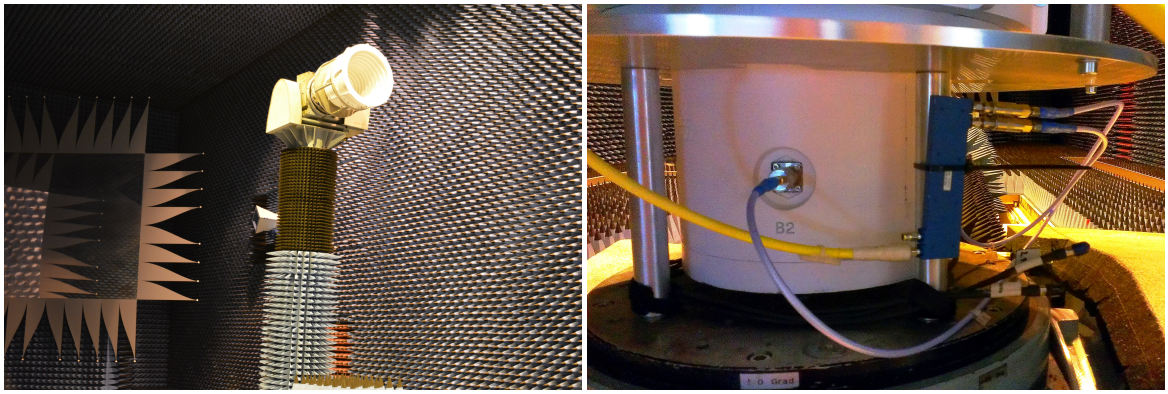

Figure 7.5: Antenna prototype mounted on the CTR positioner (left), The CTR network analyzer connected to the ports of OMT through hybrid couplers and phase shifters (right).

During the antenna measurements, two channels of the CTR network analyzer are connected to the inputs of a 180° hybrid and a 0.5-7 GHz Model 3005070 Krytar 90° hybrid coupler, so a feasibility of measuring the radiation pattern of the antenna prototype is achieved at single measurements. The 180° coupler used is similar to the one used during S-parameter measurements. By tuning pair of phase shifters and adjusting the length of cables, a 180° phase difference is achieved using a 90° coupler. This kind of assembly setup is shown on the right in Figure 7.5. In brief, one channel of network analyzer gives the signal received on a pair of orthogonal ports Port-B1B3 followed by a 180° hybrid coupler and another channel of the network analyzer gives the signal received on other pair of orthogonal ports Port-B2B4 followed by a tuned 180° hybrid coupler (90° hybrid coupler + tuned phase shifters). The antenna radiation pattern is measured over azimuth with a sweep of 360° the full spherical acquisition.

Figures 7.6, 7.7 presents the Cartesian plot for the far-field co-polar and cross-polar components regarding the measurements obtained from Port-B1B3 and Port-B2B4. Out of the measurements obtained for a full spherical acquisition, only the pattern cuts for H-plane (ϕ= 0°), worst-case cross-polar cut(ϕ= 45°) and E-plane (ϕ= 90°) are depicted. From the co-polar vs. Theta Cartesian plot as in Figure 7.6, the gain measured at Port-B1B3 and Port-B2B4 for E-plane and H-plane radiation pattern cuts is 10.6 dBi. Whereas when

considering the cross-polar Cartesian plot in Figure 7.7, the cross-polarization measured at worst case ϕ= 45° (as predicted from the simulations) at Port-B1B3 is measured as -31.3 dB and at Port-B2B4, it is measured as -33.59 dB. The mentioned worst case cross-polar values at Port-B1B3 and Port-B2B4 are observed at $\theta = 0°$. The decrease or variation of gain and cross-polar measurements when compared to simulations has a valid reason, which would be explained in the subsection 7.2.2 with appropriate plots.

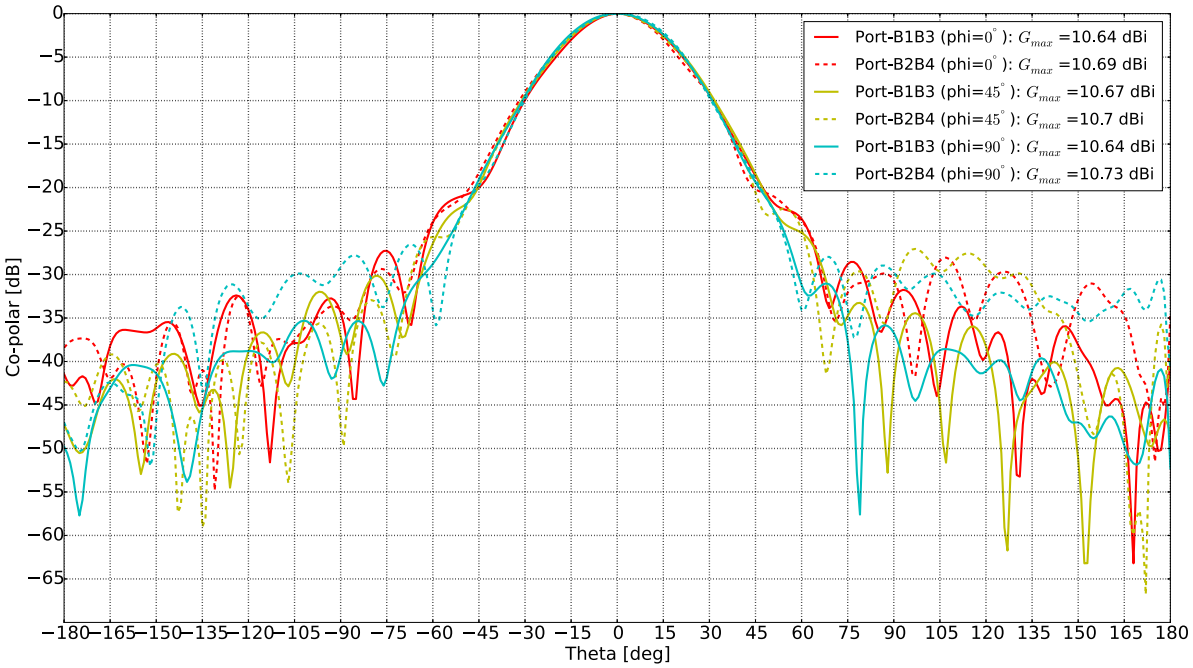

Figure 7.6: E-plane and H-plane cut far-field co-polar components of the L-band antenna prototype at center frequency 1.2575 GHz. The measured gain of around 10.6 dBi is obtained without considering the attenuation from the cables and also losses from the hybrid couplers. A clear explanation with appropriate plots about the contribution of losses resulting in variation of gain is given in subsection 7.2.2.

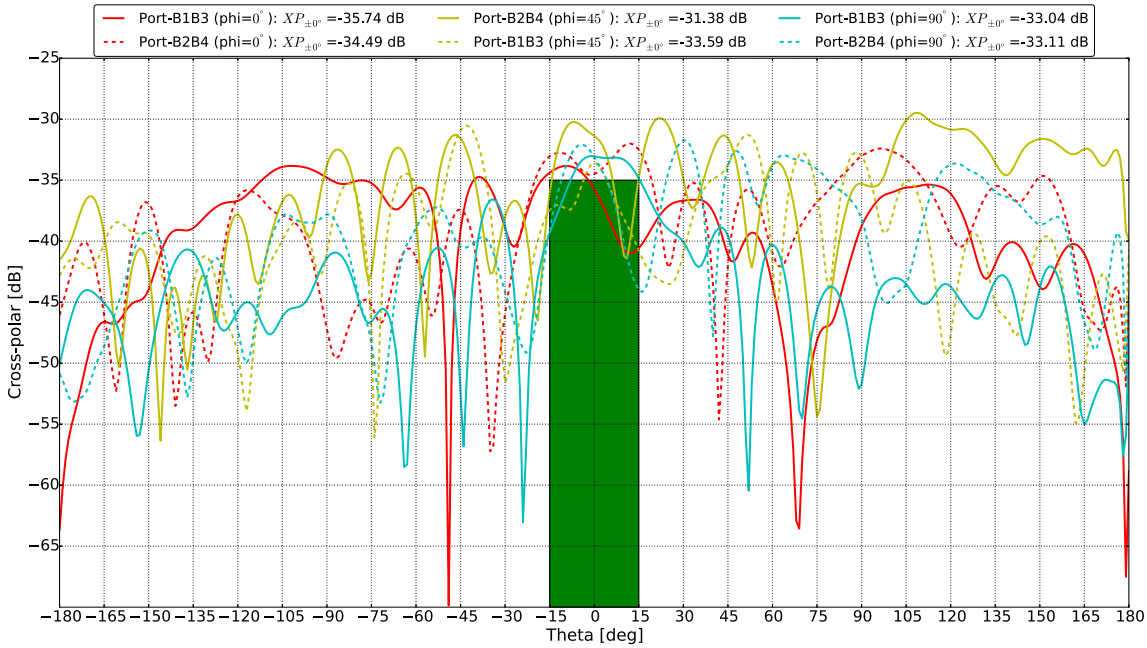

Figure 7.7: E-plane and H-plane cut far-field cross-polar components of the L-band antenna prototype at center frequency 1.2575 GHz.

A better description of the far-fields is given in Figure 7.8, where co-polar and cross-polar characterizations obtained from measurements and simulations are combined. This kind of combination or description gives a better idea whether the measurement and simulation results for E-plane and H-plane cuts are in good agreement. It can be observed from Figure 7.8 that the gain obtained from the CTR radiation pattern measurements at Port-B1B3 and Port-B2B4 is 10.64 dBi and 10.7 dBi respectively, which is 4.5 dBi less that what is achieved during simulations with 15.04 dBi. But the main beam is clearly formed and matches the simulated results quite well. The decrease or variation of gain in measurements when compared to simulations has a valid reason, which would be explained in the subsection 7.2.2 with appropriate plots. Meanwhile, when the worst case cross-polarization $\phi = 45°$ is observed towards viewing angle $\theta = 0°$, the measured cross-pol obtained at Port-B1B3 and Port-B2B4 is -31.38 dB and -33.59 dB. The results indicate that the requirement is only slightly violated and i.e. that further optimizations are likely to result in an improved and acceptable cross-polar isolation. Reasons for this violation could be: the water outlet holes made in the OMT, manufacturing tolerances and also due to the N-connectors of OMT, where a current distribution might leak into the prototype. The other possibility could be mostly due to the conductivity of the carbon paint which may be lower than expected.

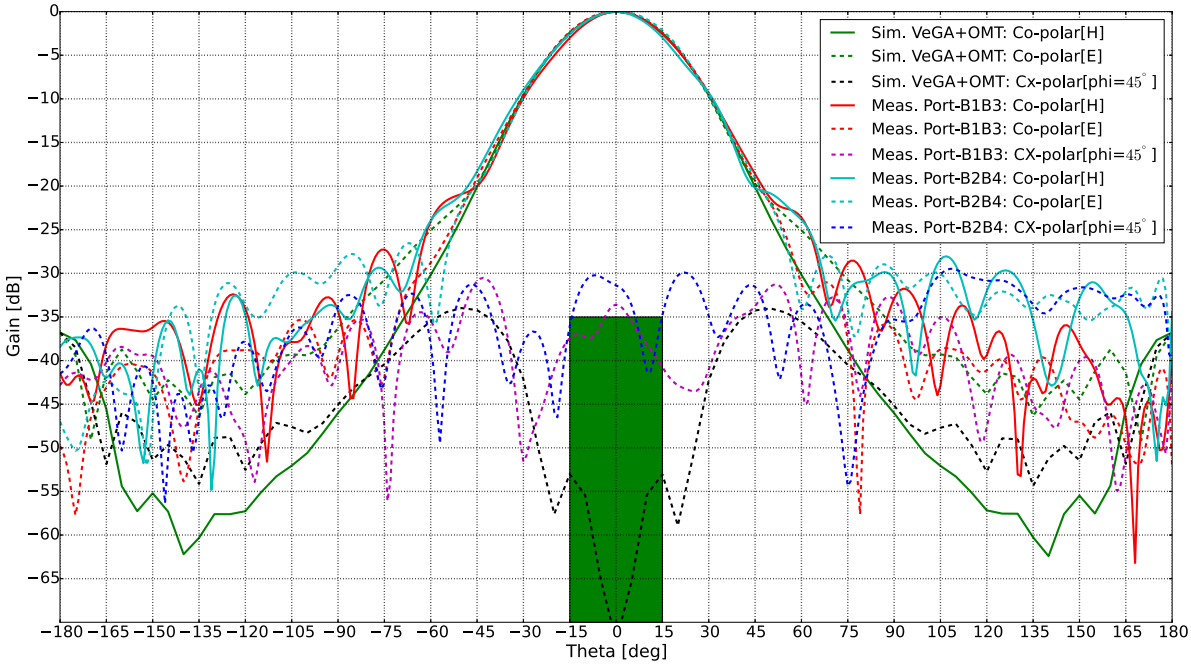

Figure 7.8: Comparison between measured and simulated far field radiation patterns of the L-band antenna prototype. The resulting measurements are plotted without considering attenuation losses from the cables and also the other factors contributing to losses like manufacturing tolerances.

A full spherical acquisition of far-field patterns is presented in Figure 7.9. Even from the spherical acquisition Figure, it is clear that measured antenna radiation pattern at Port-B2B4 has more sides lobes when compared to the radiation pattern at Port-B1B3. This kind of observation or analyzing of the data drew to a possibility that there may be a mismatch between N-connector coaxial pin and PCB probes.

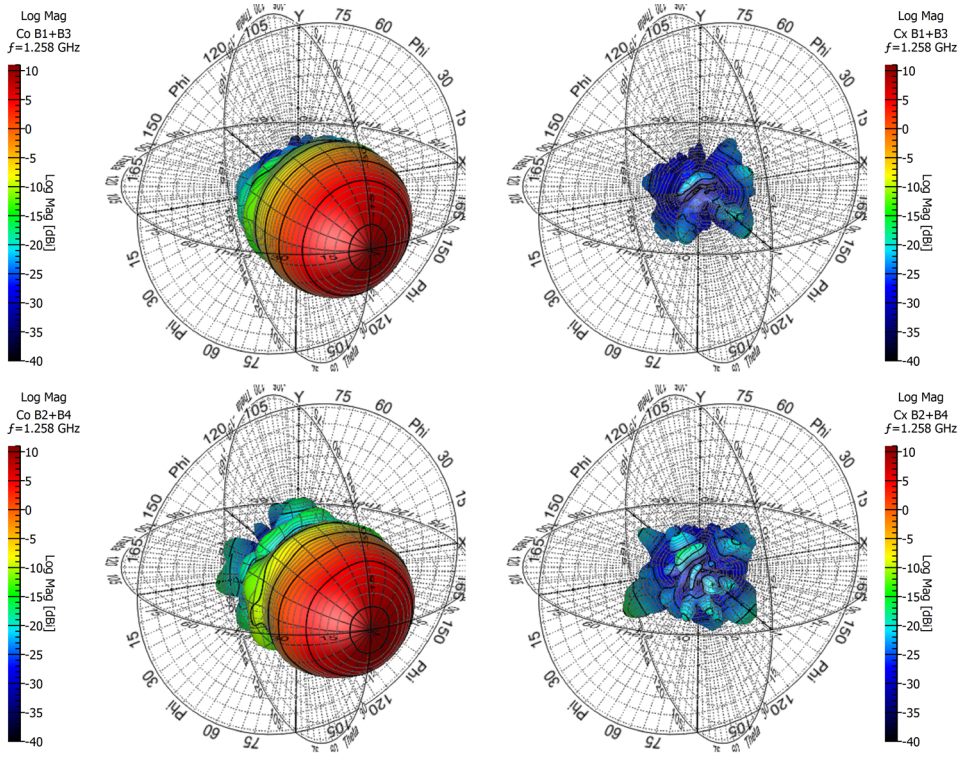

Figure 7.9: Measured spherical acquisition of the co-polar (left) and the cross-polar (right) radiation patterns for Port-B1B3 and Port-B2B4.

7.2.2 Analysis of factors contributing to losses from the antenna prototype

In regard to figure out the losses of about 4.5 dBi affecting the antenna gain, an in-depth analysis of data has been done. Initially the directivity of the antenna is obtained by integration of the measured far-field. Measured directivity and gain as a function of frequency at Port-B1B3 and Port-B2B4 are shown in Figures 7.10, 7.11 for a frequency of 1-1.8 GHz. The directivity achieved at center frequency 1.2575 GHz for Port-B1B3 is 15.17 dBi which is about 4.5 dBi higher than the measured gain, whereas the directivity obtained at Port-B2B4 is 15.14 dBi which is about 4.4 dBi higher than the measured gain at Port-B2B4. This shows that there is about 4.5 dBi losses contributing from different factors of the antenna. It was observed from further post-processing the data that the hybrid couplers and cables contribute losses of about 0.8 dBi and meanwhile the antenna alone contribute losses of around 4.5 dBi at two pair of orthogonal ports which may be the dielectric loss from the plastic material. A clear cut view of the factors contributing to the losses is shown in Figure 7.12. From the Figure 7.12, it can be observed that the antenna alone contribute a loss factor of about 3.57 dBi (violet curve) for Port-B1B3 and a loss factor of about 3.47 dBi from Port-B2B4 at 1.2575 GHz. The hybrid couplers contribute losses of about 0.87 db (pink-curve) for both ports at 1.2575 GHz, which is expected. To describe in short, the factors

contributing to losses in the antenna are expected to be from:

- The first reason would be the limited conductivity of the used carbon paint, which would result in some heating up and therefore some losses.
- The second reason is expected to be from the gaps between the segments like the water outlets where the conductivity might be lost between the segments and also may be due to the loose tolerances when assembling the antenna prototype.
- As the copper paste was applied to maintain conductivity in between the segments, a non-homogeneity was created between the conductivity of copper paste and carbon paint, which would be therefore one of the reason in contributing to losses. The other possibility might be due to the in-homogeneous conductivity created all over the antenna, as applied the carbon paint with a electric sprayer gun and also with a paint brush in between the corrugated ridges.

Hence after realizing the factors contributing to losses in the antenna measurements, it would be interesting to continue the measurements further by taking proper precautions like closing the water outlets with a conductive tape, once again spraying the antenna with one layer of carbon paint and also proper application of copper paste in between the segments, which might result in improved gain and cross-polar measurements.

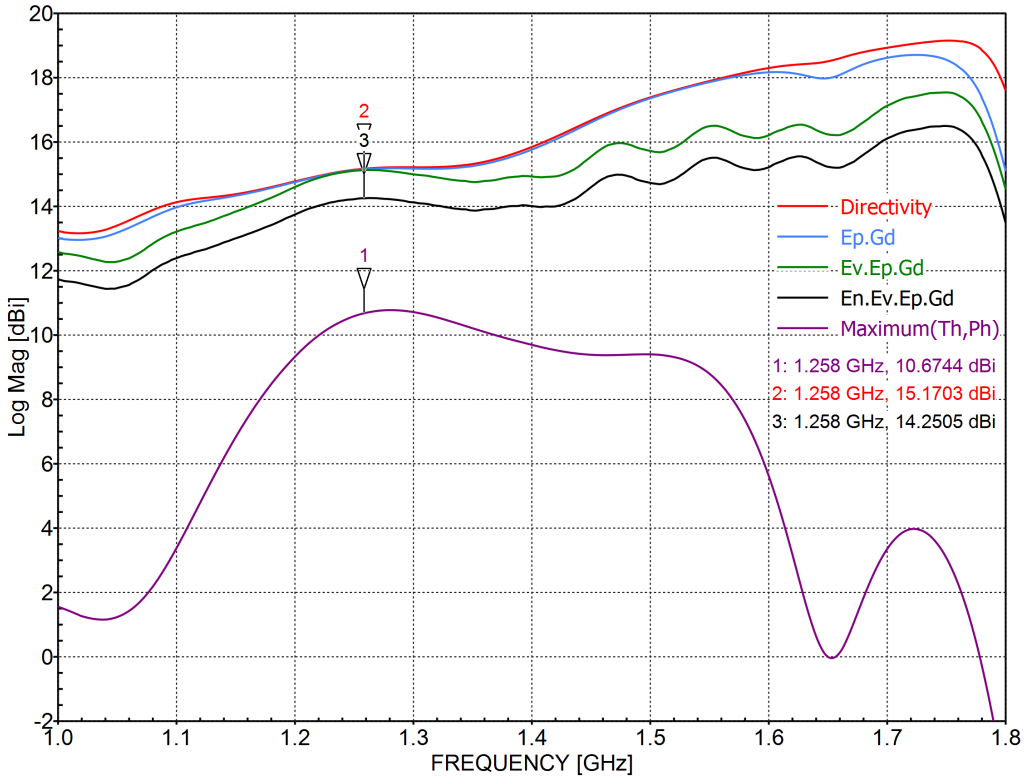

Figure 7.10: Measured Gain and directivity of L-band antenna prototype across frequency at Port-B1B3. The red curve represents the directivity and the violet curve represents the measured gain.

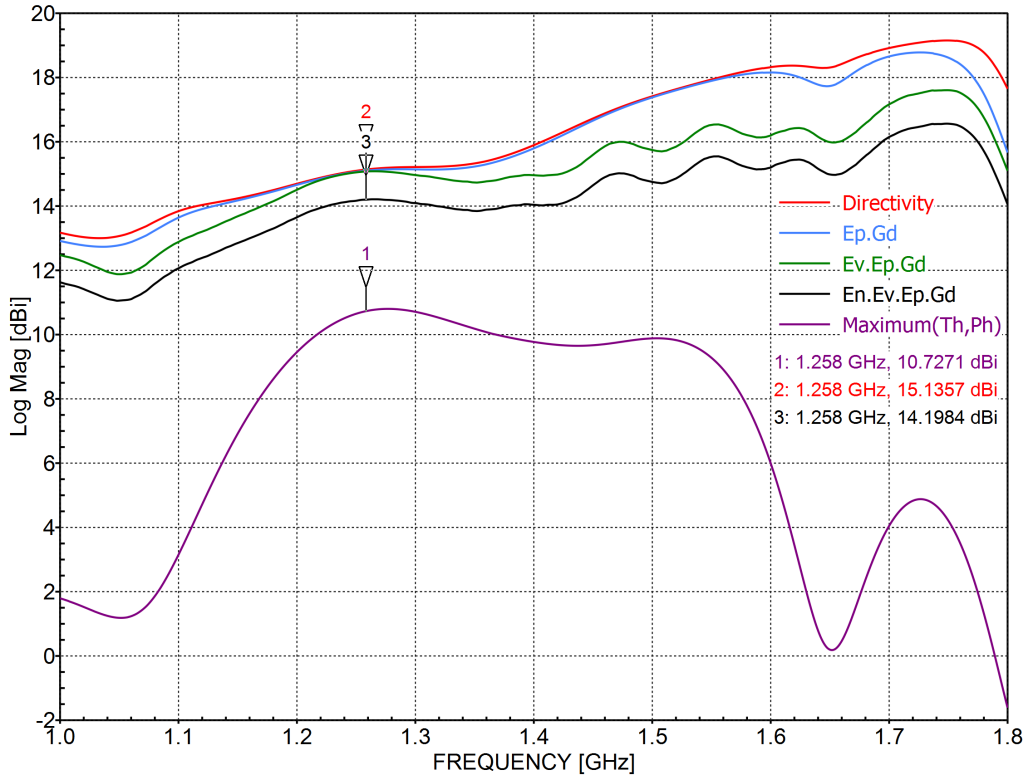

Figure 7.11: Gain and directivity of L-band antenna prototype at Port-B2B4 obtained from far-field measurements. The red curve represents the directivity and the violet curve represents the measured gain.

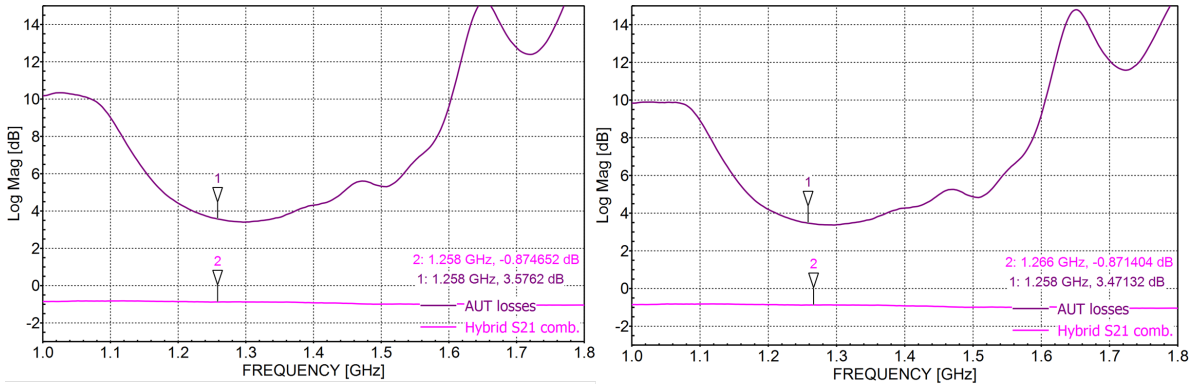

Figure 7.12: Measured losses from the Antenna under test (AUT) and from the 180° hybrid coupler for Port-B1B3 and Port-B2B4. At center frequency 1.2575 GHz, the losses from the measured antenna is itself 3.57 and 3.47 dB at two pair of orthogonal ports.

Chapter 8

Conclusions and Future Outlook

In the course of the thesis, a compact corrugated horn antenna, designated by the name VeGA and its feeding system called as orthomode transducer were developed at P-band (435 MHz) by considering standard waveguide dimensions. The design of the P-band VeGA and OMT were developed in a numerical simulation tool by performing necessary optimizations required to the model. Later on, the model performance was evaluated and validated through simulations by satisfying the design requirements listed in Tab. 1.1. The developed P-band antenna has dimensions of 2.2 m × 2.16 m × 2.16 m and shall be applied for compact calibration transponders developed by DLR. For this purpose the antennas should have low distortion of antenna radiation patterns, negligible cross-polarization and low side lobes.

As one of the requirement is to manufacture a lightweight horn antenna and its feeding system, the motive has drawn to 3-D print the designed P-band antenna using outdoor thermoplastic material and further coat with a conductive paint. In order to meet the design requirements like to use the antenna for outdoor applications and lightweight, several plastic materials and available conductive paints were reviewed and discussed. Then, an outdoor Acrylonitrile Styrene Acrylate (ASA) thermoplastic material and a cheap carbon conductive paint was introduced and justified as the appropriate materials to be used in manufacturing a lightweight antenna. Before 3-D printing the antenna, a new method was proposed by numerical simulations to examine the influence of plastic material and conductive paint on the radiation properties of antenna. As confirmed in series of simulations, the antenna modeled in perfect electric conductor and modeled in plastic and conductive paint are in good agreement satisfying the design requirements in Tab. 1.1. Before 3-D printing the antenna prototype a series of simulations were performed for the determination of allowable manufacturing tolerances and resultant uncertainties, which helps in maintaining a tight tolerance value during manufacturing and assembling the antenna prototype.

But due to time and cost constraints, it was finally decided to 3-D print the antenna in-house at L-band (1.2575 GHz) which is affordable, can be measured and moreover which has some direct use for an application for example L-band calibration transponders. The concept and procedure implemented at L-band is similar to that described in P-band, but for this purpose the P-band (68.9 cm) antenna design has to scaled down by a factor of 0.34 times to L-band (23.8 cm), which has dimensions of 76.8 cm × 74.8 cm × 74.8 cm.

The 3-D printed L-band antenna prototype performance was validated by performing scattering parameter measurements in an open area and in DLR's compact test range (CTR). Furthermore the far field measurements were executed and analysed likewise by means of DLR's CTR. The results of the L-band antenna prototype show a very good matching between the simulated and measured antenna radiation patterns. Except for the antenna gain with 10.64 dBi, losses of about 4.5 dBi have been observed. Valid reasons have been provided with appropriate plots for the factors contributing to losses in the antenna prototype.

Even the measured cross-polarization with -31.39 dB is only slightly high than the expected one with -35 dB. Hence by applying the different manufacturing steps, the performance of the L-band antenna might be improved. Therefore it is recommended to use professional techniques like electroplating and electroless plating to paint the antenna prototype, where a uniform thickness of conductive paint can be maintained all over the prototype. Despite of the valid losses from the antenna prototype, the cheap outdoor plastic, conductive paint and 3-D printing technique involved in manufacturing L-band choked GPHA and its feeding system OMT prototype has sufficiently good radiation properties, which is highly recommendable to be used in L-band calibration transponders.

Future Outlook In addition to the conclusions, I would also like to propose further research based on the contribution done in this work to develop handheld and userfriendly conductivity and thickness measurement tools for determination of conductivity and thickness of conductive coatings.

Bibliography

[1] Heinrich Axt. Vergleichende analyse groß- und kleinschreibung beachten von antennenkonzepten und antennenentwicklung für P-band kalibriertransponder, 2014. v, 4, 12, 21, 22, 26, 27, 35, 36, 37, 38, 51

[2] Carlos Henrique Severino. Compact feeding system for a P-band circular horn antenna, 2015. v, 12, 35, 36, 37, 38, 40, 41, 42, 43, 51, 74

[3] Biomass-Mission-Advisory-Group. *Report For Mission Selection: BIOMASS*. ESA Communication Production Office, 2012. v, 11

[4] Alaska Satellite Facility. Sar basics. `https://www.asf.alaska.edu/about-sar/sar-basics/`, Jan. 2016. 4, 8

[5] *Volume and Surface Resistivity Measurements of Insulating Materials Using the Model 6517A Electrometer/High Resistance Meter*. Keithley Instruments, Inc., 2001. 4, 15, 16

[6] A.P. Sajeev and S. Karunakaran. *Shielding effectiveness evaluation of metalised plastics with signal source inside test console*. Electromagnetic Interference and Compatibility '99. Proceedings of the International Conference on, 1999. 4, 17

[7] J.-C.S. Chieh, B. Dick, S. Loui, and J.D. Rockway. Development of a ku-band corrugated conical horn using 3-d print technology. 2014. 4, 24, 25, 33

[8] Ian G. Cumming and Frank H.Wong. *Digital Processing Of Synthetic Aperture Data: Algorithms and Implementation*. Artech House Publishers, 2005. 7, 8

[9] J.C. Curlander and R. N. McDonough. *Synthetic Aperture Radar: Systems and Signal Processing*. New York: John Wiley Sons, Inc, 1991. 7, 8, 9, 10

[10] Y. K. Chan and V. C. Koo. *An introduction to synthetic aperture radar (SAR)*. Progress In Electromagnetics Research B, Vol. 2, 27-60, 2008, 2008. 7

[11] Robert O. Harger. *Synthetic Aperture Radar Systems: Theory and Design*. ACADEMIC PRESS, Inc, 1970. 8

[12] Helena Norrman. *Development of a Microstrip Antenna for a Miniaturized Transponder*. Master Thesis - Lulea University of Technology (LTU), 2006. 8

[13] M. Schwerdt, B. Bräutigam, M. Bachmann, Björn J. Döring, D. Schrank, and J. Hueso Gonzalez. *Final TerraSAR-X calibration results based on novel efficient calibration methods*. IEEE Trans. Geosci. Remote Sens., vol. 48, no. 2, pp. 677-689, Feb 2010. 9

[14] Björn J. Döring, Kersten Schmidt, Matthias Jirousek, Daniel Rudolf, Jens Reimann, Sebastian Raab, John Walter, and Marco Schwerdt. *Hierarchical Bayesian Data Analysis in Radiometric SAR System Calibration: A Case Study on Transponder Calibration with RADARSAT-2 Data*. 2013. 9

[15] Anthony Freeman. *SAR calibration: An overview*. IEEE Transactions on Geoscience and Remote Sensing 30.6 (Nov. 1992), pp. 11071121, 1992. 9, 10

[16] M. Schwerdt, D. Hounam, J. L. Alvarez-Pérez, and T. Molkenthin. *The calibration concept of TerraSAR-X, a multiple mode high resolution SAR*. Can. J. Remote Sens., vol. 31, no. 1, pp. 30–36, Feb. 2005. 9

[17] D. Rudolf, S Raab, B.J. Döring, M. Jirousek, J. Reimann, and M. Schwerdt. *Absolute Radiometric Calibration of the Novel DLR Kalibri Transponder*. German Microwave Conference (GeMiC), 2015 German, 2015. 9

[18] Matthias Jirousek, Björn J. Döring, Philipp Looser, and Marco Schwerdt. *Linearity Measurements of an Accurate Transponder for Calibrating Future Spaceborne SAR Systems*. Synthetic Aperture Radar, 2012. EUSAR. 9th European Conference on, 2012. 9

[19] K. Sarabandi and Tsen-Chieh Cgiu. *Optimum corner reflectors design*. Radar Conference, 1996., Proceedings of the 1996 IEEE National, 1996. 10

[20] Björn J. Döring, Jens Reimann, Matthias Jirousek, Daniel Rudolf, Sebastian Raab, and Marco Schwerdt. *The Three-Transponder Method: A Novel Method for Accurate Transponder RCS Calibration*. Progress In Electromagnetics Research B, Vol. 61, pp. 297–315, 2014. 10, 11

[21] D. Geudtner. *Overview of the GMES Sentinel-1 mission*. in Proc. 9th Eur. Conf. Synth. Aperture Radar, Nuremberg, Germany, 2012, pp. 159–161. 10

[22] M. Jirousek, B. Döring, D. Rudolf, S. Raab, and M. Schwerdt. Development of the highly accurate dlr kalibri transponder. In *EUSAR 2014; 10th European Conference on Synthetic Aperture Radar; Proceedings of*, pages 1–4, June 2014. 11

[23] Anthony Freeman. *SAR Calibration: An Overview*. IEEE Transcations on Geoscience and Remote Sensing, Nov 1992. 11

[24] M. Schwerdt and J. Reimann. *Biomass System Calibration and Validation Plan*. Project Report, Bio-SYS-DLR-PL-0108, Issue 1.0, 18th June 2015. 11

[25] M. Kutz. *Handbook of Materials Selection*. Wiley, 2002. 13, 15

[26] S.K. Das and A. Das. *Antennas and Wave Propagation*. Tata McGraw Hill Education, 2013. 14, 18

[27] Tibtech innovations. `http://www.http://www.tibtech.com/conductivity.php`. 2011. 14

[28] T.S. Bird and C. Granet. Fabrication and space-qualifying a lightweight corrugated horn with low side lobes for global-earth coverage. 2008. 14, 23, 24

[29] H.W. Ott. *Electromagnetics compatibility Engineering*. Wiley, 2011. 15

[30] Vishu Shah. *Handbook of Plastics Testing and Failure Analysis*. John Wiley Sons, Inc., New jersey, 2007. 15

[31] D. Weston. *Electromagnetics Compatibility: Principles and Applications, Second edition, Revised and Expanded*. Taylor & Francis, 2001. 17, 18

[32] F. M. Smits. Measurement of sheet resistivities with the four-point probe. *The Bell System Technical Journal*, 37(3):711–718, May 1958. 18, 58

[33] M. Abbas-Azimi, F. Mazlumi, and F. Behnia. *Design of Broadband Constant-Beamwidth Conical Corrugated-Horn Antennas [Antenna Designer's Notebook]*. Antennas and Propagation Maganzine, IEEE, 2009. 18, 19

[34] Jorge Teniente Vallinas. *Modern Corrugated Horn Antennas*. Universidad Pública de Navarra, 2003. 18, 19, 20, 21

[35] Klaus Kark. *Antennen und Strahlungsfelder - Elektromagnetische Wellen auf Leitungen, im Freiraum und ihre Abstrahlung, 2. Auflage*. Vieweg & Sohn Verlag, 2006. 19

[36] Christophe Granet, Graeme James, and Trevor Bird. *Optimization of corrugated horn radiation patterns via a spline-profile*. ANTEM 2002, 9th International Symposium on Antenna Technology and Applied Electromagnetics, 2002. 21

[37] Christophe Granet, Graeme James, and Trevor Bird. *Compact Low-Sidelobe Corrugated Horn For Global Earth Coverage*. IEEE, 1999. 21

[38] Carlos del Río Bocio. *High performance horn antenna design (II)*. Universidad Pública de Navarra, 2006. 21

[39] J. Teniente, A. Martinez, B. Larumbe, A. Ibañez, and R. Gonzalo. *Design Guidelines of Horn Antennas That Combine Horizontal and Vertical Corrugations for Satellite Communications*. 2015. 21

[40] C. Granet, T.S. Bird, and Graeme L. James. Compact multimode horn with low sidelobes for global earth coverage. 2000. 23, 24

[41] J.A. Andriambeloson and P.G. Wiid. A 3d-printed pla plastic conical antenna with conductive-paint coating for rfi measurements on meerkat site. 2015. 25, 26, 33, 55

[42] C.C. Ibeh. *Thermoplastic materials: Properties, Manufacturing, Methods, and Applications*. CRC Press, 2011. 27, 28

[43] "BASF Corporation". *"Extrusion grades, performance comparisons and applications"*, 2001. 28, 29

[44] Overview over 3D printing technologies. `http://www.addittively.com/en/learn-about/3d-printing-technologies`. 30, 31, 33

[45] MG Chemicals. Super Shield conductive nickel coating 841 technical data sheet. `http://www.mgchemicals.com`, 2013/03. 33, 34, 53, 62

[46] YSHIELD. Yshield EMR-Protection HSF44. `http://www.yshield.com`, 2015/05. 34, 55, 58, 62, 72

[47] EM Software & Systems - S.A. (Pty) LTD. FEKO - Suite 7.0. software, 2014. 35, 36, 41, 48, 52, 61

[48] Spinner GmbH. Cross Reference For Hollow Metallic Waveguides, 2014/08. "Issue K". 37

[49] Blender Online Community. Blender Foundations 2.77a. software, 2002. 45

[50] TQC GmbH. Developers and manufacturers of paint test equipment. `http://www.tqc.eu`, 2016. 56, 57

[51] American Society for Testing and Materials Information Handling Services. Standard Test Methods for Measuring Adhesion by Tape Test1, 2000. 56

[52] Napson Corporation. Handheld sheet resistance measurement instrument. `http://en.napson.co.jp`, 2015/10. 58, 59

[53] Suragus GmbH. Portable Contact Sheet Resistance Tester. `http://www.suragus.com`, 2015/10. 60

[54] A. Gonzalez and Y. Uzawa. Tolerance analysis of alma band 10 corrugated horns and optics. *IEEE Transactions on Antennas and Propagation*, 60(7):3137–3145, July 2012. 63

[55] J. Teniente, A. Martínez, B. Larumbe, A. Ibáñez, and R. Gonzalo. Design guidelines of horn antennas that combine horizontal and vertical corrugations for satellite communications. *IEEE Transactions on Antennas and Propagation*, 63(4):1314–1323, April 2015. 63

[56] Alberto Moreira, Gerhard Krieger, Irena Hajnsek*, Konstantinos Papathanassiou, Marwan Younis, Paco Lopez-Dekker, Sigurd Huber, Michelangelo Villano, and Matteo Pardini. Tandem-l: A highly innovative bistatic sar mission for global observation of dynamic processes on the earth's surface. *German Aerospace Center*, April 2014. 70

[57] M. Limbach, B. Gabler, A. Di Maria, R. Horn, and A. Reigber. *DLR Compact Test Range facility*. 2012 6th European Conference on Antennas and Propagation (EUCAP), March 2012. 77, 78